Studies of Shock Wave Focusing Using Geometrical Shock Dynamics

Thesis by

Joseph E. Cates

In Partial Fulfillment of the Requirements
for the Degree of
Doctor of Philosophy

California Institute of Technology
Pasadena, California

1996
(Submitted May 1, 1996)

Acknowledgements

I am grateful to the faculty, staff, and students of GALCIT for their friendship during my studies at Caltech. Without their assistance, in far too many ways to list, this thesis would have been impossible. In particular, I wish to thank my advisor Professor Sturtevant for his guidance and support during my work. Throughout, he has allowed me the greatest freedom to explore many fascinating problems, even when in areas not directly related to my research.

During my undergraduate studies at the University of Alabama, Dr. Freeman, Dr. Visscher, and Dr. Whitaker, provided many opportunities and encouragement to embark on my graduate studies.

The support of my family has been unfailing – Mom and Dad, Jim, Charlotte, and Claire deserve a long-overdue "Thank you." In closing, I owe Lourdes my dearest thanks for her loving support and infinite patience during the final months.

Abstract

A finite-difference numerical method for geometrical shock dynamics has been developed, based on the analogy between the equations and the supersonic potential equation. The method has proven to be a valuable tool for analyzing the complex nonlinear processes that occur in shock focusing. The approximate shock dynamics theory is able to capture the effects of initial Mach number and aperture angle on the focal region. The numerical results duplicate the strong, moderate, and weak shock behaviors observed in experiments, with good agreement for focal pressure and triple-point path. The primary error arises due to the inability of shock dynamics to allow regular reflection along the centerline. Adequate resolution of the focal region proves to be particularly important to properly judge the accuracy of the shock dynamics solution. The appropriate shock dynamics equations are developed for the case of shock propagation into a nonuniform media for a general equation of state with nonuniform freestream velocity. The modification of the numerical method to this more general problem is straightforward. The complete shock dynamics equations are derived for both perfect gas and water using the modified Tait equation. The results for propagation of a planar shock over cylindrical gas inhomogeneities shows excellent agreement with experimental results.

The propagation of sonic booms through the atmosphere provides examples of all major types of weak shock behavior. The extensive seismic network in Southern California, consisting of over two hundred sites covering over 50,000 square kilometers, is used to map primary and secondary sonic boom carpets. The results show sonic boom ground exposure under the real atmosphere is much larger than previously expected.

Contents

List of Figures

List of Tables

List of Symbols

a = quantity related to characteristic angle (Eqn. 2.14)

a_0 = freestream sound speed

a_{01}, a_{02} = sound speed inside and outside inhomogeneity, respectively

a_1 = factor in differencing of $\sigma U/J$ term (Eqn. 2.25)

a_{11}, a_{12}, a_{22} = grid parameters (Eqn. 2.18)

A, $A(M)$ = Area-Mach relation

A' = derivative of Area-Mach relation with respect to Mach number

A_r = ray tube area

b_1 = term in differencing of $\sigma U/J$ term (Eqn. 2.25)

B = coefficient in modified Tait equation

c = freestream sound speed (geometrical acoustics)

c_0 = initial sound speed (geometrical acoustics)

c_{eff} = effective sound speed (geometrical acoustics), $c_{eff} = c_0 + \mathbf{v} \cdot \mathbf{n}$

$c(M)$ = wave speed of disturbances (Eqn. 2.9)

f = coefficient of dU_s factor (Eqn. 4.10)

= coefficient of $\mathrm{d}U_s/U_s$ contribution to $\mathrm{d}A/A$

F = body force

g = coefficient of $\mathrm{d}a_0/a_0$ contribution to $\mathrm{d}A/A$

h = coefficient of $\mathrm{d}p_0/p_0$ contribution to $\mathrm{d}A/A$

= enthalpy

Δh_s = enthalpy change due to $T\mathrm{d}s$ integral

$\mathbf{i}$ = unit vector along normal

k = coefficient of $\mathrm{d}\gamma/\gamma$ contribution to $\mathrm{d}A/A$

= offset according to crossflow direction

J = grid Jacobian (Eqn. 2.19)

m = characteristic angle (Eqn. 2.9)

M = shock Mach number

M_0 = initial or reference Mach number

= component of freestream velocity along ξ (Eqn. 4.31)

M_c = centerline Mach number at arrival of lead disturbance from corner

M_w = shock Mach number relative to freestream velocity

M_∞ = reference Mach number (potential equation)

$\mathbf{n}$ = unit vector normal to shock

n = exponent of strong shock approximation (Eqn. 2.6)

N_0 = component of freestream velocity along η (Eqn. 4.31)

p = pressure

R = radius of inhomogeneity

= ratio of density, $R = \rho_2/\rho_1$

s = distance along channel

= entropy

$\mathbf{s}$ = wave-slowness vector (geometrical acoustics)

S = dA factor for changes in freestream (Eqn. 4.10)

t = time

T = temperature

u = velocity

u, v, w = components of gradient of α, α_x, α_y, α_z

$=$ components of gradient of ϕ, ϕ_x, ϕ_y, ϕ_z (potential equation)

$\mathbf{u} =$ freestream velocity

$u_0 =$ x-component of freestream velocity

$u_{0n} =$ component of freestream velocity normal to shock

$u_z =$ vertical surface displacement

$U =$ contravariant velocity component

$=$ zonal (E/W) wind speed component (geometrical acoustics)

$=$ sonic boom speed

$U_S =$ normal velocity of shock relative to freestream velocity

$v =$ specific volume, $v = 1/\rho$

$\mathbf{v} =$ freestream velocity vector (geometrical acoustics)

$V =$ contravariant velocity component

$=$ meridional (N/S) wind speed component (geometrical acoustics)

$V_S =$ total normal velocity of shock

$x' =$ x-coordinate of system in which shock is at rest

$x_c =$ coordinate of centerline arrival of lead disturbance from corner

$z^* =$ turning point altitude (geometrical acoustics)

$Z =$ ratio of shifted pressures, $Z = (p_2 + B)/(p_1 + B)$

$\alpha =$ shock position at time t

$\gamma =$ ratio of specific heats

$\Gamma =$ coefficient in modified Tait equation for water

$\theta =$ ray angle

$=$ parameter controlling order of differencing scheme

$\theta_0 =$ aperture angle

$=$ initial ray angle (geometrical acoustics)

$\theta_c =$ centerline ray angle at arrival of lead disturbance from corner

$\lambda(M) =$ Area-Mach relation term (Eqn. 2.3)

$\lambda,\ \mu =$ elastic constants of half-space

$\mu =$ Area-Mach relation term (Eqn. 2.4)

$=$ Mach angle (potential equation)

$=$ artificial viscosity factor

$\nu =$ artificial viscosity coefficient

$\xi,\ \eta =$ transformed coordinates

$\rho =$ density

$\rho_0 =$ density at zero pressure in Tait equation

$\sigma(M) =$ Mach number divided by Area-Mach relation: $\sigma = M/A(M)$

$\tilde{\sigma}(M) =$ σ biased in the upwind direction (Eqn. 2.31)

$\tau =$ N-wave duration

$\phi =$ velocity potential (potential equation)

$\omega =$ integral in Riemann invariant (Eqn. 2.9)

$=$ frequency

$\Omega =$ geometrical acoustics term, $\Omega = 1 - \mathbf{v} \cdot \mathbf{s}$

Chapter 1 Introduction

The focusing of shock waves produces localized high pressures in the focal region, and the shock emerges from the focus with the front geometry fundamentally changed. Understanding the mechanisms of focusing is critical because converging fronts occur frequently, indeed whenever the front becomes concave forward such as by passing through nonuniform media or reflection from curved surfaces. The high pressures localized near the focus may be beneficial, as in lithotripsy, or detrimental, as in superbooms from aircraft sonic booms. The change in shock geometry downstream of the focus has significant implications for shock stability, sonic boom propagation, and sonoluminescence.

One application of shock wave focusing is extracorporeal shock wave lithotripsy (ESWL). In this treatment for urinary tract stones, weak converging shock waves are generated externally and shaped to focus within the patient's body at the stone. Outside the focal region, the weak shocks pass through the surrounding tissue without causing damage. In the focal region, the shock pressure increases dramatically to over 50 MPa leading to fragmentation of the stone, although the exact fracture mechanisms are not completely understood. Over the course of several thousand shocks, the stone is shattered into pieces small enough to be passed by the patient. To better understand the source of tissue damage and the primary means of stone fragmentation in the ESWL procedure, exact knowledge of the flowfield in the focal region is required.

A linear description of shock focusing is given by geometrical acoustics. The shock is advanced along rays at the local sound speed relative to the surrounding medium, the front speed being independent of the shock strength. The strength of the shock is inversely related to the ray tube area. Whenever the shock front is concave forward the rays will cross. At the crossing point, the ray tube area goes to zero and the amplitude becomes infinite in acoustic theory. Downstream of the ray crossing, the shock front emerges folded.

In real fluids, nonlinear effects dominate the flow in the focal region and prevent infinite amplitude at the focus. The experiments of Sturtevant and Kulkarny (1976) first demonstrated the complex types of behavior seen at the focus. Weak, moderate, and strong types of behavior are observed according to the initial strength of the shock. The front emerges from the focus crossed and folded for weak shocks, corresponding to regular reflection at the centerline, and with a triple point and Mach stem for strong shocks, corresponding to Mach reflection at the centerline.

A successful model must accurately include nonlinear effects. Ideally, one would like to numerically solve the Euler equations for the shock focusing problem, but this remains a difficult, computationally expensive task. The problem involves a combination of very weak shocks outside the focus and much stronger shocks in the focal region with disparate length scales which combine to require high resolution in the focal region. Although Euler solutions of limited problems have been presented and the problem would seem to lie within the capability of modern numerical schemes with advanced mesh refinement algorithms, to the author's knowledge no detailed study with rigorous comparison to experimental results has been completed.

The theory of geometrical shock dynamics (Whitham 1957, 1959) offers an appealing alternative to a full Euler solution. As in the linear theory of geometrical acoustics, the shock is treated as a front propagating along rays, but in nonlinear shock dynamics the shock speed along the ray is a function of the shock strength. By neglecting the flow behind the shock in favor of concentrating on the motion of the shock itself, the problem is greatly simplified and the dimensions of the problem compared to a full Euler solution are reduced by one. This approximation seems appropriate for problems where the shock is accelerating, and disturbances behind the shock are less likely to strongly effect the shock propagation. The accuracy of the approximation for specific problems is difficult to assess in advance, but the theory has historically been viewed as less accurate for weak shocks. Nonetheless, in practice geometrical shock dynamics has proven to be a valuable theory for a surprisingly large set of problems. Various efforts to extend shock dynamics have been proposed (Best 1991, Prasad 1994), but none have gained wide acceptance.

Analytical solutions of the shock dynamics equations are available for simple geometries, but numerical methods are needed for most problems of interest. Since the equations are hyperbolic, characteristic methods have been used for problems such as shock propagation over cylinders and spheres (Bryson & Gross 1961). Front-tracking numerical methods, where discrete points along the shock front are advanced along rays, have been extensively developed (Henshaw *et al.*, 1986). As noted by Whitham (1959) the equations of geometrical shock dynamics are analogous to the supersonic potential equation, and numerical schemes for the supersonic potential equation can be adapted to shock dynamics (Schwendeman 1993). The use of finite-difference schemes offers advantages over previous characteristic and front methods. Finite-difference schemes provide conservative formulations where the effects of artificial viscosity can be clearly characterized. The method is easily extended to three dimensional problems with optimal grids for specific problems. In addition, finite-difference schemes are typically easier to set up and apply to specific problems than previous methods, especially for problems with weak shocks.

The related problem of shock propagation through a general, non-uniform medium is essential to understanding the mechanics of shock focusing. The problem is especially applicable to sonic boom propagation through the atmosphere and ESWL treatment involving propagation through inhomogeneous tissue. The theory of shock dynamics has been extended to non-uniform perfect gases by Catherasoo & Sturtevant (1983), who used a characteristic method to study planar shock propagation over a gaseous interface. The front-tracking numerical method has been adapted to shock dynamics in non-uniform gases (Schwendeman 1988). Apazidis and Lesser (1996) extended the method to non-uniform freestream flow ahead of the advancing shock, although an additional term required in the Area-Mach relation was omitted.

1.1 Outline

In Chapter 2, a conservative, finite-difference scheme for geometrical shock dynamics is developed for an arbitrary grid, based on the analogy with the supersonic potential

equation. The resulting numerical method is used to explore the problem of focusing of weak shocks in Chapter 3 with the goal of assessing the accuracy of shock dynamics for this type of problem. The results duplicate the behavior of strong, moderate, and weak shock waves observed experimentally. In comparison with the experiments of Sturtevant and Kulkarny (1976), shock dynamics is seen to accurately predict the focus location, but overpredicts the pressure. For weak shocks, the main inaccuracy can be attributed to the failure of shock dynamics to allow regular reflection at the centerline.

In Chapter 4, the theory of geometrical shock dynamics and the numerical method are extended to the more general case of shock propagation into a nonuniform medium with non-zero freestream velocity. The equations are derived for a general equation of state, with the equations expanded for the special case of a perfect gas. Results for propagation of a planar shock over cylindrical gas inhomogeneities show excellent agreement with experimental results of Haas (1984, 1987).

In Appendix A, the Area-Mach relation for water using the modified Tait equation is derived. An analytic equation of state for water is also used to calculate the shock jump conditions to assess the accuracy of the Tait equation, and to examine the temperature and entropy changes across the shock.

The propagation of sonic booms through the atmosphere provides examples of all major types of shock behavior: focusing, refraction, diffraction, and reflection. In Appendix B, seismic stations, which routinely detect the small ground motions produced by sonic booms, are used to analyze sonic booms from a SR-71 pass at $M = 3.15$ at high altitude, the landing of space shuttle Discovery at Edwards AFB, the passage of shuttle Discovery over Washington and Oregon at approximately $M = 14$, and a set of "mystery booms" in California. In particular, the extensive seismic network in Southern California, consisting of over two hundred sites covering over 50,000 square kilometers, provide a unique opportunity to map the carpets from direct and indirect sonic booms. The ground patterns under a real atmosphere are observed to be extremely complex. Ray theory fails to predict indirect sonic boom arrival times, observed multiple booms within the first shadow region, and extensive overlap of

the multiply refracted sonic booms. The extensive ground coverage of the "mystery boom" and shuttle reentry booms suggest boom exposure under the real atmosphere is much larger than previously expected.

Bibliography

Apazidis, N. and Lesser, M.B. (1996) "On generation and convergence of polygonal-shaped shock waves," *J. Fluid Mech.*, **309**, 301–319.

Best, J. (1991) "A generalisation of the theory of geometrical shock dynamics," *Shock Waves*, **1**, 251–273.

Bryson, A.E. and Gross, R.W.F. (1961) "Diffraction of strong shocks by cones, cylinders, and spheres," *J. Fluid Mech.*, **10**, 1–16.

Catherasoo, C.J. and Sturtevant, B. (1983) "Shock dynamics in non-uniform media," *J. Fluid Mech.*, **127**, 539–561.

Haas, J.-F. (1984) *Interaction of Weak Shock Waves and Discrete Gas Inhomogeneities*, Ph.D. Thesis, Graduate Aeronautical Laboratories, California Institute of Technology, Pasadena, CA.

Haas, J.-F. and Sturtevant, B. (1987) "Interaction of weak shock waves with cylindrical and spherical gas inhomogeneities," *J. Fluid Mech.*, **181**, 41–76.

Henshaw, W.D., Smyth, N.F., and Schwendeman, D.W. (1986) "Numerical shock dynamics using geometrical shock dynamics," *J. Fluid Mech.*, **171**, 519–545.

Prasad, P. (1994) "A Nonlinear Ray Theory," *Wave Motion*, **20**, 21–31.

Schwendeman, D.W. (1988) "Numerical shock propagation in non-uniform media," *J. Fluid Mech.*, **188**, 383–410.

Sturtevant, B. and Kulkarny, V.A. (1976) "The focusing of weak shock waves," *J. Fluid Mech.*, **73**, 651–671.

Whitham, G.B. (1957) "A new approach to problems of shock dynamics, Part I: Two-dimensional problems," *J. Fluid Mech.*, **2**, 145–171.

Whitham, G.B. (1959) "A new approach to problems of shock dynamics, Part II: Three-dimensional problems," *J. Fluid Mech.*, **5**, 369–386.

Chapter 2 Numerical Method

In this chapter, a finite-difference numerical method is developed for the equations of geometrical shock dynamics for a perfect gas. In the first section, the equations of shock dynamics are introduced; a complete derivation is delayed until Chapter 4 for a more general case. The analogy between the equations of geometrical shock dynamics and the full potential equations, outlined in Section 2.2, provides a basis for development of the finite-difference method in Section 2.3.

2.1 Geometrical Shock Dynamics

Geometrical shock dynamics is an important approximate theory for problems involving shock propagation. For problems such as the focusing of weak shocks, where a wide range of shock strengths are encountered and high resolution is required in the focal region, numerical solutions of the Euler equations are still difficult and computationally expensive. By neglecting the interaction of the shock with the flow behind the shock, shock dynamics reduces by one the number of dimensions of the problem, greatly simplifying the computation.

In geometrical shock dynamics, the shock is considered as a wavefront propagating down ray tubes normal to the front, as with geometrical acoustics. However, shock dynamics is nonlinear, in that the velocity of the shock depends on the strength of the shock. To close the system, an equation is introduced to relate the shock strength, represented by the Mach number, to the variation of the ray tube area. To accomplish this, the motion of the shock down the ray tube is treated as propagation down a tube with solid walls and a slowly varying cross-sectional area. By ignoring the effect of disturbances overtaking the shock from behind, a relationship can be derived for the Mach number as a function of area. This Area-Mach relation is then applied to express the Mach number as a function of ray tube area along the shock front.

Since the theory emphasizes the effect of the geometry on the shock propagation by ignoring the interaction of the shock with the flow behind the shock, one would expect the theory to be particularly appropriate for problems with accelerating shocks and problems dominated by geometry. However, geometrical shock dynamics has proved to be accurate for a much wider range of problems. In simple problems where comparison is available with full compressible flow solutions, shock dynamics has shown better agreement for strong shocks, and is generally considered less reliable for weak shocks.

The equations of geometrical shock dynamics (Whitham 1957, 1959) are

$$\nabla \cdot \left(\frac{M}{A(M)} \nabla \alpha \right) = 0, \qquad M = \frac{1}{|\nabla \alpha|}. \tag{2.1}$$

$\alpha(\mathbf{x}) = a_0 t$ gives the shock position at time t, a_0 being the undisturbed sound speed. $A(M)$ is the Area-Mach number relation, which specifies the relation between the area A of the ray tube and the shock strength M. For a perfect gas, the Area-Mach number relation is given by

$$A(M) = \exp\left[- \int_{M_0}^{M} \frac{M \lambda(M)}{M^2 - 1} \mathrm{d}M \right], \tag{2.2}$$

where

$$\lambda(M) = \left(1 + \frac{2}{\gamma + 1} \frac{1 - \mu^2}{\mu} \right) \left(1 + 2\mu + \frac{1}{M^2} \right), \tag{2.3}$$

$$\mu^2 = \frac{(\gamma - 1)M^2 + 2}{2\gamma M^2 - (\gamma - 1)}. \tag{2.4}$$

An analytical expression for the Area-Mach integral was originally given by Bryson and Gross (1961); in which several misprints were later pointed out by Henderson (1980). A slightly more compact expression was derived by Catherasoo (1982).

Two approximations are commonly used for the Area-Mach relation, the weak shock approximation ($M \to 1$):

$$A(M) = (M - 1)^{-2}, \tag{2.5}$$

and the strong shock approximation ($M \to \infty$):

$$A(M) = M^{-n}, \qquad n = 1 + \frac{2}{\gamma} + \sqrt{\frac{2\gamma}{\gamma - 1}}. \tag{2.6}$$

Area-Mach relations for other equations of state have been used in shock dynamics. The Area-Mach relation for water using the modified Tait equation is developed in Appendix A.

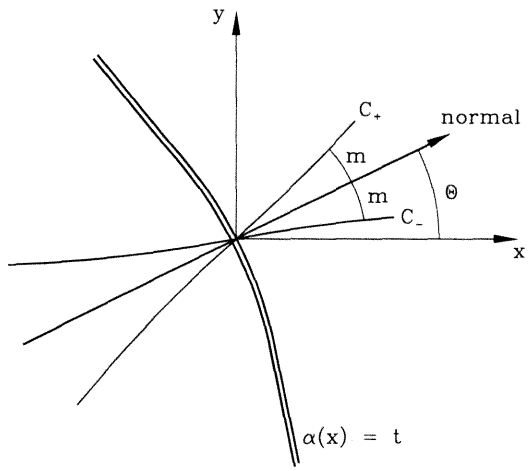

Figure 2.1: Shock front geometry and characteristic angles.

The equations of geometrical shock dynamics form a hyperbolic, second-order partial differential equation that describes the wave motion of disturbances propagating along the shock front. Discontinuities, called *shock-shocks*, can form along the shock carrying a change in shock angle and an increase in Mach number. *Shock-expansions* can also form, for example in shock diffraction around a sharp corner.

For two-dimensional problems, the equations can be conveniently written in characteristic form (Whitham 1957, 1959). As shown in Fig. 2.1, the characteristics lie at the characteristic angle m above and below the ray angle θ:

$$C_{\pm} : \frac{\mathrm{d}y}{\mathrm{d}x} = \tan(\theta \pm m). \tag{2.7}$$

Along the characteristics, the compatibility relation is given by:

$$\theta \pm \omega(M) = \text{constant}. \tag{2.8}$$

The additional variables introduced are defined as:

$$\omega(M) = \int_1^M \left[\frac{\lambda(M)}{M^2-1}\right]^{1/2} \mathrm{d}M, \qquad c(M) = \sqrt{-\frac{M}{AA'}}, \qquad \tan m = \frac{Ac}{M}. \tag{2.9}$$

The derivative A', which represents differentiation of the Area-Mach relation with respect to the Mach number, is always negative. The Area-Mach relation $A(M)$ and the functions $\omega(M)$, $c(M)$, and $m(M)$ are plotted in Fig. 2.2 for a perfect gas with $\gamma = 1.4$. For weak shocks, in the limit $M \to 1$, the characteristic angle approaches zero, and the characteristics collapse into the rays.

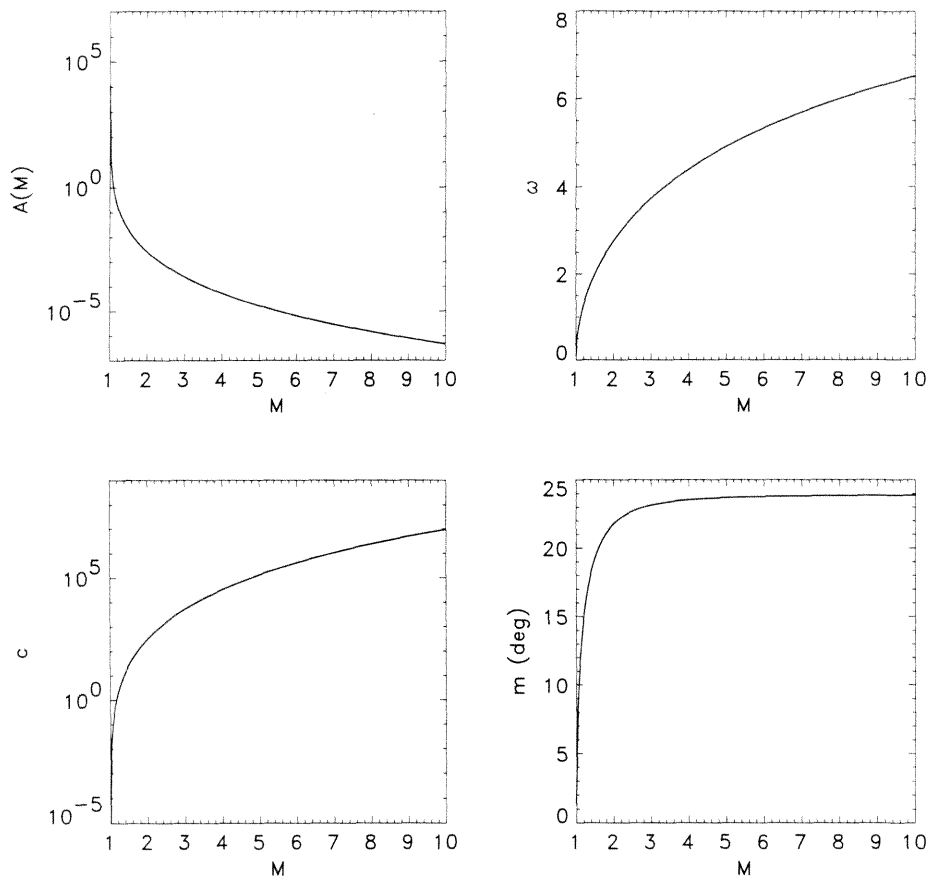

Figure 2.2: Area-Mach relation $A(M)$ and functions $\omega(M)$, $c(M)$, and $m(M)$ for perfect gas, $\gamma = 1.4$.

2.2 Analogy with Potential Flow

The conservative form of Eqn. 2.1 in Cartesian coordinates can be written as

$$\frac{\partial(\sigma u)}{\partial x} + \frac{\partial(\sigma v)}{\partial y} + \frac{\partial(\sigma w)}{\partial z} = 0, \tag{2.10}$$

where $u = \alpha_x$, $v = \alpha_y$, $w = \alpha_z$ are the components of the gradient of α, and

$$M = \left[u^2 + v^2 + w^2\right]^{-1/2}, \qquad \sigma \equiv \frac{M}{A(M)}. \tag{2.11}$$

As originally noted by Whitham (1959), the equations of geometrical shock dynamics are analogous to the full potential equation for steady supersonic flow.[1] The shock front position α is analogous to the velocity potential and the ratio of the Mach number to area σ is analogous to the density. To complete the comparison with the supersonic potential equation, the variable a, analogous to the sound speed, is defined as

$$a^2 \equiv \left[M^2\left(1 - \frac{MA'}{A}\right)\right]^{-1}, \tag{2.14}$$

where the prime represents differentiation with respect to the Mach number. With the above definition, a is directly related to the characteristic angle:

$$a = \frac{\sin m}{M}, \tag{2.15}$$

and appears frequently in the numerical method.

[1] In Cartesian coordinates, the potential equation in terms of the velocity potential ϕ is:

$$\frac{\partial(\rho\phi_x)}{\partial x} + \frac{\partial(\rho\phi_y)}{\partial y} + \frac{\partial(\rho\phi_z)}{\partial z} = 0, \tag{2.12}$$

where $u = \phi_x$, $v = \phi_y$, $w = \phi_z$ are the velocity components, density and speed of sound are:

$$\rho = \left[1 - \left(\frac{\gamma - 1}{2}\right) M_\infty \left(u^2 + v^2 + w^2 - 1\right)\right]^{1/\gamma - 1}, \qquad a = \sqrt{\frac{\rho^{\gamma-1}}{M_\infty^2}}. \tag{2.13}$$

The characteristics are Mach lines which lie at the Mach angle $\mu = \sin^{-1}(1/M)$ above and below the streamline.

2.3 Finite-Difference Formulation

Only a small relatively simple set of problems of interest can be worked analytically using the method of shock dynamics. Two numerical approaches have been used for a wide range of problems: the method of characteristics (Bryson & Gross 1961, Catherasoo & Sturtevant 1983) and front-tracking methods (Henshaw *et al.*, 1986). Characteristics methods are typically more cumbersome than finite-difference methods and difficult to extend to three dimensional problems, and thus their numerical applications have been fairly limited. In the front-tracking methods, points along the shock front are advanced along rays normal to the front according to the shock Mach number. The ray-tube area is then used to compute the Mach number along the front at the new position. The extension of front-tracking methods to three-dimensions is straightforward. However, the method requires the frequent splining of the points with addition of points in areas where the front contracts, and the removal of points where the front expands. The precise effect of adding and deleting points, and what artificial viscosity is introduced by this smoothing, is difficult to quantify.

With the analogy between the shock dynamics equation and the potential equation, Whitham (1959) noted that numerical methods for the potential equation could be directly applied. Extensive numerical work on finite-difference methods for the potential equation was done in the 1970's and 1980's before computation of the full Euler equations was feasible. Only recently have these finite-difference schemes been applied to the equations of shock dynamics (Schwendeman 1993). Schwendeman presented a finite-difference method for three-dimensional problems using the strong-shock approximation for the Area-Mach relation, and considered the problems of shock propagation in channels.

For problems involving weak shocks, where very strong shock-shock discontinuities can occur, sophisticated numerical methods are required. In the front-tracking methods, points along the shock front at the shock-shock can cross several other points in one time step. To continue the solution requires either sophisticated methods to remove intermixed points or else extremely small time steps. Using the existing,

simpler finite-difference methods, solution steps can fail due to iterations which produce Mach numbers less than one during convergence. In this section, an improved finite-difference scheme is developed based on the methods developed for the supersonic potential equation (Shankar 1982, Shankar *et al.*, 1983, 1985) which is suitable for weak shock problems with strong discontinuities.

Introducing an arbitrary coordinate system (not necessarily orthogonal) defined by $\xi = \xi(x, y)$, $\eta = \eta(x, y)$, Eqn. 2.10 can be written in strong-conservation form:

$$\frac{\partial}{\partial \xi}\left(\frac{\sigma U}{J}\right) + \frac{\partial}{\partial \eta}\left(\frac{\sigma V}{J}\right) = 0, \tag{2.16}$$

where U, V are the contra-variant velocity components given by

$$U = a_{11}\alpha_\xi + a_{12}\alpha_\eta, \qquad V = a_{12}\alpha_\xi + a_{22}\alpha_\eta, \tag{2.17}$$

and the grid parameters are

$$a_{11} = \xi_x^2 + \xi_y{}^2, \qquad a_{12} = \xi_x\eta_x + \xi_y\eta_y, \qquad a_{22} = \eta_x^2 + \eta_y^2, \tag{2.18}$$

$$J = \xi_x\eta_y - \xi_y\eta_x. \tag{2.19}$$

The Mach number is now given by

$$M = [U\alpha_\xi + V\alpha_\eta]^{-1/2}. \tag{2.20}$$

In the solution procedure, we consider ξ to be the marching, time-like direction and assume all information is known at the ith and all previous levels. The problem is to advance the solution to the level $i + 1$ and obtain new α values.

At all levels, the quantities α_ξ, α_η are computed from

$$(\alpha_\xi)_{i,j} = \frac{\alpha_{i,j} - \alpha_{i-1,j}}{\Delta\xi} \qquad (\alpha_\eta)_{i,j} = \frac{\alpha_{i,j+1} - \alpha_{i,j-1}}{2\Delta\eta}, \tag{2.21}$$

where a backward difference is used for the marching direction ξ and a central

difference is used for the crossflow direction η. For half-points, the velocities are averaged between neighboring points which gives:

$$(\alpha_\xi)_{i,j+1/2} = \frac{(\alpha_{i,j+1} - \alpha_{i-1,j+1}) + (\alpha_{i,j} - \alpha_{i-1,j})}{2\Delta\xi} \tag{2.22}$$

$$(\alpha_\eta)_{i,j+1/2} = \frac{\alpha_{i,j+1} - \alpha_{i,j}}{\Delta\eta}. \tag{2.23}$$

Once these quantities are known, U and V follow directly from Eqn. 2.17 and M from Eqn. 2.20.

2.3.1 σU/J Term

Since the ξ direction is the marching direction, the ξ derivative term in Eqn. 2.16 is backward differenced as

$$\frac{\partial}{\partial\xi}\left(\frac{\sigma U}{J}\right)_{i+1,j} \approx \frac{(a_1 - \theta b_1)\left\{(\sigma U/J)_{i+1,j} - (\sigma U/J)_{i,j}\right\} - \theta b_1\left\{(\sigma U/J)_{i,j} - (\sigma U/J)_{i-1,j}\right\}}{a_1\Delta\xi_1 - \theta b_1(\Delta\xi_1 + \Delta\xi_2)}, \tag{2.24}$$

where

$$a_1 = (\Delta\xi_1 + \Delta\xi_2)^2\ , \qquad b_1 = (\Delta\xi_1)^2, \tag{2.25}$$

and

$$\Delta\xi_1 = \xi_{i+1} - \xi_i\ , \qquad \Delta\xi_2 = \xi_i - \xi_{i-1}\ . \tag{2.26}$$

The parameter θ controls the order: $\theta = 0$ gives first-order accuracy and $\theta = 1$ gives second-order accuracy (Shankar & Osher, 1983).

The upwind differencing of the ξ derivative term produces a truncation error whose leading term is

$$\frac{\sigma}{Ja^2}\left(1 - \frac{a^2 a_{11}}{U^2}\right)U^2\alpha_{\xi\xi\xi}\Delta\xi. \tag{2.27}$$

This term always represents a positive artificial viscosity when

$$\frac{U^2}{a_{11}} > a^2. \tag{2.28}$$

As an illustration, consider the case of Cartesian coordinates where the stability requirement for the marching direction reduces to $u^2 > a^2$. Since $M = 1/\sqrt{(u^2+v^2)}$ and θ is the ray angle, $u = \cos\theta/M$. Substituting from the definition of m and simplifying, the requirement reduces to

$$\cos^2\theta > \sin^2 m, \tag{2.29}$$

Since m is the characteristic angle (see Fig. 2.1), the condition is equivalent to the requirement that characteristic information propagates forward in x.

In general, the stability requirement of Eqn. 2.28 is satisfied if the information propagates along characteristics only from behind the current point. To march along the ξ direction, the domain of dependence for point i, j must not include information from forward of the current ξ row. For problems where the shock is strongly curved, the numerically grid must be chosen to maintain ξ as the propagation direction. For weak shocks, the characteristic angle approaches zero and stability requires only that the component of the shock velocity along the marching direction be positive. The stability condition is more restrictive for higher Mach numbers as the characteristic angle increases, and the ξ direction must be more closely aligned with the shock normal. Ideally, the grid is aligned such that locally at each point the ξ direction is normal to the shock.

2.3.2 σV/J Term

The η derivative term in Eqn. 2.16 is central-differenced and written at level $i+1$ to make the resulting scheme fully implicit:

$$\frac{\partial}{\partial\eta}\left(\frac{\sigma V}{J}\right)_{i+1,j} \approx \frac{1}{\Delta\eta}\left\{\left(\frac{\sigma V}{J}\right)_{i+1,j+1/2} - \left(\frac{\sigma V}{J}\right)_{i+1,j-1/2}\right\}. \tag{2.30}$$

The suitability of the above difference depends on the nature of the flow in the crossflow plane. When $1 - a_{22}a^2/V^2 < 0$ the crossflow is elliptic-type as shown in Fig. 2.3(a). The characteristics propagate information from both the positive and

negative η directions, and the central differencing is appropriate. For hyperbolic-type crossflow as shown in Fig. 2.3(b), $1 - a_{22}a^2/V^2 < 0$. In this case, the characteristics propagate information a single η direction, and the central differencing of Eqn. 2.30 is unstable. In this case, artificial viscosity is necessary to preserve stability.

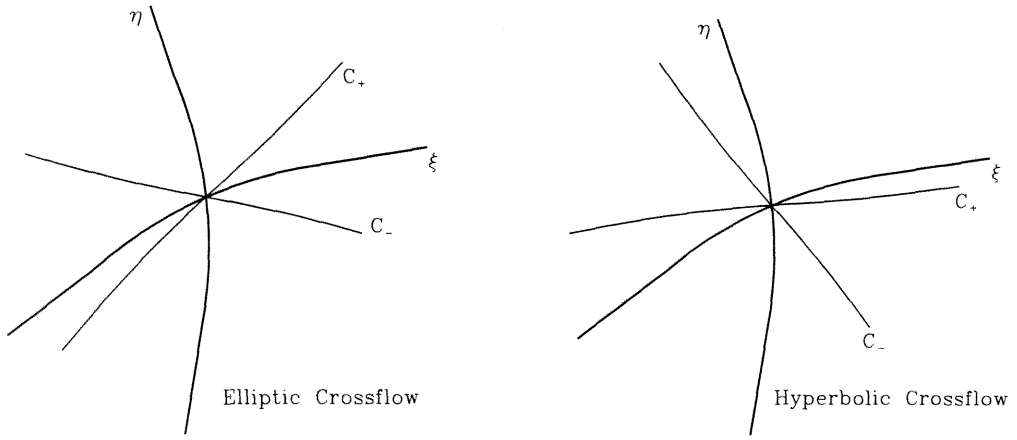

Figure 2.3: Crossflow type according to characteristic angles.

To implement the required artificial viscosity, the value of σ is biased in the direction of the crossflow V.[2] The σ in Eqn. 2.30 is replaced by $\tilde{\sigma}$ defined to be

$$\tilde{\sigma}_{i+1,j+1/2} = (1-\nu)\sigma_{i+1,j+1/2} + \frac{1}{2}\nu\left(\sigma_{i+1,j+1/2+2k} + \sigma_{i+1,j+1/2-1}\right) \tag{2.31}$$

where $k = 0$ when $V_{i+1,j+1/2} > 0$ and $k = 1$ when $V_{i+1,j+1/2} < 0$. The artificial viscosity coefficient ν can be computed by one of two alternate methods discussed below. The simplest method is to apply the biasing at all points with ν calculated as

$$\nu_{i+1,j+1/2} = \left(1 - a^2M^2\right)_{i+1,j+1/2}. \tag{2.32}$$

The coefficient $\nu \rightarrow 1$ in the weak shock limit $M \rightarrow 1$, and for a perfect gas with $\gamma = 1.4$, $\nu \rightarrow 0.835$ in the strong shock limit, $M \rightarrow \infty$.

However when the crossflow is elliptic-type, artificial viscosity is not required. Shankar and Osher (1983) introduced an artificial viscosity which employs upwind

[2]This corresponds to density biasing, often referred to as artificial compressibility, in the case of the supersonic potential equation.

differencing based on the direction of the characteristic signal propagation which turns off the upwind differencing when the crossflow is elliptic-type. In this case, the artificial viscosity coefficient is given by

$$\nu_{i+1,j+1/2} = \mu \left[1 - \frac{a_{22} a^2}{V^2} \right]_{i+1,j+1/2}, \tag{2.33}$$

with

$$\mu = 0 \quad \text{for} \quad \left(a_{22} - \frac{V^2}{a^2} \right)_{i+1,j+1/2} > 0 \qquad \text{(elliptic-type crossflow)}, \tag{2.34}$$

$$= 1 \quad \text{for} \quad \left(a_{22} - \frac{V^2}{a^2} \right)_{i+1,j+1/2} < 0 \qquad \text{(hyperbolic-type crossflow)}. \tag{2.35}$$

Since, the density biasing is switched off when the crossflow is elliptic-type, this method typically produces sharper resolution of discontinuities.

2.3.3 Step Convergence

Given the α values at all previous levels, the differencing results in a set of nonlinear algebraic equations for α_{i+1} which are solved using Newton's method. In general, the artificial viscosity given by Eqn. 2.31 leads to a pentadiagonal system. For large Mach numbers where the artificial viscosity terms are small and for flows without strong shock-shock discontinuities, the derivative terms due to the artificial viscosity can often be neglected to give a tridiagonal system. In this case, more iterations may be required for convergence of each ξ step, but each iteration is significantly faster.

For most problems, a simple forward difference can be used for the initial estimate of α_{i+1} which is then converged. For problems with strong discontinuities or Mach numbers close to unity, a more accurate initial estimate is often needed. In order for the ξ-derivative term to be explicit in α, we locally linearize σU about the known values at the ith plane:

$$(\sigma U)_{i+1} \approx (\sigma U)_i + \frac{\partial (\sigma U)_i}{\partial \alpha} (\alpha_{i+1} - \alpha_i), \tag{2.36}$$

where

$$\frac{\partial(\sigma U)}{\alpha} = \frac{\partial \sigma}{\alpha} U + \sigma \frac{\partial U}{\partial \alpha}. \tag{2.37}$$

Substituting from the definitions of U and σ and grouping terms,

$$(\sigma U)_{i+1} \approx \sigma_i U_i + \sigma_i \left[\left(a_{11} - \frac{U^2}{a^2} \right)_i \frac{\partial}{\xi} + \left(a_{12} - \frac{UV}{a^2} \right)_i \frac{\partial}{\eta} \right] (\alpha_{i+1} - \alpha_i) . \tag{2.38}$$

The above linearized equation is explicit, having α_{i+1} as the unknown. However, the η-derivative term is still implicit due to the presence of $\tilde{\sigma}$. To force the step to be explicit, the retarded value is used, *i.e.*, $\tilde{\sigma}$ at the current level, $i+1$, is calculated based on the values at the previous level, i.

2.3.4 Boundary and Initial Conditions

Boundary conditions require that the shock front be normal to solid boundaries. If $\mathbf{n}$ is the unit vector normal to the boundary, the condition requires $\partial\alpha/\partial n = 0$ along the boundary. For the grid systems used, the boundary is assumed to be given by η = constant; therefore, the boundary condition reduces to $V = 0$. The initial conditions of α and Mach number are specified along an initial row, ξ = constant. Since the Mach number specifies the derivative of α, the values of α at the previous ξ can be estimated from the Mach number. Then with α values specified for two ξ rows, the solution can be advanced.

Bibliography

Bryson, A.E. and Gross, R.W.F. (1961) "Diffraction of strong shocks by cones, cylinders, and spheres," *J. Fluid Mech.*, **10**, 1–16.

Catherasoo, C.J. (1982) *Shock Dynamics in Non-Uniform Media*, Ph.D. Thesis, Graduate Aeronautical Laboratories, California Institute of Technology, Pasadena, California.

Henderson, L.F. (1980) "On the Whitham theory of shock-wave diffraction at concave corners," *J. Fluid Mech.*, **99**, 801–811.

Henshaw, W.D., Smyth, N.F., and Schwendeman, D.W. (1986) "Numerical shock dynamics using geometrical shock dynamics," *J. Fluid Mech.*, **171**, 519–545.

Schwendeman, D.W. (1993) "A new numerical method for shock wave propagation based on geometrical shock dynamics," *Proc. R. Soc. Lond. A*, **441**, 331–341.

Shankar, V. (1982) "Conservative Full Potential, Implicit Marching Scheme for Supersonic Flows," *AIAA J.*, **20**, 1508–1514.

Shankar, V. and Osher, S. (1983) "An Efficient, Full-Potential Implicit Method Based on Characteristics for Supersonic Flows," *AIAA J.*, **21**, 1262–1270.

Shankar, V., Szema, K.-Y., and Osher, S. (1985) "Treatment of Supersonic Flows with Embedded Subsonic Regions," *AIAA J.*, **23**, 41–48.

Whitham, G.B. (1957) "A new approach to problems of shock dynamics, Part I: Two-dimensional problems," *J. Fluid Mech.*, **2**, 145–171.

Whitham, G.B. (1959) "A new approach to problems of shock dynamics, Part II: Three-dimensional problems," *J. Fluid Mech.*, **5**, 369–386.

Chapter 3 Shock Focusing

The finite-difference numerical method for geometrical shock dynamics developed in the previous chapter is ideally suited for analysis of shock focusing problems which involve strong shock-shock discontinuities in the focal region. In the opening section, existing experimental results for shock focusing are reviewed. In Sections 3.2 and 3.3, results for the convergence and focusing of cylindrical portions of shocks is examined. The numerical results duplicate the different strong, moderate, and weak shock type behaviors observed in experiment. In Section 3.4, comparison is made between the numerical results and the focusing experiments of Sturtevant and Kulkarny (1976).

3.1 Previous Experimental Work

A number of experiments have examined the shock focusing problem. The experiments of Sturtevant and Kulkarny (1976) characterized the three primary types of shock focusing behavior using plane shocks reflected to a focus from parabolic reflectors. Interest in lithotripsy applications has led to additional experiments with weak shocks and elliptic reflectors in both gases (Holl 1982) and water (Müller 1987, 1989).

In the experiments of Sturtevant and Kulkarny (1976), plane shocks were reflected from parabolic reflectors to a point focus. The three types of focusing behavior observed are shown in Fig. 3.1 reproduced from Kulkarny (1976). Solid lines represent the shock fronts after reflection from the parabola shown at the left. For sound pulses in acoustic theory, the rays continue to a point focus; afterwards the shock front is crossed and folded as shown in Fig. 3.1(a). At the focus in acoustic theory, the ray tube area goes to zero and the shock amplitude is infinite. For weak shocks, Fig. 3.1(b), a Mach stem is formed near the focus. The triple point initially moves outward, but is eventually pushed back to the centerline, and the shock front becomes crossed and folded. For strong shocks, Fig. 3.1(d), a Mach stem is again formed, but

the triple point moves outward as the front advances past the acoustic focus. A transition case for moderate strength shocks is also observed, Fig. 3.1(c), where the triple point initially moves outward from the centerline. Further downstream, the triple point is swept back toward the centerline but never reaches the centerline. Instead the triple-point begins to move outward again. Later experiments with weak shocks have observed consistent behavior (Holl 1982, Müller 1987, 1989).

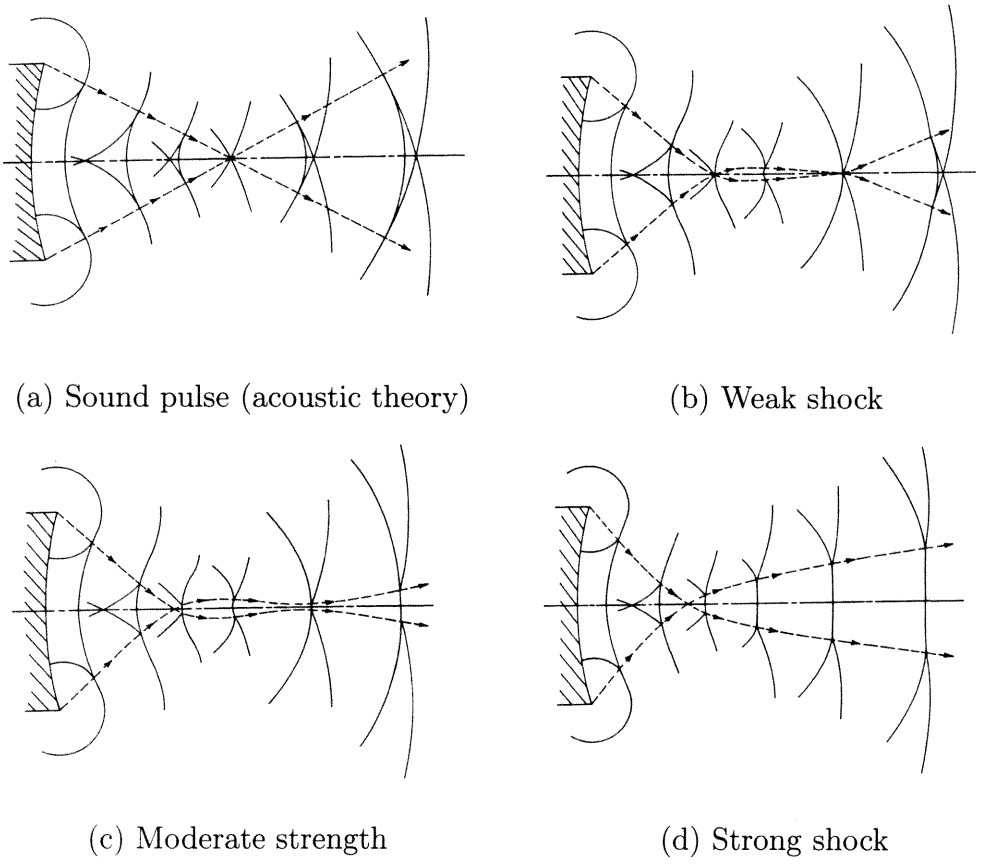

(a) Sound pulse (acoustic theory)

(b) Weak shock

(c) Moderate strength

(d) Strong shock

Figure 3.1: Types of focusing behavior observed in experiment [Reproduced from Kulkarny, 1976].

The shock strength near the focus of a shock wave lithotriptor, $M \sim 1.03 - 1.05$, corresponds to the weak shock case, Fig. 3.1(b). For these weaker shocks, the behavior near the focus approaches the prediction of acoustics. The focal amplification is higher, and the focal region is narrower and located nearer the acoustic focus than for stronger shocks (Sturtevant & Kulkarny 1976, Holl 1982).

Experimental studies have also examined the effect of the aperture angle of the

reflector on the location and pressure at the focus. For smaller aperture angles, corresponding to shallow reflectors, at equal initial Mach numbers, the focal pressure is lower and the focus is located further upstream of the acoustic focus than for larger aperture angles. For weak shocks with large aperture angles, the location of the maximum pressure can lie behind the acoustic focus. With stronger shocks or smaller aperture angles, the focus is located upstream of the acoustic focus (Sturtevant & Kulkarny 1976, Müller 1989).

To be considered successful, the numerical shock dynamics analysis should duplicate the strong, moderate, and weak focusing behavior observed experimentally. This entails accurately predicting the path of the triple-point seen experimentally, represented by a shock-shock in the current analysis. The path of the triple point is the most demanding element, since this defines the geometry of the flow near the focus. The parameters to compare include the shock front positions downstream of the focus, the shock pressure jump at the focus, and the location of the maximum pressure jump. The dependence of the focus parameters on the initial Mach number and the aperture angle of the initial front are also important features to replicate. The conditions behind the leading shock cannot be determined with the theory of shock dynamics.

3.2 Focusing Problem

In this section, the idealized problem of the convergence of a portion of a cylindrical shock front is considered. The problem can be expressed by two parameters shown in Fig. 3.2: the initial Mach number M_0 and the aperture angle of the front θ_0.

The lead disturbance from the corner travels inward along the C_+ characteristic originating at the corner. The arrival of this lead disturbance at the centerline signals the beginning of the focusing process. Until the arrival of the lead disturbance, the shock front is outside the region of influence of the corner, and the front is converging unaware of the diffraction at the corner. The arrival point of the lead characteristic in shock dynamics can be computed analytically. On the lead C_+ characteristic, the

compatibility relation gives

$$\theta_0 + \omega(M_0) = \theta_c + \omega(M_c), \tag{3.1}$$

where subscript c refers to values at the centerline. Since the angle of the flow at the centerline is zero, the centerline Mach number on arrival is given by:

$$\omega(M_c) = \theta_0 + \omega(M_0) \tag{3.2}$$

Before the arrival, the shock front is radially converging, so the area is simply the ratio of the final radius to the initial radius. The location of the arrival of the lead disturbance, x_c, non-dimensionalized by the initial radius is

$$x_c = -\frac{A(M_c)}{A(M_0)}. \tag{3.3}$$

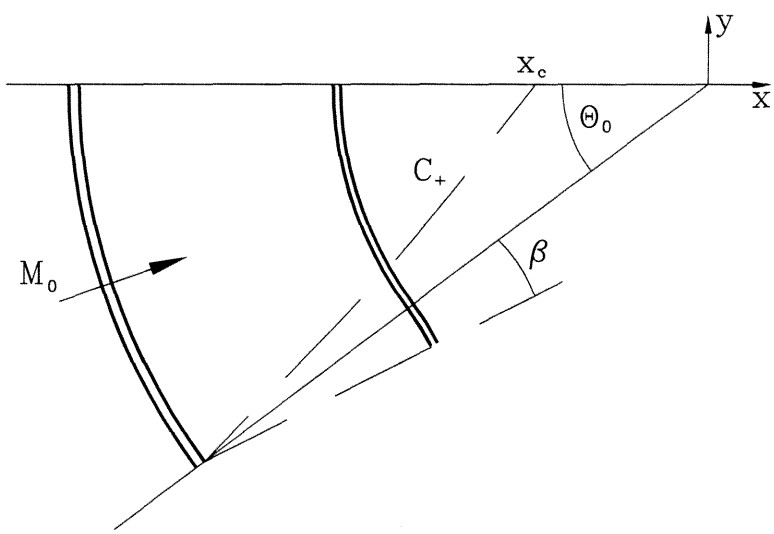

Figure 3.2: Focusing problem parameters: initial shock Mach number M_0 and the aperture angle θ_0.

Results for the centerline Mach number and normalized distance from the center of the original converging front are shown in Fig. 3.3 for initial aperture angles of 36°, 60°, and 80°, with $\gamma = 1.4$. For low Mach numbers the speed of the characteristic along the shock front is small, and the disturbance does not reach the centerline until

very near the acoustic focus. For this case, the amplification at the focus has increased to extremely high values. However, until the arrival of the lead disturbance, the Mach number will continue to increase, so the lead disturbance always must arrive before the acoustic focus. Only in the limit of initial Mach number of unity, the disturbance does not reach the centerline until the geometric focus and the results of acoustics are recovered. For smaller initial aperture angles, the disturbance has a shorter transverse distance to travel to reach the centerline; therefore, focusing begins further upstream of the acoustic focus at a lower Mach number.

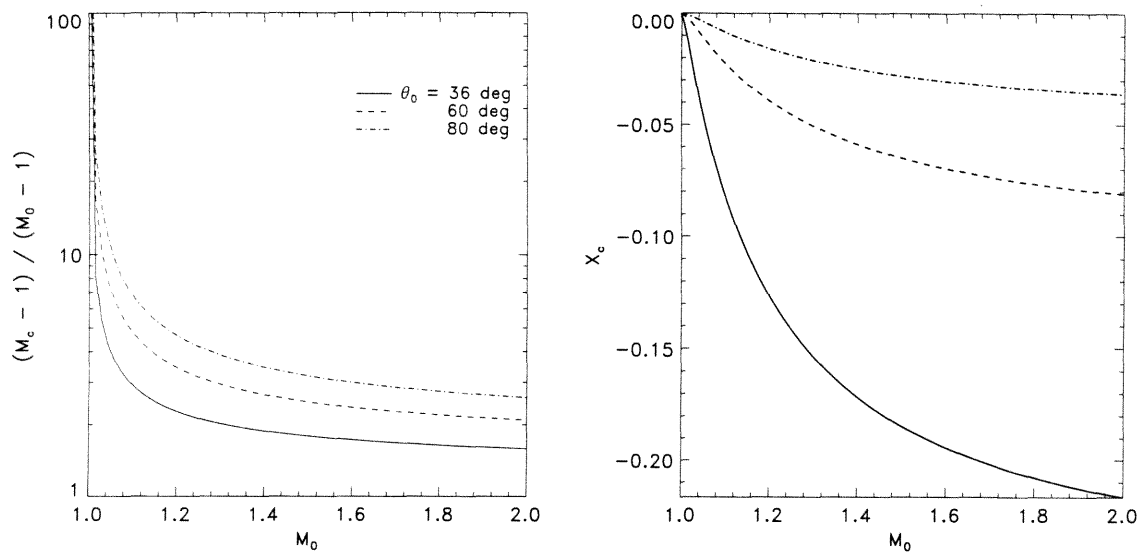

Figure 3.3: Mach number M_c and x-coordinate x_c of the arrival of first disturbance from the corner at the centerline as a function of aperture angle θ_0 and initial Mach number M_0.

This simple analysis is able to capture many of the aspects of the focusing behavior seen experimentally, since the velocity of the lead disturbance is directly related to how strongly nonlinear effects are felt. However, the arrival of the lead disturbance at the centerline marks only the beginning of the focusing process; a full numerical solution is required to resolve the focal region.

3.3 Numerical Results

Two aperture angles were considered for $\gamma = 1.4$, $\theta_0 = 36°$ and $\theta_0 = 80°$, both of which correspond to reflectors used in experiments (Sturtevant & Kulkarny 1976, Müller 1989). The aperture angle of $\theta_0 = 36°$ corresponds to the reflector ellipse used in the Dornier HM3 lithotriptor which has an eccentricity $e = 0.8$.

The initial condition specifies the shape of the shock front with the initial α values given along the line $\xi = 0$. The upper boundary at $\eta = 1$ is taken as a line of symmetry. The numerical treatment of the lower boundary depends on the initial Mach number. For a given M_0 there is a limit in shock dynamics to the maximum angle the front can be turned before $M = 1$ is reached,[1] denoted by the angle β in Fig. 3.2. When the initial Mach number is sufficiently high, the lower boundary is chosen parallel to the centerline. The numerical solution is then allowed to turn the shock front to a lower boundary parallel to the upper boundary. For weaker shocks, the lower boundary is placed at an angle to allow the shock front at the corner to be turned to a Mach number approaching unity. Provided a large enough angle is turned, the exact turning angle was observed to have only a weak effect on the focal region.

For cases where the maximum turning angle does not allow the upper and lower boundaries to be parallel, the grid is taken as a polar grid with an angle based on the aperture angle minus the maximum turning angle. This choice allows use of an orthogonal coordinate system which improves convergence. Since in this case the initial ξ row does not correspond to a shock front, the α and Mach number values are advanced to the start ξ analytically, since the front is just converging without effect from the corner. In no case is the shock front fitted using other methods; the initial values are always calculated using only shock dynamics.

For all cases, typical runs use several hundred grid points in the η-direction. For better resolution of the focal region, grid points are packed near the upper boundary.

[1] Continuing the analogy with the supersonic potential equation, the situation corresponds to the maximum turning angle in compressible flow where the flow can only be expanded until $\rho = 0$ where $M = \infty$.

The solution is marched at variable ξ steps chosen to maintain an average CFL number of unity.

Results for aperture angle $\theta_0 = 80°$ with initial Mach number $M_0 = 1.3$ are shown in Fig. 3.4 and Fig. 3.5. The upper figure, Fig. 3.4(a), shows the shock fronts which are contours of constant α. The normal to the fronts, which give the direction of the shock propagation, are shown in the center ray diagram, Fig. 3.4(b). Finally, the lower figure, Fig. 3.4(c), displays the contours of Mach numbers. A surface plot of the shock Mach number is shown in Fig. 3.5. For clarity, the solution at every grid point is not plotted on the surface plot which makes the discontinuity appear coarser than in the actual solution.

The maximum turning angle for $M_0 = 1.3$ is 88°, but to avoid excessive starting oscillations at the corner, a polar grid is used and the lower boundary is inclined slightly to the centerline. The front is advanced analytically to the start ξ row using shock dynamics theory. This portion of the solution is shown with dashed lines in the plots of shock fronts, Fig. 3.4(a), and Mach number contours, Fig. 3.4(c). In each of the three figures, the shock propagates left to right, and the original cylindrical front is shown as the darker line on the far left. The x, y coordinates are non-dimensionalized by the initial radius of the shock front with the center located at $(x, y) = (0, 0)$.

The $M_0 = 1.3$ case for $\theta_0 = 80°$ is an example of the strong-shock type behavior. The lead characteristic from the corner arrives at the centerline and turns the shock front out from the centerline which slows the Mach number increase. To maintain the boundary condition that the shock front is normal to the centerline, the shock-expansion from the corner reflects from the centerline as disturbances turning the flow back toward the centerline. These disturbances coalesce into a compression which eventually forms a shock-shock discontinuity. The shock-shock is clearly shown in the figures by the change in angle of the shock front and the increase in Mach number. The shock-shock advances outward throughout the solution. As the shock-shock propagates outward and the Mach stem extends in length, the discontinuity weakens and the Mach number behind the shock-shock decreases. Downstream of the focus, a large Mach stem is present which is slightly convex forward.

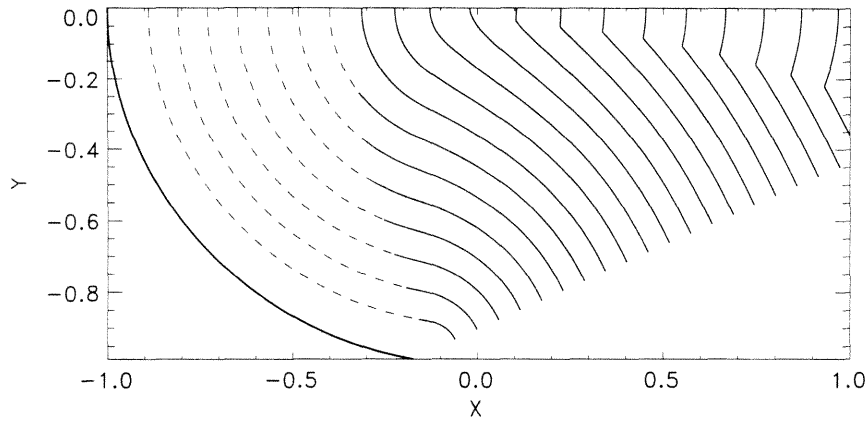

(a)

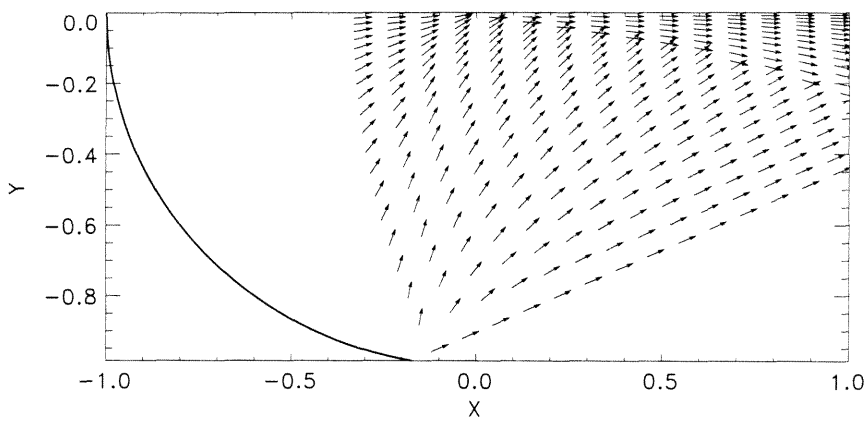

(b)

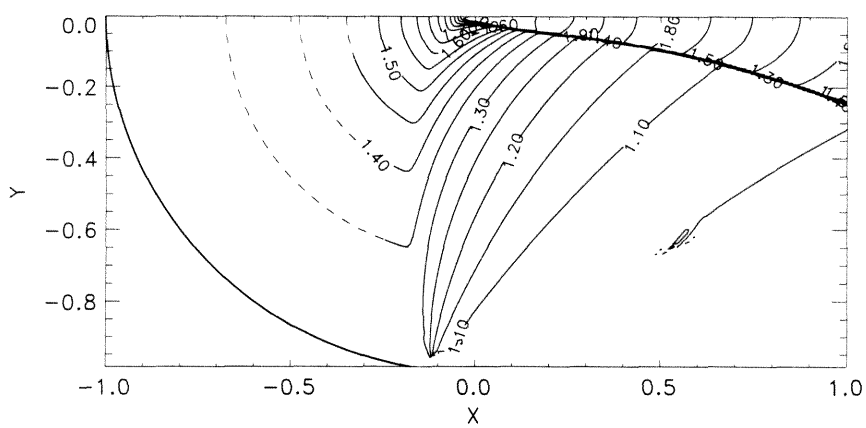

(c)

Figure 3.4: (a) Shock fronts, (b) shock front normals, and (c) Mach number contours for converging shock, $M_0 = 1.3$, $\theta_0 = 80°$, $\gamma = 1.4$. The center of the initial front lies at $(x, y) = (0, 0)$.

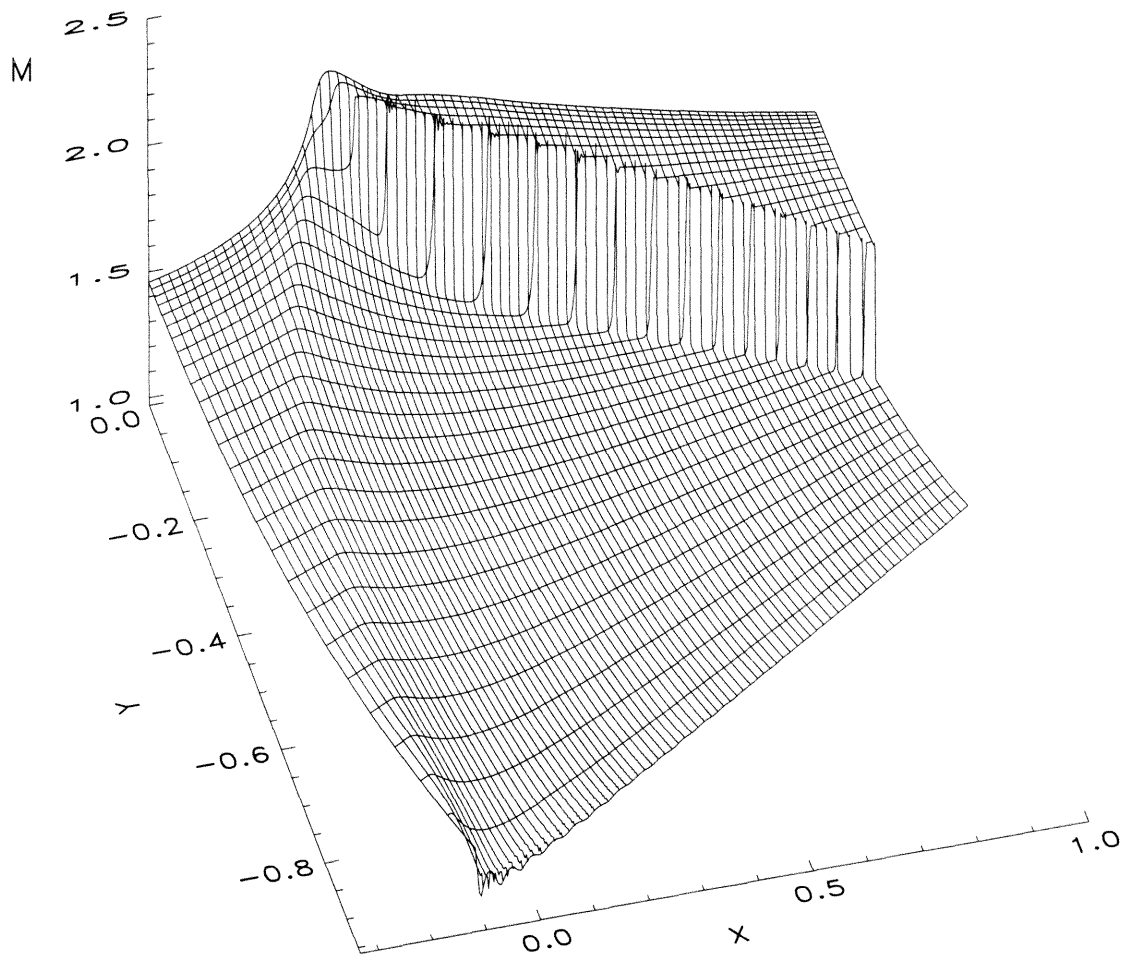

Figure 3.5: Mach number surface for converging shock, $M_0 = 1.3$, $\theta_0 = 80°$, $\gamma = 1.4$. The center of the initial front lies at $(x, y) = (0, 0)$. Slight overshoot is visible at the upper-edge of the shock-shock discontinuity.

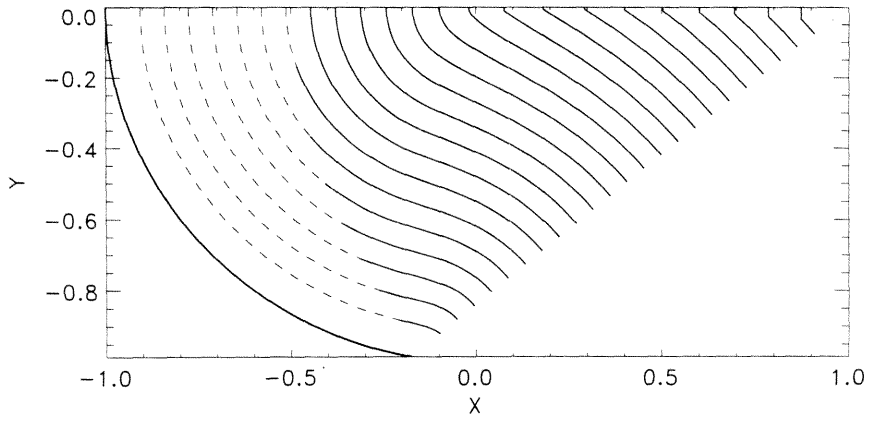

(a)

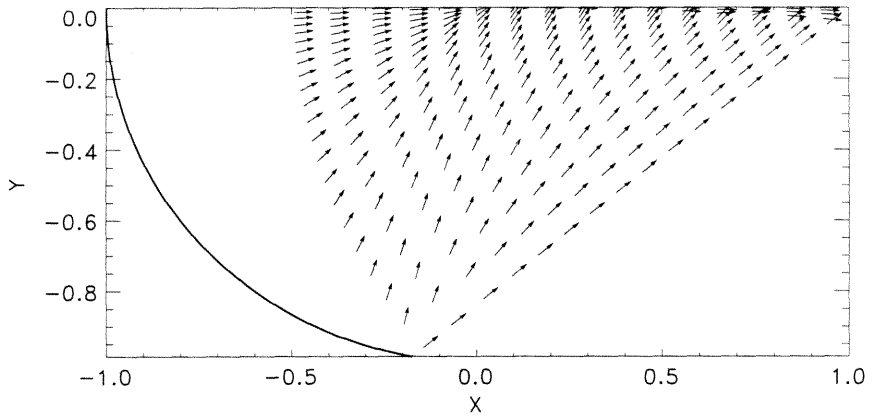

(b)

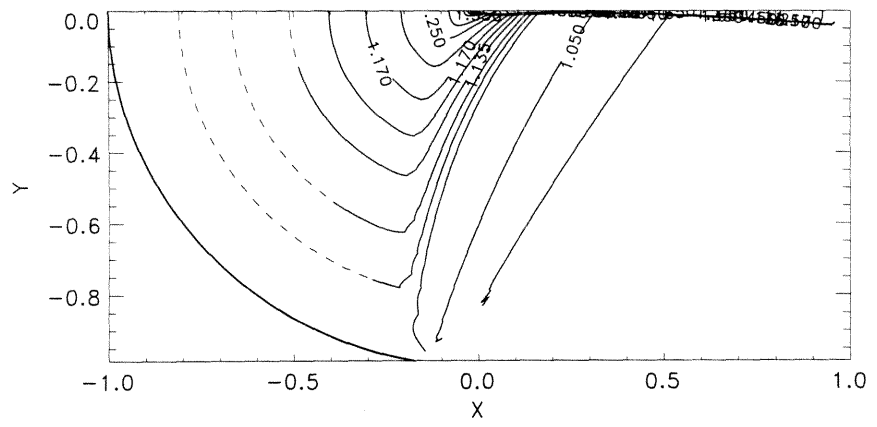

(c)

Figure 3.6: (a) Shock fronts, (b) shock front normals, and (c) Mach number contours for converging shock, $M_0 = 1.1$, $\theta_0 = 80°$, $\gamma = 1.4$. The center of the initial front lies at $(x, y) = (0, 0)$.

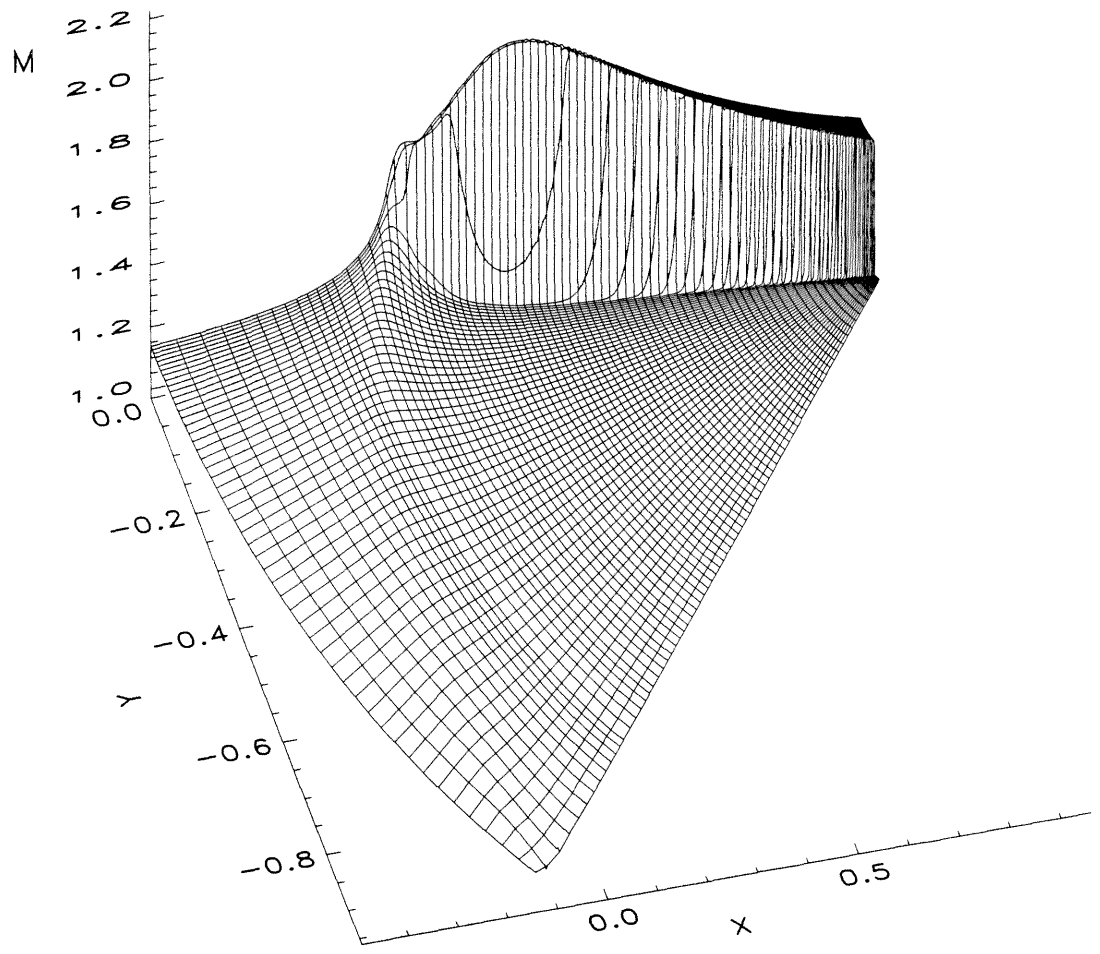

Figure 3.7: Mach number surface for converging shock, $M_0 = 1.1$, $\theta_0 = 80°$, $\gamma = 1.4$. The center of the initial front lies at $(x, y) = (0, 0)$. Slight overshoot is visible at the upper-edge of the shock-shock discontinuity.

An example of moderate shock behavior is shown in the next set of results for initial Mach number $M_0 = 1.1$ with the same aperture angle $\theta_0 = 80°$. Fig. 3.6(a) – (c) show the shock fronts, the rays normal to the shock front, and the contours of the shock Mach number. Fig. 3.7 displays the surface plot of the Mach number. The maximum turning angle for $M_0 = 1.1$ is 51°, so the lower grid boundary is inclined to the centerline.

The path of the disturbances from the corner can be clearly seen propagating inward on the Mach number contour plot and surface plot. The shock-expansion reflects from the wall and coalesces into a shock-shock discontinuity. Although the triple point propagates outward along the shock front, the shock front itself is still moving inward. The net result is that the shock-shock discontinuity is swept back toward the centerline. The strength of the shock-shock increases as it is pushed inward, producing a further increase in the centerline Mach number. The inward motion of the shock-shock forms a shoulder in the Mach number profile as shown in the Mach number surface plot, Fig. 3.7. The strength of the shock-shock continues to increase until the velocity of the shock-shock discontinuity along the shock front is sufficient for the shock-shock to begin to move outward. Downstream of the focus, a narrow Mach-stem is visible.

Similar behavior is seen for weaker shocks, with the arrival of the disturbance from the corner occuring nearer the acoustic focus. A shock-shock forms at the focus; however, the discontinuity is pushed back toward the centerline almost immediately and the open region is further reduced in size. For weak shocks, the shock-shock is pushed to several grid points from the centerline, and the path of the shock-shock becomes dependent on adequate grid resolution.

The path of the discontinuity is plotted superimposed over the solution grid for the region near the focus in Fig. 3.8. For each solution row, the location of the maximum Mach number gradient is displayed. From the left, the maximum gradient shows the path of the expansion from the corner. These disturbances reflect from the centerline and produce a compression discontinuity moving out from the centerline which coalesces into a discontinuity. For moderate and weak shock behavior, the

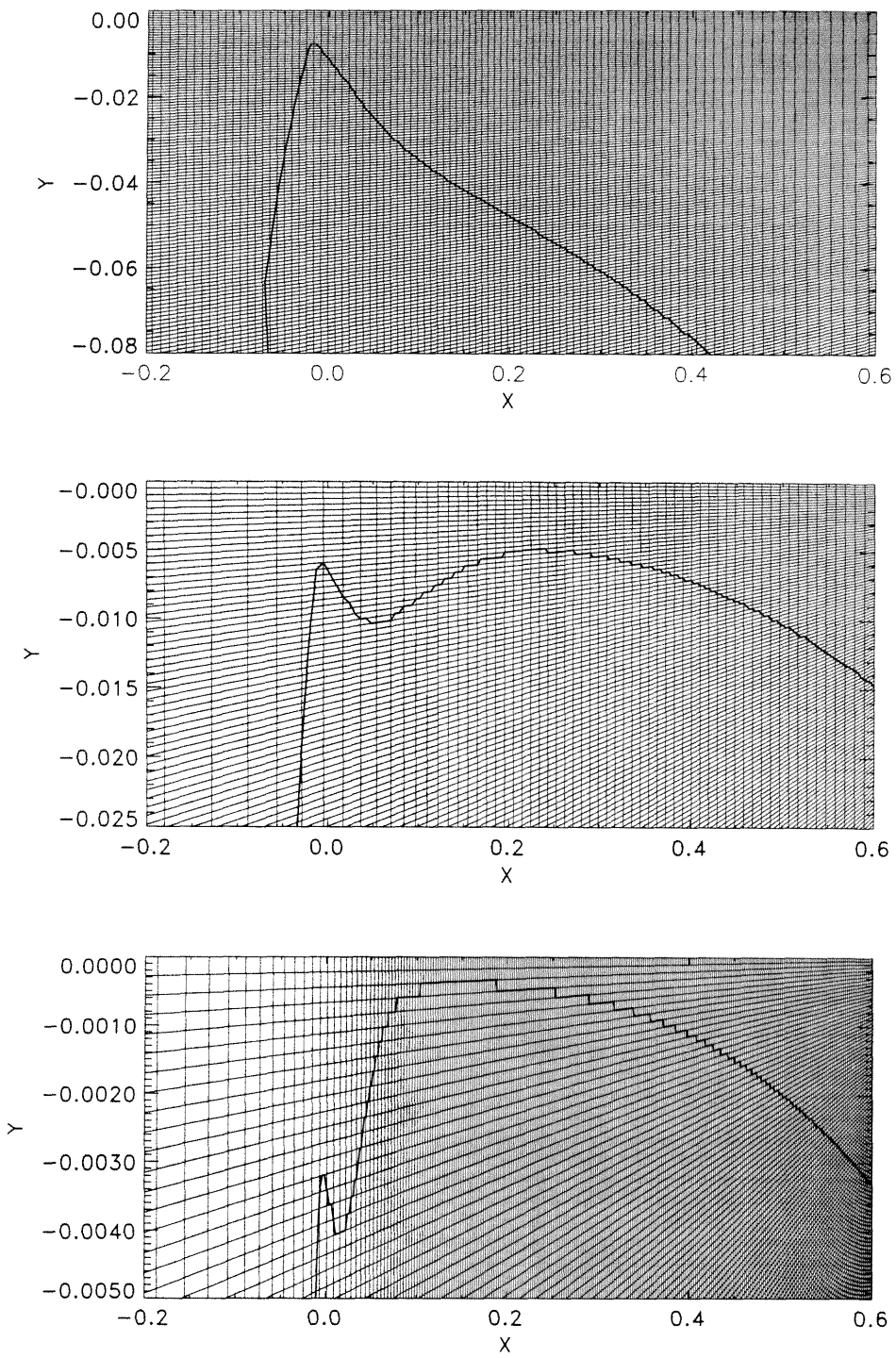

Figure 3.8: Location of maximum Mach number gradient near the focus for strong, $M_0 = 1.3$, moderate, $M_0 = 1.1$, and weak $M_0 = 1.05$, shock behavior for $\theta_0 = 80°$, $\gamma = 1.4$ superimposed over solution grid. For weak shock behavior, the discontinuity is immediately pushed to within several grid points of the centerline.

discontinuity propagates back toward the centerline and increases in strength until strong enough to begin to move outward. For moderate type behavior, adequate grid points exist to correctly resolve the distance of the discontinuity from the wall at closest approach. However for weak shock behavior, the discontinuity is immediately pushed to within several grid points of the centerline, even for much smaller grid spacings.

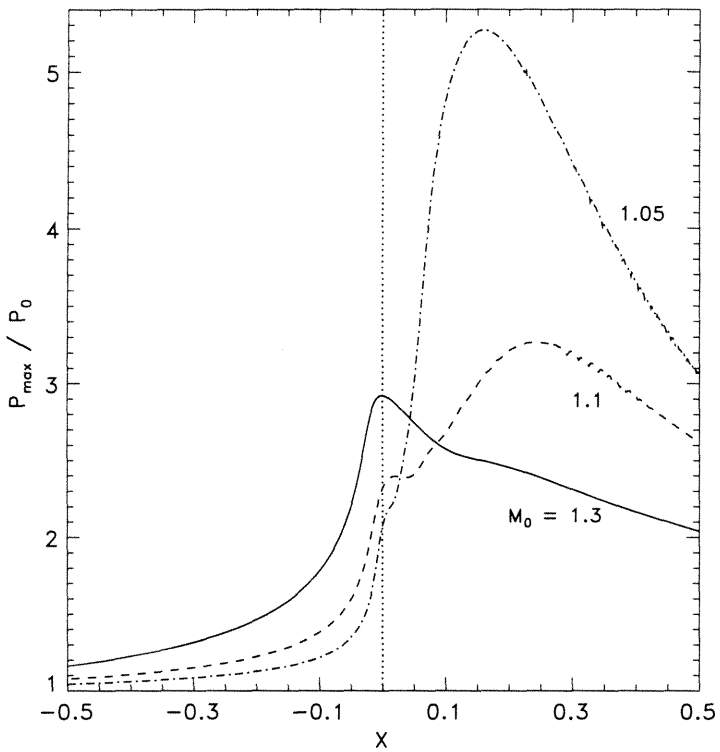

Figure 3.9: Centerline pressure ratios for varying initial Mach numbers, M_0, aperture angle $\theta_0 = 80°$, $\gamma = 1.4$. The center of the initial cylindrical front lies as $x = 0$.

Figure 3.9 plots the centerline pressure ratio for strong, $M_0 = 1.3$, moderate, $M_0 = 1.1$, and weak shock, $M_0 = 1.05$, cases for aperture angle $\theta_0 = 80°$. The pressure ratio is defined as the pressure behind the shock normalized by the pressure behind the initial shock. The x-coordinate is non-dimensionalized by the initial radius, and the acoustic focus lies at $x = 0$. For strong shock behavior, a single peak is formed slightly ahead of the acoustic focus. For the moderate and weak types of behavior, the initial peak occurs near the geometric focus when the corner disturbance arrives

at the centerline. An absolute maximum occurs further downstream when the shock-shock becomes strong enough to again move outward. For the weak case, $M_0 = 1.05$, the initial shoulder is only visible as a change of slope. From comparison with experiment, the shoulder on the centerline pressure for the weak cases is expected to mark where experiment shows a transition to regular reflection and the front becomes crossed and folded.

Results for the initial Mach numbers for a strong case, $M_0 = 1.1$, and a weak case, $M_0 = 1.01$, for a smaller aperture angle of $\theta_0 = 36°$ are shown in Figs. 3.10 – 3.13. Two major effects of the smaller aperture angle are seen in the results. The disturbance from the corner has less transverse distance to travel and reaches the centerline to start the focusing process further upstream. This also means the disturbance reaches the centerline at a lower Mach number, producing lower Mach numbers at the focus. Due to the lower Mach numbers, the onset of weak shock behavior occurs at a lower Mach number. For $\theta_0 = 36°$, moderate shock behavior is still seen at $M_0 = 1.1$, while weak shock behavior is seen at $M_0 = 1.01$.

A summary of the maximum Mach number and focus location from the numerical computations are shown in Fig. 3.14 for two aperture angles $\theta_0 = 36°$ and $\theta_0 = 80°$. The focus is taken as the location of the maximum centerline Mach number. The dashed line shows the location and Mach number at the arrival at the centerline of the lead disturbance from the corner in shock dynamics theory. For the weak shock and moderate shock type behavior, the location of the initial shoulder is denoted by the plus symbols. The results show that the arrival of the lead disturbance from the corner provides an accurate estimate of the beginning of the focal region. The actual maximum Mach number occurs further downstream as more of the bulk of the disturbance from the corner arrives.

For aperture angle $\theta_0 = 36°$, which corresponds to a deeper reflector, the focus occurs ahead of the acoustic focus, except for the very weak case $M_0 = 1.01$. For this case, even the initial shoulder forms slightly behind the acoustic focus. For $\theta_0 = 80°$, which corresponds to a deeper reflector, the location of the focus is behind the acoustic focus for weaker shocks. The focus Mach number is higher for the larger aperture

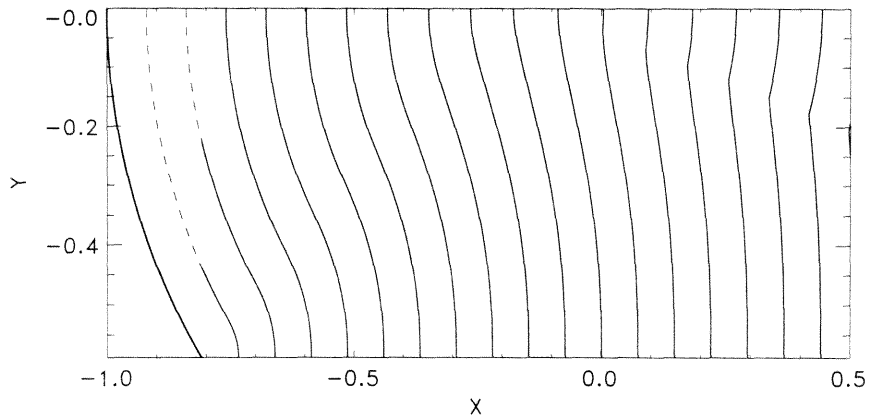

(a)

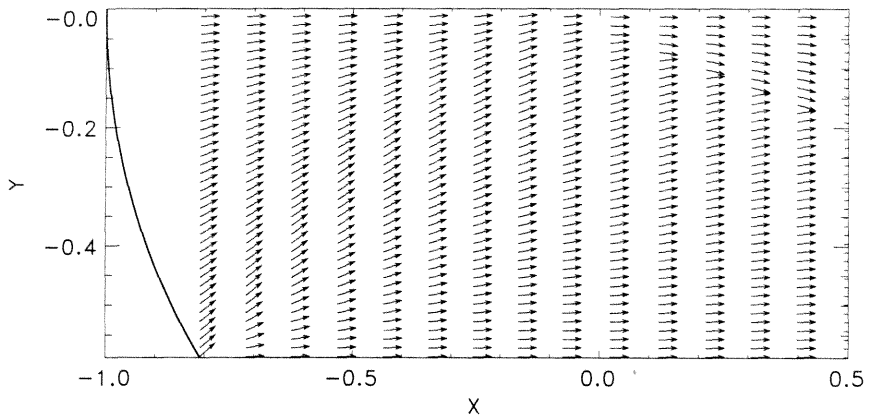

(a)

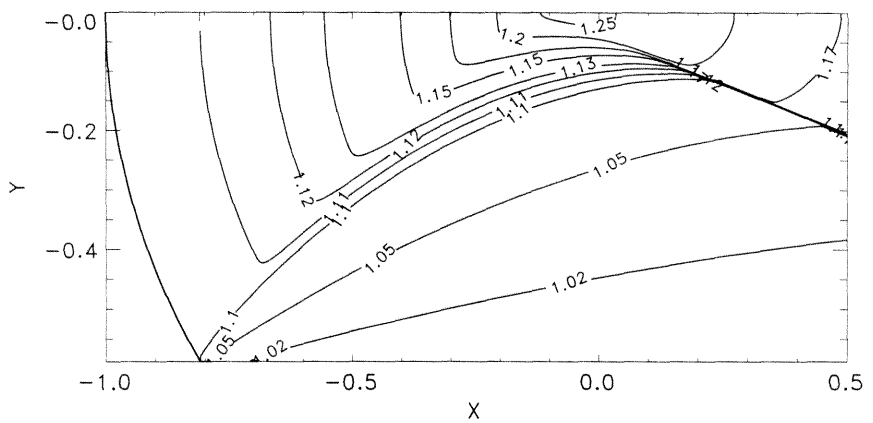

(a)

Figure 3.10: (a) Shock fronts, (b) shock front normals, and (c) Mach number contours for converging shock, $M_0 = 1.1$, $\theta_0 = 36°$, $\gamma = 1.4$. The center of the initial front lies at $(x, y) = (0, 0)$.

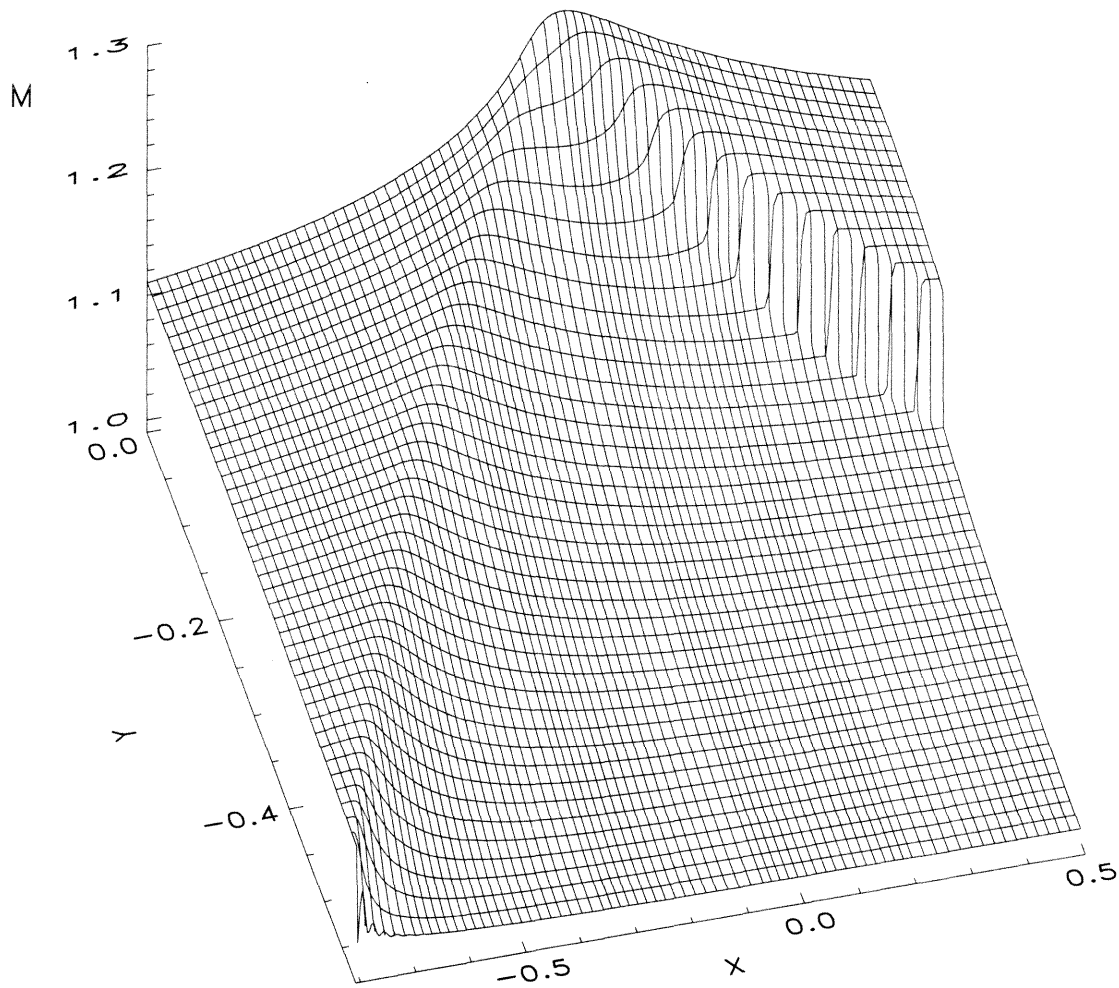

Figure 3.11: Mach number surface for converging shock, $M_0 = 1.1$, $\theta_0 = 36°$, $\gamma = 1.4$. The center of the initial front lies at $(x, y) = (0, 0)$.

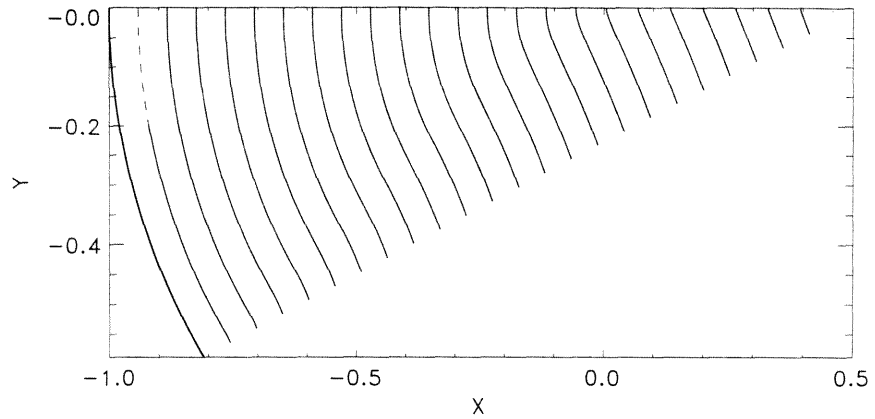

(a)

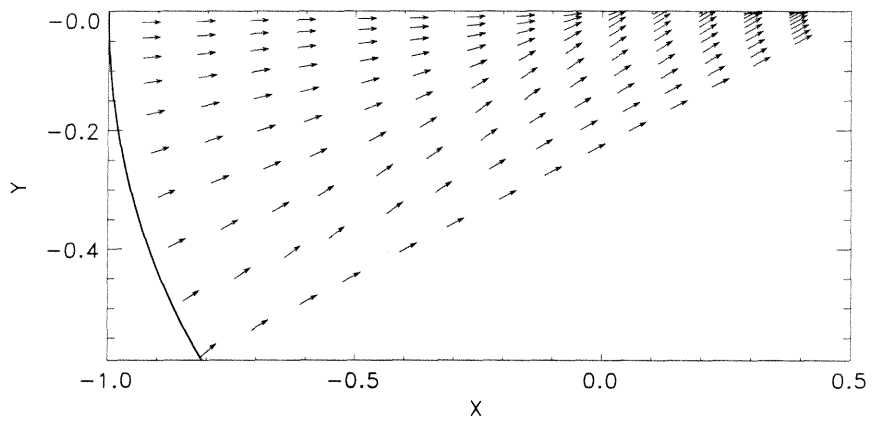

(a)

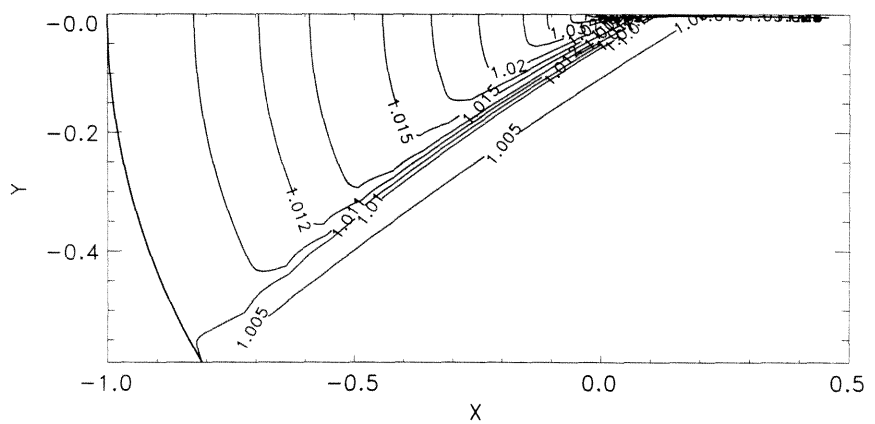

(a)

Figure 3.12: (a) Shock fronts, (b) shock front normals, and (c) Mach number contours for converging shock, $M_0 = 1.01$, $\theta_0 = 36°$, $\gamma = 1.4$. The center of the initial front lies at $(x, y) = (0, 0)$.

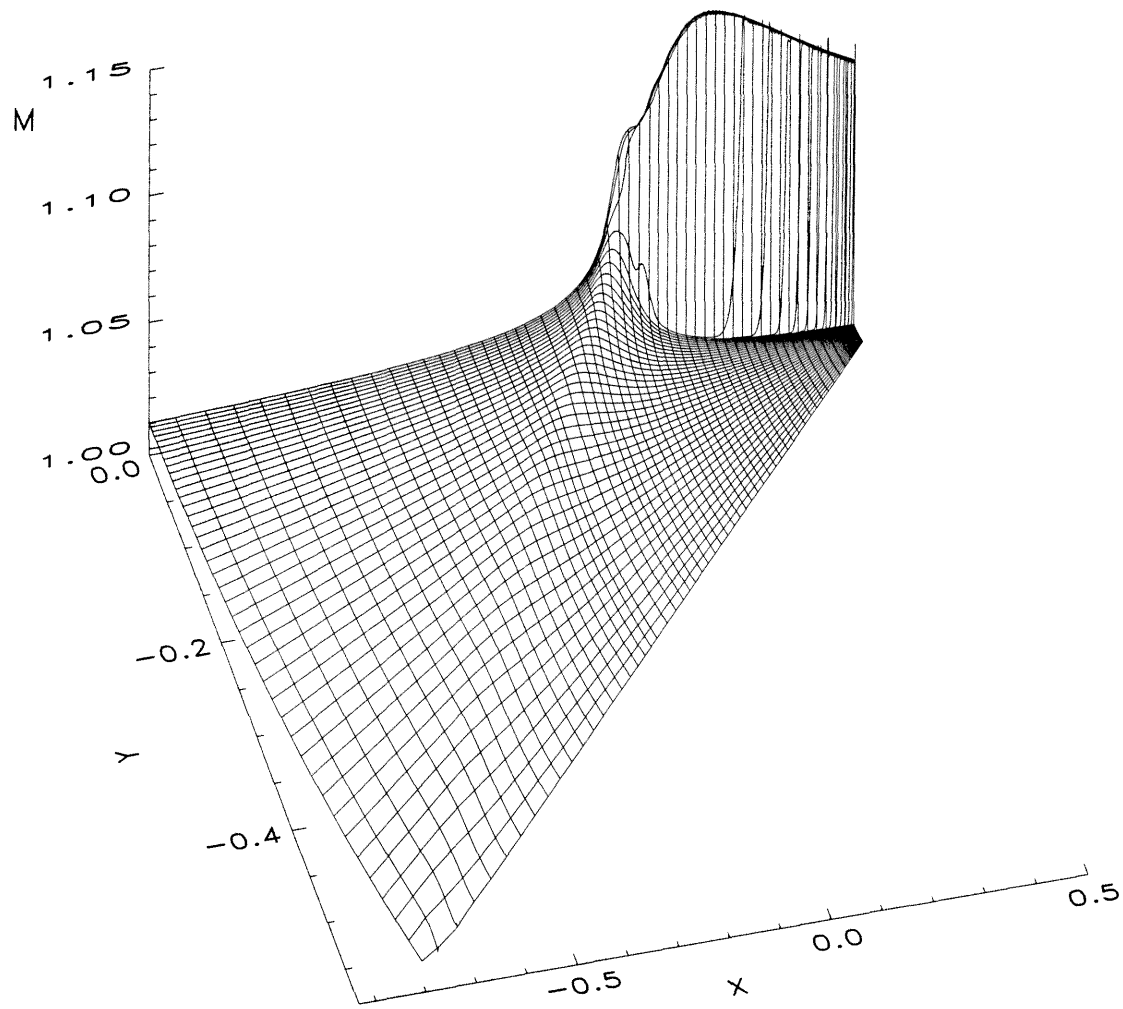

Figure 3.13: Mach number surface for converging shock, $M_0 = 1.01$, $\theta_0 = 36°$, $\gamma = 1.4$. The center of the initial front lies at $(x, y) = (0, 0)$. Slight overshoot is visible at the upper-edge of the extremely strong shock-shock discontinuity.

angle across the entire range of initial Mach numbers.

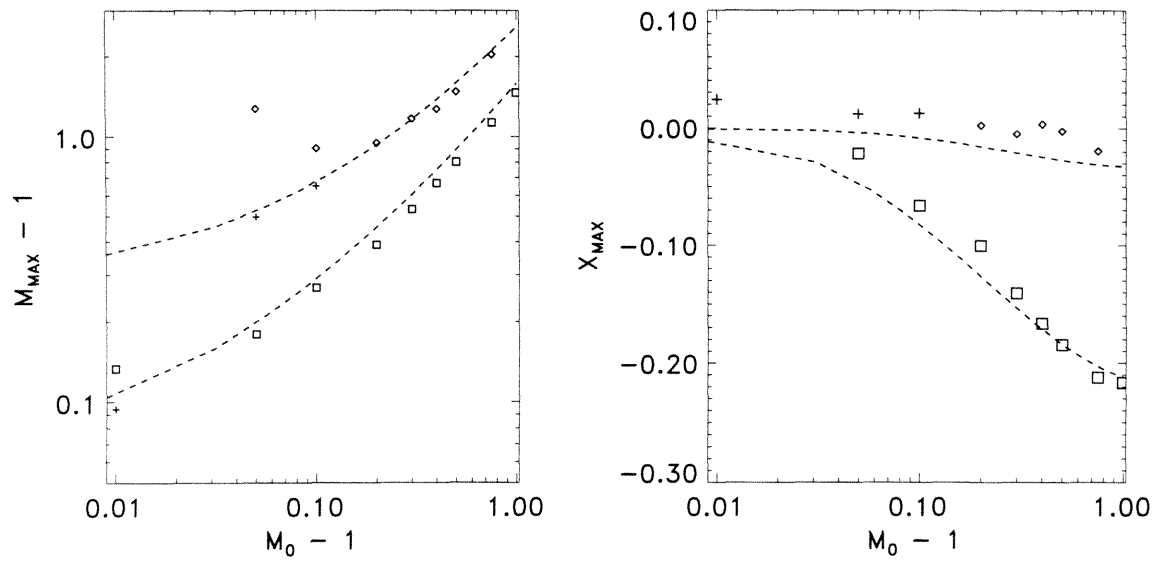

Figure 3.14: Maximum centerline Mach number and x-location of maximum for aperture angles $\theta_0 = 80°$ ($\diamond$) and $\theta_0 = 36°$ ($\square$), with $\gamma = 1.4$. For weak shocks, the location of the original peak is denoted by the + symbols. Dashed lines represent the arrival in shock dynamics of the lead disturbance from the corner.

3.4 Comparison with Experimental Results

The numerical shock dynamics method was used to calculate results for the focusing experiments of Sturtevant & Kulkarny (1976). In this series of experiments, plane shock waves were reflected from a parabola to a point focus in the 17" shock tube at GALCIT. An insert of square cross-section was used in the cylindrical tunnel; therefore, the problem is treated as two-dimensional, instead of axi-symmetric.

After reflection the shock propagates back into the uniform flow behind the incident shock. The problem can be treated with the general method developed in Chapter 4; however, since the velocity is uniform, a simple coordinate transformation is sufficient. If the uniform velocity is given by u_0, the freestream is at rest in the coordinate frame given by $x' = x + u_0 t$. Therefore, at any point on the shock front

$\alpha(\mathbf{x}') = a_0 t$, the physical x-coordinate value must be computed as

$$x = x' + \left(\frac{u_0}{a_0}\right)\alpha. \tag{3.4}$$

Provided the initial conditions are specified properly in the (x', y) coordinate system, the problem can be solved with the present numerical scheme.

A parabolic grid is used for the calculation so the parabolic reflector is a line of constant ξ, and the initial conditions are specified along the reflector. The initial α values are calculated from the arrival time of the incoming shock at each point on the reflector. The Mach number is taken as the Mach number of the initial planar shock, since the oblique shock relations predict regular reflection along the entire parabola. Computations using the reflected-shock Mach number from the full oblique shock relations show that the variation in initial Mach number along the reflector has only a small effect on the focal region. The outer corner is treated as described in Section 3.2.

The computed reflected shock fronts and Mach number contours for strong shock type behavior with initial Mach number $M_0 = 1.3$ and moderate type with $M_0 = 1.1$ are shown in Fig. 3.15 for the parabolic reflector with half-angle of 80°. The shock fronts are shown in the upper set of figures, and contours of shock Mach number are shown below. The x, y coordinates are non-dimensionalized by the focal length of the parabola. The outline of the reflector is shown at the left of each figure. The focus of the parabola lies on the centerline at $(x, y) = (0, 1)$.

Fig. 3.15(a) shows an example of the strong shock type behavior observed for $M_0 = 1.3$. As seen for the earlier cases, the initial disturbance from the corner of the parabola travels along the shock front until it reaches the centerline, where a shock-shock discontinuity forms on the shock to enforce the boundary condition. The uniform velocity pushes the location of the maximum pressure further upstream of the acoustic focus. The path of the shock-shock propagating outward along the shock front represents the path of the triple-point seen experimentally. As the discontinuity propagates outward, it weakens and the Mach number behind the shock-shock de-

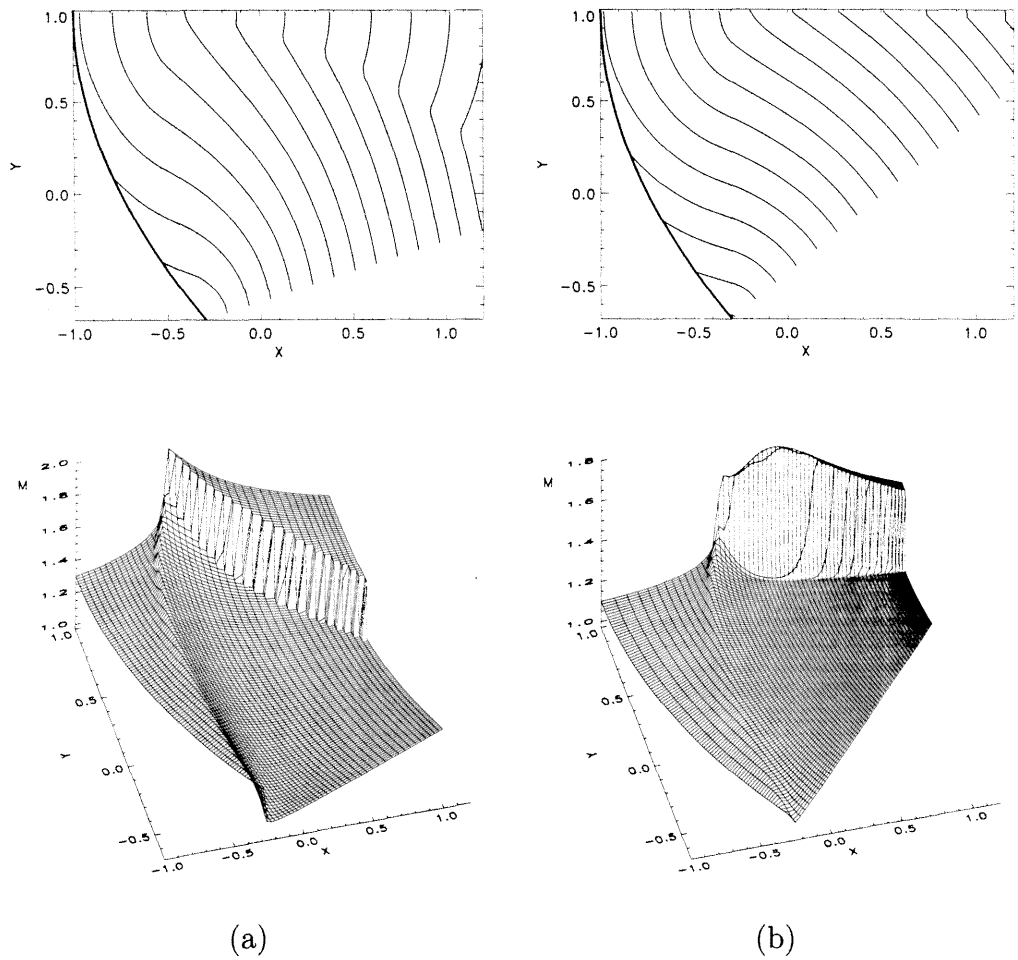

(a) (b)

Figure 3.15: Shock fronts and Mach number surface for for reflection of planar shock waves from a parabola with initial Mach number (a) $M_0 = 1.3$ and (b) $M_0 = 1.1$, $\gamma = 1.4$.

creases. For moderate strength shock waves, the triple point does not immediately propagate outward, but is initially swept back toward the centerline causing a further increase in Mach number as shown in Fig. 3.15(b) for $M_0 = 1.1$. For the moderate case, the transition period when the shock-shock moves toward the centerline is elongated by the uniform velocity.

The computed pressure amplification and shock-shock path are compared with the experimental results in Fig. 3.16. The pressure amplification is defined as the pressure jump across the shock normalized by the pressure jump of the reflected shock as it leaves the reflector surface. The experimental pressure is the maximum

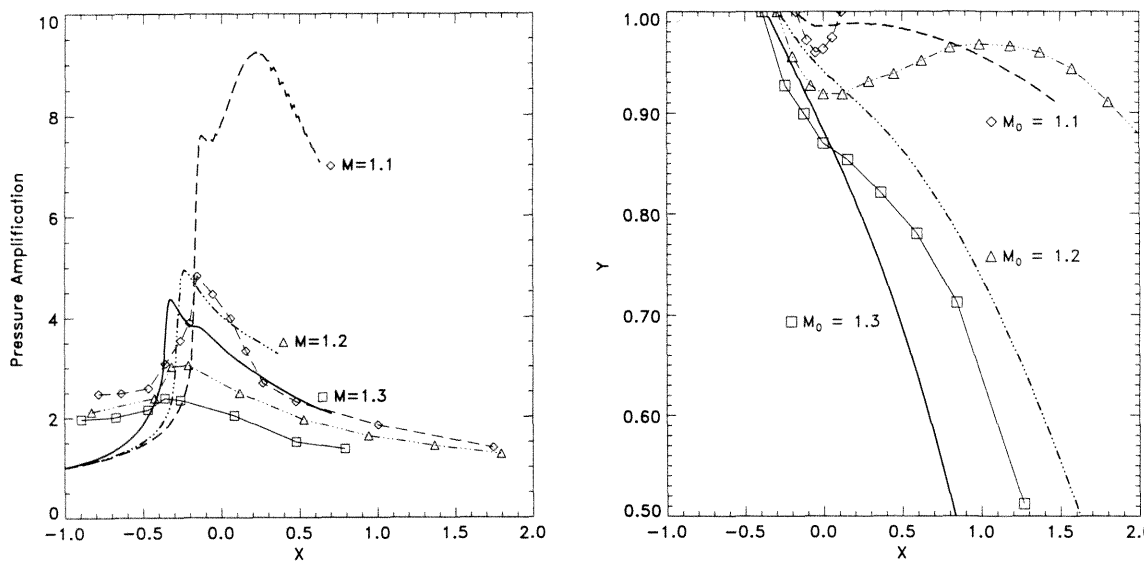

(a) (b)

Figure 3.16: (a) Pressure amplification and (b) shock-shock path computed for reflection of planar shock waves from a parabola compared with experimental results of Sturtevant and Kulkarny (1976). The numerical results are shown as lines without symbols, experimental results are corresponding line types with symbols. The experimental pressure amplification is based on the maximum pressure which outside the focal region is not the pressure directly at the shock.

pressure, which outside the focal region is not the pressure directly at the shock. The approximate shock dynamics theory cannot provide the pressure behind the shock. However, within the focal region, the maximum pressure observed is the shock pressure jump and comparison can be made with the results of shock dynamics. For the strong case $M_0 = 1.3$, the shock dynamics pressure is twice the experimental results, but the overprediction falls to a factor of 1.5 for $M_0 = 1.1$. The overprediction is not significantly affected by accounting for the finite size of the pressure transducer. Within the focal region, the numerical results correctly predict the location of the maximum pressure for the stronger shocks. For the moderate strength case, the location of the original peak corresponds well to the experimental focus location, but the additional rise in the Mach number due to the requirement for Mach reflection at the centerline is not seen experimentally.

The path of the shock-shock is one of the most exacting comparisons since the

effect is sensitive to nonlinear effects. The path is well-predicted for $M_0 = 1.3$, but for weaker shocks the agreement deteriorates. Whereas moderate type behavior was seen experimentally for $M_0 = 1.2$, shock dynamics does not show this behavior until a lower Mach number. However, the shock dynamics approximation is able to capture the moderate type behavior of the shock-shock being swept towards the centerline for $M_0 = 1.1$. For all cases, the origin of the shock-shock agrees closely with the origin of the triple point observed in the experiments.

From an analysis of a straight shock diffracting around a corner with a small turning angle, Whitham (1957) showed that the speed of the initial signal predicted by shock dynamics is half the value from the full gas-dynamics relations. However even for weak shocks, Whitham demonstrated that the total magnitude of the disturbance is quite accurate. Examining the current focusing problem, the diffractive disturbance from the corner arrives at the centerline too late in shock dynamics, after the Mach number and pressure have reached too high a value. The shock-shock discontinuity then has too high a speed outward from the centerline as seen in the comparison with experimental results.

For a valid comparison with experimental results, the focal region must be adequately resolved numerically. Too coarse a grid or high artificial viscosity can reduce the maximum Mach number at the focus, leading to an artificial agreement with experiment and an over-optimistic assessment of the accuracy of shock dynamics. This is especially true for very weak shocks where the focal region becomes extremely sensitive to grid resolution.

3.5 Conclusions

The finite-difference method developed for geometrical shock dynamics can efficiently solve shock focusing problems where strong shock-shock discontinuities occur. The numerical results qualitatively capture the strong, moderate, and weak shock types of behavior observed in experiment. The major effects of the aperture angle and initial Mach number predicted by geometrical shock dynamics agree with results seen

experimentally. In comparison with experiments of Sturtevant and Kulkarny (1976), the location of the focus is accurately predicted. Due to the underprediction of the speed of the corner disturbance by shock dynamics, the pressure at the focus is overpredicted, which leads to too high a speed of the shock-shock out from the centerline. Agreement deteriorates somewhat for weaker shocks, as expected with shock dynamics.

Bibliography

Holl, R. (1982) *Wellenfokussierung in Fluiden*, Dissertation, Aachen.

Kulkarny, V.A. (1975) *An Experimental Investigation of Focusing of Weak Shock Waves in Air*, Ph.D. Thesis, Graduate Aeronautical Laboratories, California Institute of Technology, Pasadena, California.

Müller, M. (1987) "Experimental Investigations of Focusing of Weak Spherical Shocks Waves in Water by Shallow Ellipsoidal Reflectors," *Acustica*, **64**, 85–93.

Müller, M. (1988) "Experimentelle Untersuchungen zur Fokussierung sphärischer Stoßwellen in Wasser durch tiefe ellipsoide Reflektoren," *Acustica*, **66**, 258–266.

Müller, M. (1989) "Die Fokussierung von Wasserstoßwellen zur Lithotripsie durch verschiedene Ellipsoidreflektoren," *Biomedizinische Technik*, **34**, 62–72.

Sturtevant, B. and Kulkarny, V.A. (1976) "The focusing of weak shock waves," *J. Fluid Mech.*, **73**, 651–671.

Takayama, K. (1993) "Application of Underwater Shock Wave Focusing to the Development of Extracorporeal Shock Wave Lithotripsy," *Jpn. J. Appl. Phys.*, **32**, 2192–2198.

Whitham, G.B. (1957) "A new approach to problems of shock dynamics, Part I: Two-dimensional problems," *J. Fluid Mech.*, **2**, 145–171.

Chapter 4 Generalized Equations of Shock Dynamics

In Chapter 2, a numerical method for a shock propagating into a uniform gas at rest was developed. In the current chapter, the theory of geometrical shock dynamics is extended to the case of a shock propagating into a general, non-uniform fluid in motion.

In Section 4.1, the equation is derived for shock propagation into a fluid in motion, the primary additional complexity being that the rays are no longer normal to the front. In Section 4.2, the appropriate Area-Mach relation is developed for varying properties upstream with a general equation of state. As an example, the equations for a mixture of perfect gases are expanded in Section 4.3. In Section 4.4, the finite-difference numerical method developed previously is extended to the more general problem. In conclusion, the final section presents results for shock propagation over cylindrical gas inhomogeneities.

4.1 Development

To begin, the function $\alpha(\mathbf{x}) = t$ is defined as the shock front position at time t. Defining the vector $\mathbf{n}$ as the unit normal to the front as shown in Fig. 4.1, the normal vector follows from the definition of α:

$$\mathbf{n} = \frac{\nabla\alpha}{|\nabla\alpha|}. \tag{4.1}$$

Considering the differential motion of a point on the shock front from $\alpha(\mathbf{x}) = t$ to $\alpha(\mathbf{x} + \mathrm{d}\mathbf{x}) = t + \mathrm{d}t$, the normal velocity of the front can be expressed in terms of the

gradient of α:

$$V_S = \frac{1}{|\nabla\alpha|}. \tag{4.2}$$

The total normal velocity is the normal velocity of the shock relative to the freestream velocity, U_S, plus the component of the freestream velocity along the normal:

$$V_S = U_S + \mathbf{u}_0 \cdot \mathbf{n}. \tag{4.3}$$

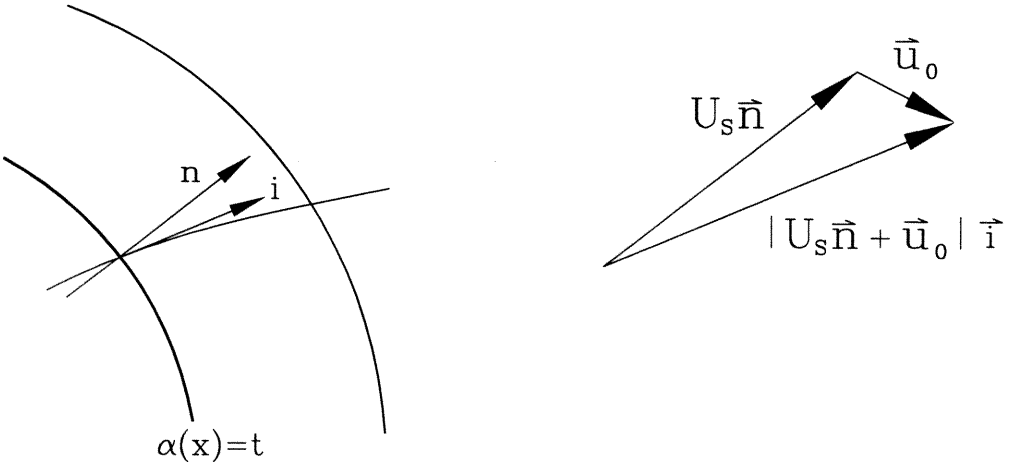

Figure 4.1: Shock front geometry showing normal and ray vector geometry.

Due to the uniform velocity, the rays are no longer orthogonal to the front; therefore, $\mathbf{i}$ is introduced as the unit vector along the ray. Since the shock front will propagate at the normal velocity of the shock itself, U_S, plus the freestream velocity, the ray vector is

$$\mathbf{i} = \frac{U_S\mathbf{n} + \mathbf{u}_0}{|U_S\mathbf{n} + \mathbf{u}_0|}. \tag{4.4}$$

Applying the divergence theorem to the ray tube between two successive shock positions (Whitham, 1968), the ray-tube area can be directly related to the divergence of the rays:

$$\nabla \cdot \frac{\mathbf{i}}{A_r} = 0, \tag{4.5}$$

where the area A_r is defined as proportional to the cross-sectional area of a ray-tube. The ray-tube area is related to the normal area as $A_r = A(\mathbf{i} \cdot \mathbf{n})$.

Substituting the expressions for the normal and ray vectors, Eqn. 4.5 can be

simplified to

$$\nabla \cdot \left[\frac{U_S}{A} \left(\nabla\alpha + \frac{\mathbf{u}_0}{U_S V_S} \right) \right] = 0. \tag{4.6}$$

For zero uniform velocity, the second term immediately disappears and the familiar relation of Chapter 2 is recovered. For the special case of u_0 constant, the equation can be simplified to the form given by Whitham (1968).

Eqn. 4.6 provides the governing equation for the motion of the shock front. At this point, the development is still general: Eqn. 4.6 follows only from the shock front definition as $\alpha(\mathbf{x}) = t$, with the assumption that the shock front moves at its normal velocity plus the freestream velocity. To proceed further to a differential equation for $\alpha(\mathbf{x})$, an expression for the area as a function of the shock strength is required. As in Whitham's original theory of shock dynamics, the shock propagation down each ray tube is treated as a shock propagating down a tube with solid walls. The variation of area along the ray tube is taken as the area variation along the tube. Provided a relation is known between the shock strength and area, the system is closed.

4.2 General Area Relation

To develop a general area relation, the problem of propagation of a shock down a tube with slowly-varying area is considered. The shock relations are applied directly along the C_+ characteristic from the continuity and momentum equations for the 1-D problem. Including body forces, along the C_+ characteristic:

$$\frac{\mathrm{d}p}{\mathrm{d}s} + \rho a \frac{\mathrm{d}u}{\mathrm{d}s} + \frac{\rho u a^2}{u+a} \frac{1}{A} \frac{\mathrm{d}A}{\mathrm{d}s} - \frac{\rho a}{u+a} F = 0, \tag{4.7}$$

where s is the distance along the channel. The p, u, ρ, and a values behind the shock from the shock relations are substituted directly into Eqn. 4.7. Whitham (1958) showed this approach is equivalent to Chisnell's (1957) treatment as a series of small area changes where disturbances overtaking the shock from behind are ignored.

To postpone any assumptions about the fluid equation of state, the pressure and velocity derivatives will be expanded into two terms. The first term contains the

contributions from changes in the shock front velocity. The second term, the total derivative at constant U_S, contains all contributions from changes in the freestream ahead of the shock:

$$\frac{\mathrm{d}p}{\mathrm{d}s} = \frac{\partial p}{\partial U_S}\frac{\mathrm{d}U_S}{\mathrm{d}s} + \left(\frac{\partial p}{\partial s}\right)_{U_S}, \tag{4.8}$$

$$\frac{\mathrm{d}u}{\mathrm{d}s} = \frac{\partial u}{\partial U_S}\frac{\mathrm{d}U_S}{\mathrm{d}s} + \left(\frac{\partial u}{\partial s}\right)_{U_S}. \tag{4.9}$$

Substituting the derivatives into Eqn. 4.7 gives a differential area relation for the generalized system:

$$\frac{\mathrm{d}A}{A} + f\left(U_S, ()_0\right)\mathrm{d}U_S + S\left(U_S, ()_0\right) = 0. \tag{4.10}$$

Both f and S are functions of the shock velocity and the upstream conditions, denoted by $()_0$. Simplifying,

$$f = \left(\frac{u+a}{\rho u a^2}\right)\left(\frac{\partial p}{\partial U_S} + \rho a\frac{\partial u}{\partial U_S}\right), \tag{4.11}$$

$$S = \left(\frac{u+a}{\rho u a^2}\right)\left[\left(\frac{\partial p}{\partial s}\right)_{U_S} + \rho a\left(\frac{\partial u}{\partial s}\right)_{U_S}\right] + \frac{F}{ua}. \tag{4.12}$$

The contributions due to the area-change, due to changes in the shock front normal velocity relative to the upstream velocity, and due to the upstream conditions are separated into different terms. The partial terms must include the effect of all changes upstream, from both changes in fluid state and changes in fluid composition, including gradients in freestream velocity ahead of the advancing shock.

Because of the assumption that the shock conditions can be applied along the C_+ characteristic, the shock jump conditions for the appropriate equation of state can be used to evaluate the differential terms in the equations for f and S. With the equation of state for the fluid, the system can be completely expressed in terms of the velocity of the shock front and the upstream conditions. In general, the terms may include both the shock strength, represented by U_S, and the upstream conditions.

4.3 Perfect Gas Case

As an example, the case is considered of a perfect gas where the freestream conditions along with the composition of the gas vary, including the effect of uniform velocity. The area relation for this problem for zero uniform velocity is available for comparison (Catherasoo 1983).

Two thermodynamic variables, p_0 and a_0, are used to describe the freestream state with the upstream velocity normal to the shock front given by u_{0n}. The variation of perfect gas composition requires an additional term for the change in γ. Therefore, the upstream contribution terms are expanded into four terms as follows:

$$\left.\frac{\mathrm{d}p}{\mathrm{d}s}\right|_{U_S} = \frac{\partial p}{\partial p_0}\frac{\mathrm{d}p_0}{\mathrm{d}s} + \frac{\partial p}{\partial a_0}\frac{\mathrm{d}a_0}{\mathrm{d}s} + \frac{\partial p}{\partial u_{0n}}\frac{\mathrm{d}u_{0n}}{\mathrm{d}s} + \frac{\partial p}{\partial \gamma}\frac{\mathrm{d}\gamma}{\mathrm{d}s} \tag{4.13}$$

$$\left.\frac{\mathrm{d}u}{\mathrm{d}s}\right|_{U_S} = \frac{\partial u}{\partial p_0}\frac{\mathrm{d}p_0}{\mathrm{d}s} + \frac{\partial u}{\partial a_0}\frac{\mathrm{d}a_0}{\mathrm{d}s} + \frac{\partial u}{\partial u_{0n}}\frac{\mathrm{d}u_{0n}}{\mathrm{d}s} + \frac{\partial u}{\partial \gamma}\frac{\mathrm{d}\gamma}{\mathrm{d}s} \tag{4.14}$$

The derivatives in the Area-Mach relation are along the ray tube, so the upstream velocity term contains the velocity component normal to the shock, u_{0n}.

Using the standard normal shock relations, the derivatives can be expressed in terms of M_w, the Mach number of the shock relative to the fluid velocity ahead of the shock. The pressure partial derivative terms are given by:

$$\frac{\partial p}{\partial p_0} = 1 + \frac{2\gamma}{\gamma+1}\left(M_w^2 - 1\right) \qquad \frac{\partial p}{\partial a_0} = \frac{-4\gamma}{\gamma+1}\left(\frac{p_0}{a_0}\right)M_w^2 \tag{4.15}$$

$$\frac{\partial p}{\partial u_{0n}} = \frac{\partial p}{\partial a_0} \qquad \frac{\partial p}{\partial \gamma} = \frac{2}{(\gamma+1)^2}\left(M_w^2 - 1\right)p_0 \tag{4.16}$$

The velocity partial derivative terms are:

$$\frac{\partial u}{\partial p_0} = 0 \qquad \frac{\partial u}{\partial a_0} = -\frac{4}{(\gamma+1)\,M_w} \tag{4.17}$$

$$\frac{\partial u}{\partial u_{0n}} = \frac{-2}{(\gamma+1)}\frac{(M_w^2+1)}{M_w^2} \qquad \frac{\partial u}{\partial \gamma} = \frac{-2}{(\gamma+1)^2}\frac{(M_w^2-1)}{M_w}a_0 \tag{4.18}$$

For a perfect gas, all terms are functions of the Mach number, γ, and the upstream

properties. The differential form of the Area-Mach relation can be expressed in the form:

$$\frac{1}{A}\mathrm{d}A + f\frac{\mathrm{d}U_S}{U_S} + g\frac{\mathrm{d}a_0}{a_0} + h\frac{\mathrm{d}p_0}{p_0} + j\frac{\mathrm{d}u_{0n}}{u_{0n}} + k\frac{\mathrm{d}\gamma}{\gamma} = 0. \tag{4.19}$$

The coefficients are defined as:

$$f(\gamma, M_w) = \frac{M_w}{M_w^2 - 1}\left(1 + 2\mu + \frac{1}{M_w^2}\right)\left(1 + \frac{2}{\gamma+1}\frac{1-\mu^2}{\mu}\right)\frac{U_S}{a_0} \tag{4.20}$$

$$g(\gamma, M_w) = \frac{-4}{\gamma+1}\left(1 + \frac{\mu\left(2\gamma M_w^2 - (\gamma-1)\right)}{2(M_w^2-1)}\right)\left(\frac{(\gamma+1)\,M_w^2}{2\gamma M_w^2 - (\gamma-1)} + \frac{1}{M_w}\right) \tag{4.21}$$

$$h(\gamma, M_w) = \frac{1}{2\left(M_w^2-1\right)}\left[2\left(M_w^2-1\right) + \mu\left(2\gamma M_w^2 - (\gamma-1)\right)\right] \tag{4.22}$$

$$j(\gamma, M_w) = -\frac{M_w}{M_w^2 - 1}\left(1 + 2\mu + \frac{1}{M_w^2}\right)\left(1 + \frac{2}{\gamma+1}\frac{1-\mu^2}{\mu}\right)\frac{u_{0n}}{a_0} \tag{4.23}$$

$$k(\gamma, M_w) = \frac{(\mu-\gamma)}{\gamma\,(\gamma+1)}g(\gamma, M_w) \tag{4.24}$$

where

$$\mu^2 = \frac{(\gamma-1)M_w^2 + 2}{2\gamma M_w^2 - (\gamma-1)}. \tag{4.25}$$

For zero upstream velocity, the relations can be shown to be equivalent to the Area-Mach relation given by Catherasoo & Sturtevant (1983).

4.4 Numerical Method

The extension of the finite-difference method developed in Chapter 2 for the uniform perfect gas case to the more general case of the current chapter is straightforward. The differencing scheme is carried over directly. The main complication is the dependence of the Area-Mach relation on the upstream properties at the current point.

The governing equation, Eqn. 4.6, can be expressed as

$$\nabla \cdot \left[\,\sigma\left(\nabla\alpha + \frac{\mathbf{u}_0}{U_S V_S}\right)\right] = 0, \qquad \sigma \equiv \frac{U_S}{A(U_S, \mathbf{x})}. \tag{4.26}$$

Rewriting in strong conservative form for an arbitrary grid:

$$\frac{\partial}{\partial \xi}\left(\frac{\sigma(U + M_0/U_S V_S)}{J}\right) + \frac{\partial}{\partial \eta}\left(\frac{\sigma(V + N_0/U_S V_S)}{J}\right) = 0, \tag{4.27}$$

where

$$U = a_{11}\alpha_\xi + a_{12}\alpha_\eta, \qquad V = a_{12}\alpha_\xi + a_{22}\alpha_\eta. \tag{4.28}$$

The standard grid parameters a_{11}, a_{12}, a_{22}, and J are defined as in Chapter 2. The total front velocity, V_S, is:

$$V_S = [U\alpha_\xi + V\alpha_\eta]^{-1/2}, \tag{4.29}$$

with the shock normal velocity relative to freestream velocity, U_S, given by subtracting the freestream velocity:

$$U_S = V_S - (M_0\alpha_\xi + N_0\alpha_\eta). \tag{4.30}$$

In the general coordinate system, the components of the upstream velocity are written in terms of the Cartesian components of the velocity $\mathbf{u}_0 = (u_0, v_0)$:

$$M_0 = \xi_x u_0 + \xi_y v_0, \qquad N_0 = \eta_x u_0 + \eta_y v_0. \tag{4.31}$$

The quantities α_ξ and α_η are computed using backward differences in the marching ξ direction and central differences in the crossflow η direction. The $\partial/\partial\xi$ and $\partial/\partial\eta$ terms are differenced as in the original numerical scheme of Chapter 2.

Due to the variation of freestream conditions, the area relation is now a function of both the shock strength, through U_S, and the freestream properties at the current point. In general, the area relation cannot be integrated analytically and must be evaluated numerically. The area relation

$$\frac{1}{A}(\nabla A \cdot \mathbf{n}) + f\left(U_S, \xi, \eta\right)(\nabla U_S \cdot \mathbf{n}) + S\left(U_S, \xi, \eta\right) = 0, \tag{4.32}$$

is rewritten in (ξ, η) coordinates as:

$$\frac{1}{A}(A_\xi U + A_\eta V) + f(U_{S\xi} U + U_{S\eta} V) + S = 0. \tag{4.33}$$

The terms are differenced with the usual combination of backward and central differences, for example at point (i, j):

$$\frac{1}{A}(A_\xi U + A_\eta V) \approx \frac{1}{A_{i,j}} \left(\frac{A_{i,j} - A_{i-1,j}}{\Delta\xi} U_{i,j} + \frac{A^*_{i,j+1} - A^*_{i,j-1}}{2\Delta\eta} V_{i,j} \right). \tag{4.34}$$

Similar differencing is used for the U_S term and the derivatives of freestream properties within the f and S terms. Since $A_{i,j}$ depends implicitly on the current row through $A_{i,j+1}$ and $A_{i,j-1}$, the retarded values of A^* from the previous iteration is used for each iteration. This allows the desired quantity $A_{i,j}$ to be expressed as a function of known quantities.

In problems with strong discontinuities, converging the general area relation often requires an excessive number of iterations at each step. For the perfect-gas relations, a simpler method used by Schwendeman (1988) is adapted for improved performance with only slight loss of accuracy. For zero upstream velocity, the area relation is written solely in terms of the Mach number:

$$\frac{1}{A}\mathrm{d}A + f(\gamma, M)\mathrm{d}M + g(\gamma, M)\frac{\mathrm{d}a_0}{a_0} + h(\gamma, M)\frac{\mathrm{d}p_0}{p_0} + k(\gamma, M)\frac{\mathrm{d}\gamma}{\gamma} = 0. \tag{4.35}$$

Assuming for each step that the functions g, h, k do not change drastically, the equation is integrated using the mean value:

$$\left(\frac{A}{A(0)}\right)\left(\frac{a_0}{a_0(0)}\right)^{\bar{g}}\left(\frac{p_0}{p_0(0)}\right)^{\bar{h}}\left(\frac{\gamma}{\gamma(0)}\right)^{\bar{k}} = \exp\left(-\int_{M_0}^{M} f(\bar{\gamma}, M)\mathrm{d}M\right), \tag{4.36}$$

where $\bar{g}$, $\bar{h}$, and $\bar{k}$ are based on the average M and γ for the previous step. The right side is simply the Area-Mach relation for a perfect-gas for mean $\bar{\gamma}$. For the given point i, j, the simplified formula is dependent only on the Mach number which allows the $\partial A/\partial\alpha$ derivatives needed for convergence to be conveniently expressed without further approximation.

4.5 Shock Propagation Over Inhomogeneities

As an example, shock propagation over cylindrical inhomogeneities in a perfect gas is considered. Both experimental and numerical results are available for comparison. The problem has been investigated numerically using full Euler codes by Quirk and Karni (1994) and a front-tracking shock dynamics code by Schwendeman (1988). The problem was investigated experimentally by Haas and Sturtevant (1987) using weak plane shocks over cylinders containing lighter and heavier gases. The numerical results compare well with experiment. The inability of shock dynamics to produce regular reflection, discussed in regard to the focusing problem of Chapter 2, reappears for the case of a four-shock intersection, and produces features not seen in experiment.

Numerical results for a planar shock propagating over a cylinder containing light gas, with a higher sound speed, are shown in Fig. 4.2. Figure 4.3 shows the Mach number variation as a function of distance along the shock front for the five shock front positions marked in the upper figure with the origin for the distance along the shock front at the centerline. In the experiment, the helium in the cylinder was contaminated; therefore, the sound speed ratio of the gas in the cylinder will be taken as $a_{02}/a_{01} = 2.32$. The radius of the cylinder is $R = 1$, with the initial Mach number of the planar shock wave $M_0 = 1.22$.

Since the sound speed inside the cylinder is higher, the shock within the cylinder accelerates ahead of the shock outside. Initially, regular refraction is observed, and the shock front is kinked at the interface. As the shock propagates forward over the cylinder, the angle between the shock and the interface decreases until irregular refraction occurs. A shock-shock forms moving outward along the shock front, producing a large increase in Mach number as shown in profile B. An additional corner forms on the front outside the cylinder due to a second shock-shock. As the front propagates, the two shock-shocks spread apart producing the visible second corner, seen for example in profile E. The two shock-shocks weaken as they propagate outward from the cylinder. A precursor wave joins the straight shock outside the cylinder with the shock moving ahead in the cylinder. Between the corner and the cylinder, the

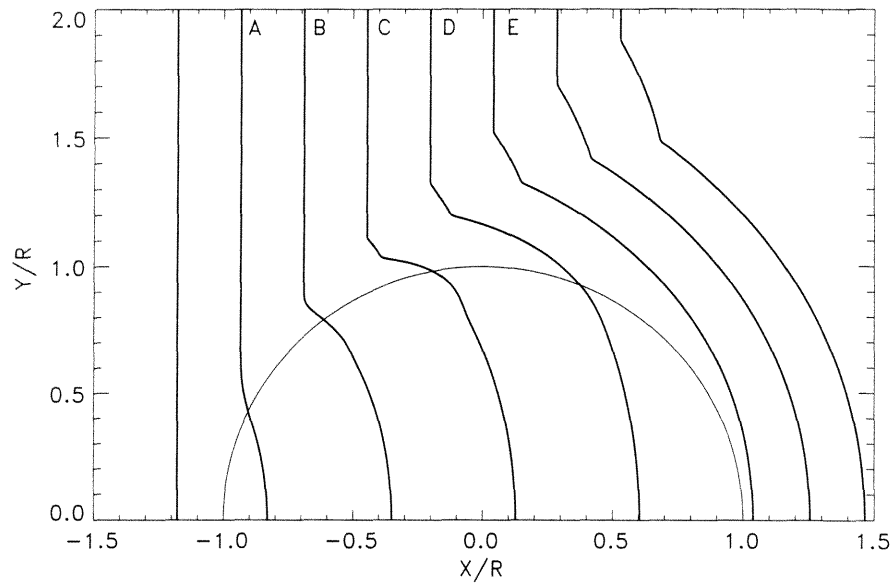

Figure 4.2: Shock dynamics results for plane shock $M_0 = 1.22$ over cylinder with sound speed ratio $a_{02}/a_{01} = 2.32$.

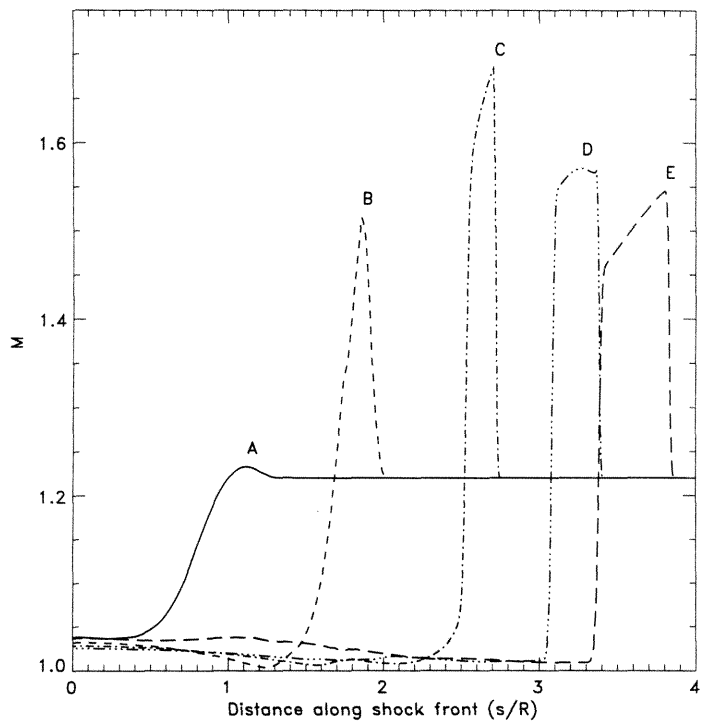

Figure 4.3: Mach number profiles for shock fronts shown in previous figure.

Mach number of the shock approaches unity as the shock diverges. Downstream of the cylinder, the shock emerges diverging.

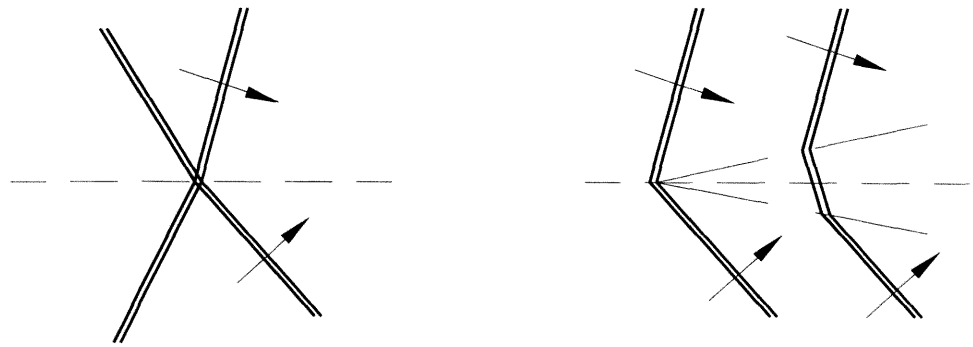

Figure 4.4: Comparison of the (a) four-shock point seen in experiment, and (b) the double corner formed in shock dynamics.

The second shock-shock seen on the shock fronts in Fig. 4.2 is a limitation of shock dynamics. The corner is not seen experimentally or in numerical analysis using the Euler equations (Quirk & Karni 1994). From experiment, a four-shock intersection is expected as shown in Fig. 4.4(a), which turns the shock without a strong increase in Mach number. In shock dynamics, a single shock-shock cannot turn the shock without increasing the Mach number. Therefore after the initial shock-shock discontinuity which turns the shock, a second shock-shock of the opposite family occurs to further turn the front and lower the Mach number. The two shock-shocks are of opposite family and spread apart as the front propagates, as shown in Fig. 4.4(b). This failure of shock dynamics produces the regions of high Mach number seen in Fig. 4.3 in profiles B – E, which are not observed using experimentally. The failure to accurately resolve four-shock intersections is a direct effect of regular reflection not being allowed in shock dynamics.

The shock fronts from the numerical shock dynamics results are compared with experimental results in Fig. 4.5. The solid lines represent the present numerical results, while the dashed lines are the shock fronts digitized from the shadowgraphs in the results of Haas (1984). In the experiment, variation in the shock strength or time origin between shots causes the uneven spacing of the experimental profiles. The

numerical results compare extremely well with experiment. Initially, the numerical shock front appears too highly curved; however, the results agree closely near the back edge of the cylinder. The experimental location of the shock corner appears centered between the two shock-shocks produced by shock dynamics. The Mach number along the shock front would provide a more sensitive comparison to judge the accuracy of the shock dynamics solution, however the information is not available from the experimental and numerical Euler-code results.

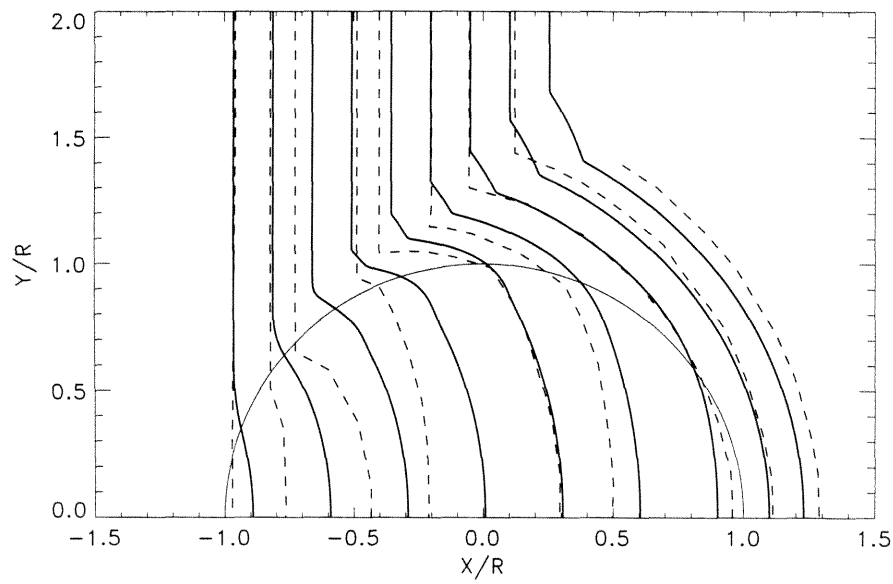

Figure 4.5: Comparison of shock dynamics results with experimental results: plane shock $M_0 = 1.22$ over cylinder with sound speed ratio $a_{02}/a_{01} = 2.32$. Solid lines represent the present numerical results, while the dashed lines are the shock fronts digitized from the shadowgraphs in the results of Haas (1984).

Figure 4.6 displays the numerical results for a planar shock propagating over a cylinder containing heavy gas, with a lower sound speed. Figure 4.7 shows the Mach number variation as a function of distance along the shock front for the five shock front positions marked in the upper figure with the origin for the distance along the shock front at the centerline. In the experiment, the cylinder contained refrigerant R22 with sound speed ratio of the gas in the cylinder to gas outside of $a_{02}/a_{01} = 0.53$. As before, the radius of the cylinder is $R = 1$, and initial shock Mach number $M_0 = 1.22$.

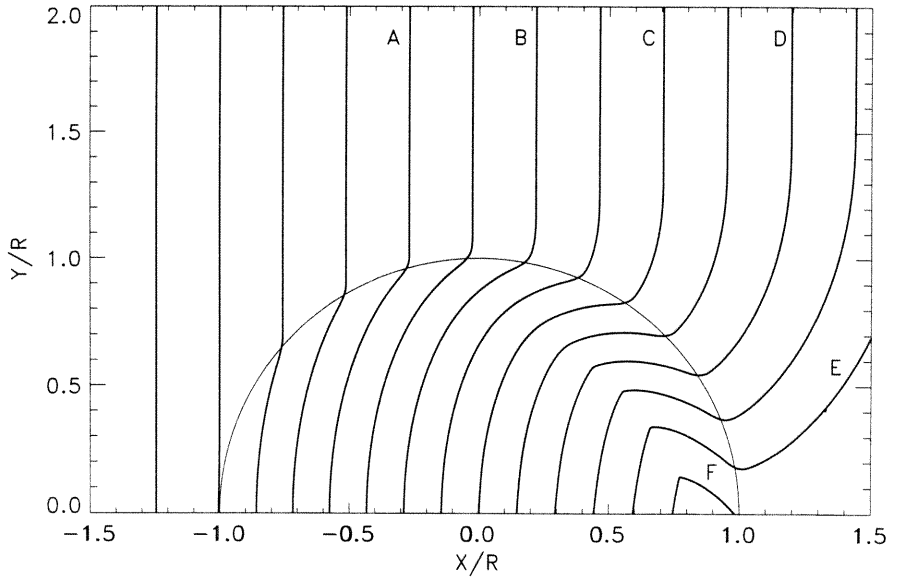

Figure 4.6: Shock dynamics results for plane shock $M_0 = 1.22$ over cylinder with sound speed ratio $a_{02}/a_{01} = 0.53$.

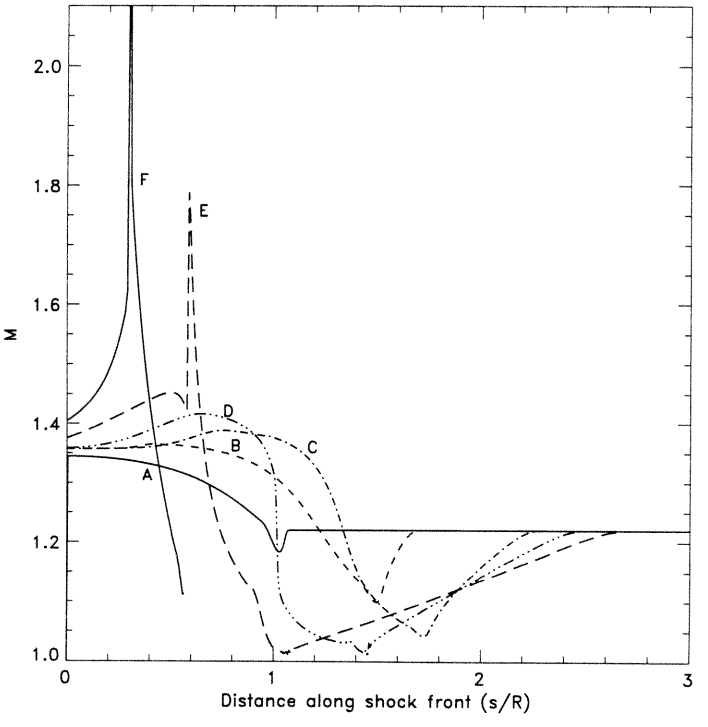

Figure 4.7: Mach number profiles for shock fronts shown in previous figure.

The gas inside the cylinder has lower sound speed, so the shock outside the inhomogeneity advances ahead of the shock front inside, as shown in Fig. 4.6. However, the Mach number inside the cylinder is higher as shown in the Mach number profiles. As the shock advances around the outside of the cylinder, the shock weakens and the Mach number approaches one. The shock front inside forms a corner, approximately along the caustic predicted by acoustics. At the corner, two shock-shocks of opposite families begin to form and move outward between which the Mach number reaches high values. Again, experimental shadowgraphs show four disturbances meeting at the corner. However, since shock dynamics cannot treat regular reflection, a pair of shock-shocks form as in the previous case. The solution cannot be continued past profile F since the shock at the edge of the bubble intersects itself at the centerline.

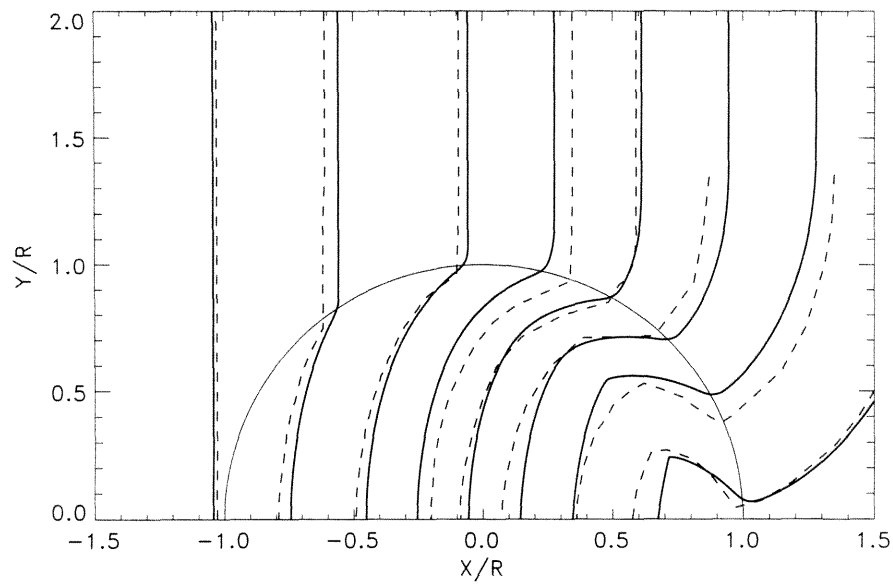

Figure 4.8: Comparison of shock dynamics results with experimental results: plane shock $M_0 = 1.22$ over cylinder with sound speed ratio $a_{02}/a_{01} = 0.53$. Solid lines represent the present numerical results, while the dashed lines are the shock fronts digitized from the shadowgraphs in the results of Haas (1984).

The shock fronts from the numerical shock dynamics results are compared with experimental results in Fig. 4.8. The numerical and experimental shock fronts are plotted at equal times. The fronts digitized from the shadowgraphs in the results

of Haas (1984) are shown as dashed lines, and the thicker solid lines represent the present numerical results. The agreement is good throughout the solution, especially the location of the corner on the shock front inside the cylinder.

Bibliography

Catherasoo, C.J. and Sturtevant, B. (1983) "Shock dynamics in non-uniform media," *J. Fluid Mech.*, **127**, 539–561.

Chisnell, R.F. (1955) "The normal motion of a shock wave through a non-uniform one-dimensional medium," *Proc. R. Soc. Lond.*, **A232**, 350–370.

Chisnell, R.F. (1957) "The motion of a shock wave in a channel, with applications to cylindrical and spherical shock waves," *J. Fluid Mech.*, **2**, 286–298.

Haas, J.-F. (1984) *Interaction of Weak Shock Waves and Discrete Gas Inhomogeneities*, Ph.D. Thesis, Graduate Aeronautical Laboratories, California Institute of Technology, Pasadena, CA.

Haas, J.-F. and Sturtevant, B. (1987) "Interaction of weak shock waves with cylindrical and spherical gas inhomogeneities," *J. Fluid Mech.*, **181**, 41–76.

Quirk, J. and Karni, S. (1994) "On the dynamics of a shock-bubble interaction," *NASA CR-194978, ICASE Report No. 94-75.*

Schwendeman, D.W. (1988) "Numerical shock propagation in non-uniform media," *J. Fluid Mech.*, **188**, 383–410.

Whitham, G.B. (1957) "A new approach to problems of shock dynamics, Part I: Two-dimensional problems," *J. Fluid Mech.*, **2**, 145–171.

Whitham, G.B. (1959) "A new approach to problems of shock dynamics, Part II: Three-dimensional problems." *J. Fluid Mech.*, **5**, 369–386.

Whitham, G.B. (1968) "A note on shock dynamics relative to a moving frame," *J. Fluid Mech.*, **31**, 449–453.

Appendix A Area-Mach Relation for Shock Waves in Water

A.1 Shock Relations

For a stationary shock, the conservation of mass, momentum, and energy gives the three equations

$$\rho_1 u_1 = \rho_2 u_2, \tag{A.1}$$

$$p_1 + \rho_1 u_1^2 = p_2 + \rho_2 u_2^2, \tag{A.2}$$

$$h_1 + \frac{1}{2}u_1^2 = h_2 + \frac{1}{2}u_2^2, \tag{A.3}$$

for the pressure p, enthalpy h, density ρ, and velocity u. The subscripts 1 and 2 denote conditions upstream and downstream of the shock respectively. The Mach number of the shock is given by $M = u_1/a_1$. Combining Eqns. A.1 – A.3, the enthalpy difference is often expressed in terms of the pressure and density as

$$h_2 - h_1 = \frac{1}{2}\left(p_2 - p_1\right)\left(v_1 + v_2\right), \tag{A.4}$$

where $v = 1/\rho$. Assuming the upstream conditions are specified, Eqns. A.1 – A.3 provide three equations for the four unknown downstream values p_2, ρ_2, u_2, and h_2. The set of equations is closed by an equation of state, typically $h = h(p, \rho)$.

A.2 NBS Equation for Water Properties

In order to make predictions for the temperature and entropy changes across the shock and to verify the accuracy of the Tait equation for water, the NBS equation of state for water is used. The U.S. National Bureau of Standards (Haar *et al.*, 1984)

developed a formulation for the properties of water and steam based on a review of experimental thermodynamic measurements. An analytic equation containing over sixty coefficients approximates the Helmholtz function $A(\rho, T)$ as a function of density and temperature. The remaining thermodynamic variables are then calculated by differentiation of this relation.

The equations are specifically recommended for the range

$$273.15 \leq T \leq 1273.15 \text{ K}, \tag{A.5}$$

where for $T \geq 423.15$ K, the maximum pressure is

$$p_{max} = 1500 \text{ MPa} \quad (15000 \text{ bar}), \tag{A.6}$$

and for $273.15 \leq T \leq 423.15$ K, the maximum pressure is

$$p_{max} = 100 \left[5 + \frac{(T - 273.15 \text{ K})}{15 \text{ K}} \right] \text{ bar}. \tag{A.7}$$

In addition, a small region near the critical point is excluded. The inaccuracy in density across the entire temperature range as a function of pressure and temperature is estimated to be less than 35 parts in 10000 for $p \leq 100$ MPa (1000 bar) and less than 150 parts in 10000 for pressures up to 1000 MPa (10000 bar).[1]

With the analytic equation of state, the shock equations are closed, and the system can be written in terms of the density ratio, and solved by iteration. The resulting shock properties are shown in Fig. A.1 for the initial pressure of $p_1 = 1$ bar and temperature of $T_1 = 20$ C.

[1]The authors claim the equation should also be suitable for the wider range

$$260 \leq T \leq 2500K, \tag{A.8}$$

$$0 \leq p \leq 3000 \text{ MPa} \quad (30000 \text{ bar}). \tag{A.9}$$

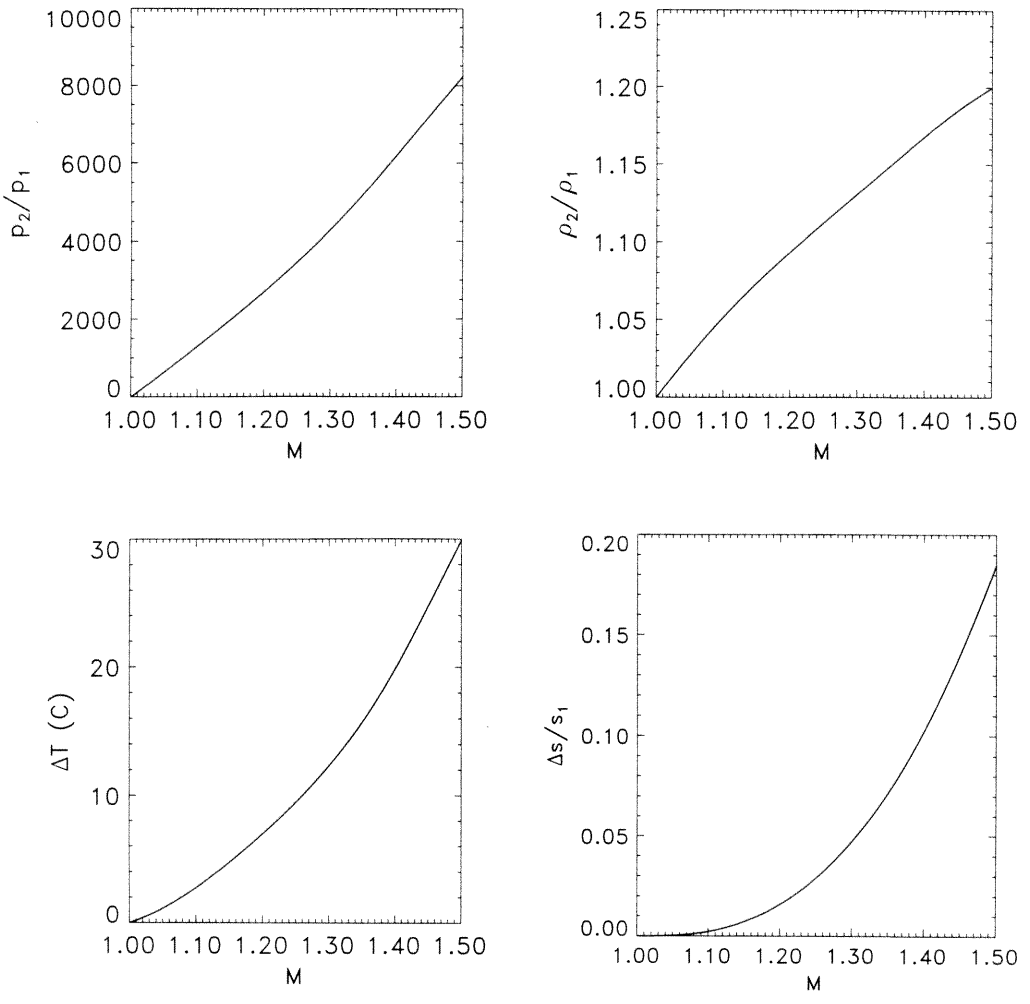

Figure A.1: Shock properties from NBS equation of state for upstream conditions $p_1 = 1$ bar, $T_1 = 20$ C.

A.3 Tait Equation for Water

Kirkwood and Bethe (1942) proposed the modified Tait equation for water:

$$\frac{1}{\rho}\left(\frac{\partial \rho}{\partial p}\right)_s = \frac{1}{\Gamma\,(p+B)}. \tag{A.10}$$

Integrating from a reference state:

$$\frac{p(\rho,s)+B(s)}{p(\rho_0,s)+B(s)} = \left(\frac{\rho(p,s)}{\rho(p_0,s)}\right)^{\Gamma}. \tag{A.11}$$

Taking the reference state as zero pressure $p_0 = 0$ and rearranging yields the more familiar form

$$p(\rho, s) = B(s) \left[\left(\frac{\rho(p, s)}{\rho(0, s)} \right)^{\Gamma} - 1 \right], \tag{A.12}$$

where $B(s)$ is a weak function of entropy, $\rho(0, s)$ is the density at zero pressure, and Γ is approximately constant.

Since the coefficients are only functions of entropy, the sound speed is given without further approximation by

$$a^2 = \left(\frac{\partial p}{\partial \rho} \right)_s = \frac{\Gamma \left(p + B(s) \right)}{\rho}. \tag{A.13}$$

The value of B should be chosen to give agreement with the sound speed at the reference state. The sound speed varies with entropy. The relation does not imply that B is a constant or that the Tait equation is an isentropic relation.

The terms $B(s)$ and $\rho(0, s)$ are only weak functions of entropy, therefore $B(s)$ and $\rho(0, s) = \rho_0$ are typically taken as constant without significant loss of accuracy:

$$p(\rho) = B \left[\left(\frac{\rho(p, T)}{\rho_0} \right)^{\Gamma} - 1 \right]. \tag{A.14}$$

This further approximation leads to the relation

$$\frac{p + B}{\rho^{\Gamma}} = \text{constant}, \tag{A.15}$$

which is similar in form to the isentropic condition for gases. However, since it is not an isentropic relation, it can be applied across shock waves.

The appropriate choice of Γ depends on the pressure and temperature range of interest. Γ decreases with pressure at constant temperature and increases with temperature at constant pressure. For temperature $T_1 = 20$ C, the value of $\Gamma = 7.15$ is most often used in the literature. The density at zero pressure for $T_1 = 20$ C sets $\rho_0 = 998.232$ kg/m^3, and B follows from Γ and the sound speed (Eqn. A.13), $B = 303.975$ MPa.

With the assumption that B, Γ, and $\rho(0, s)$ are constant, the equation for pressure p is only a function of the density ρ. Therefore, the shock Hugoniot p_2 versus v_2 follows immediately. The resulting Hugoniot is shown in Fig. A.2 compared to the Hugoniot from the full equation of state for initial temperature of 20 C.

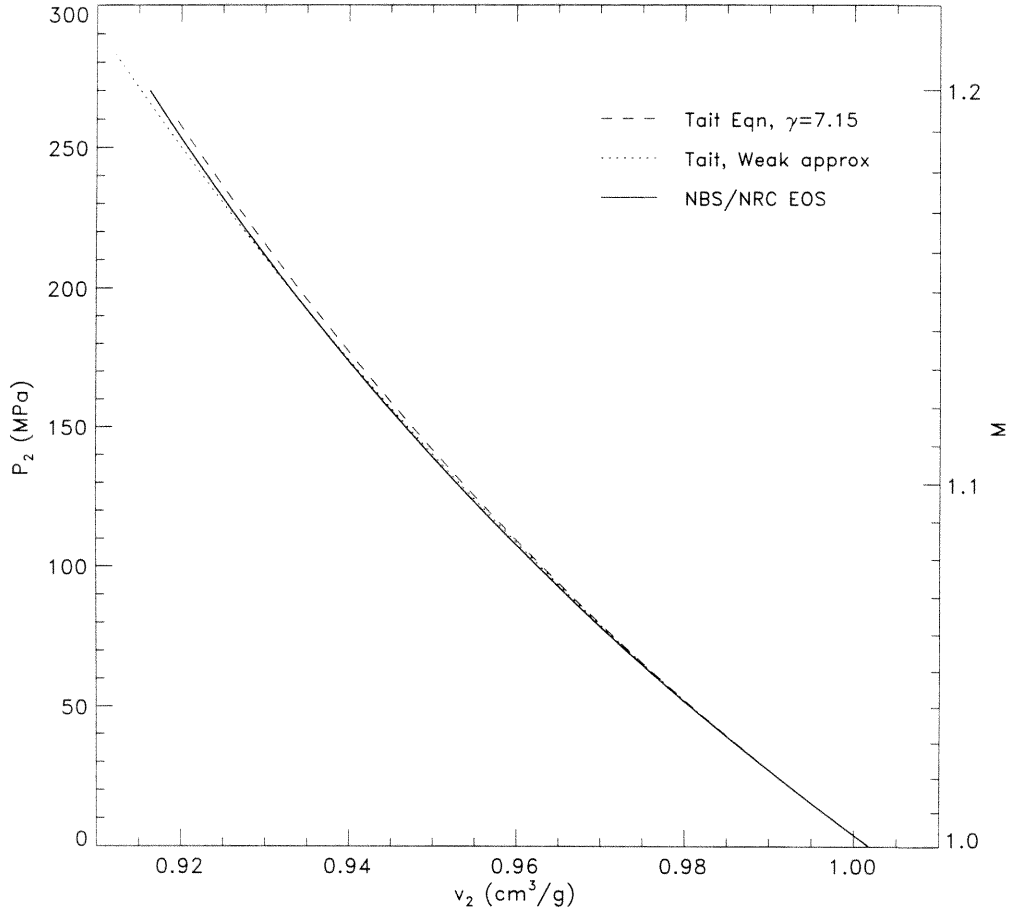

Figure A.2: Comparison of shock Hugoniot for NBS equation of state and modified Tait equation for $p_1 = 1$ bar, $T_1 = 20$ C.

A.4 Shock Relations Using Tait Equation

Using the Tait equation, which gives $p(\rho)$ in Eqn. A.14, the system of shock equations can be solved without reference to the energy equation. Eliminating the density ratio,

the pressure ratio is given as a function of the shock Mach number by the non-trivial root of

$$Z^{(\Gamma+1)/\Gamma} - \left(1 + \Gamma M^2\right) Z^{1/\Gamma} + \Gamma M^2 = 0, \tag{A.16}$$

where the ratio of the shifted pressures $Z = (p_2 + B)/(p_1 + B)$. The density ratio R follows immediately from Eqn. A.15:

$$R \equiv \frac{\rho_2}{\rho_1} = Z^{1/\Gamma}. \tag{A.17}$$

Therefore, the density ratio can also be written as the non-trivial root of the equation

$$R^{\Gamma+1} - \left(1 + \Gamma M^2\right) R + \Gamma M^2 = 0. \tag{A.18}$$

The density ratio and shifted pressure ratio are functions of Γ alone. The value of B is required only to calculate the value of the pressure ratio p_2/p_1, and the value of ρ_0 does not appear in any of the relations. However, the assumed equation of state does not allow a prediction of the temperature or entropy change across the shock.

Two limits are recognized. In the weak shock limit $M \to 1$, the pressure and density ratios reduce to

$$Z(M \to 1) = 1 + \frac{4\Gamma}{(\Gamma + 1)} (M - 1), \tag{A.19}$$

$$R(M \to 1) = 1 + \frac{4}{(\Gamma + 1)} (M - 1). \tag{A.20}$$

In the strong shock limit as $M \to \infty$, the pressure and density ratio are approximated by

$$Z(M \to \infty) \sim M^2, \tag{A.21}$$

$$R(M \to \infty) \sim \left(M^2\right)^{1/\Gamma}. \tag{A.22}$$

Unlike for a perfect gas, with the assumed equation of state the density ratio does not approach a finite value as the shock Mach number approaches infinity.

A.5 Enthalpy Change

A further approximation for the enthalpy change has been used in the literature (Holl 1982, Best 1991), which results in a system equivalent to that for a perfect gas. As will be shown, the approximation is unnecessary and may result in unexpectedly large errors in Mach number predictions.

From thermodynamics, the enthalpy derivative $\mathrm{d}h$ can be written in terms of the entropy derivative $\mathrm{d}s$ and the pressure derivative $\mathrm{d}p$:

$$\mathrm{d}h = T\mathrm{d}s + v\mathrm{d}p. \tag{A.23}$$

This expression can be integrated from state 1 to 2 along a path consisting of a constant pressure segment and constant entropy segment to give

$$h_2 - h_1 = \int_{p_1}^{p_2} v\mathrm{d}p \,\Big|_{s=s_1} + \int_{s_1}^{s_2} T\mathrm{d}s \,\Big|_{p=p_2}. \tag{A.24}$$

If the modified Tait equation is assumed, the first integral can be evaluated explicitly:

$$h_2 - h_1 = \frac{\Gamma}{\Gamma - 1}\left(\frac{p_2 + B}{\rho_2} - \frac{p_1 + B}{\rho_1}\right) + \int_{s_1}^{s_2} T\mathrm{d}s. \tag{A.25}$$

For weak shocks, one might suggest that the entropy contribution to the enthalpy difference can be neglected, the term being small compared to the total enthalpy difference. If the term is neglected, the enthalpy relation becomes

$$h_2 - h_1 \approx \frac{\Gamma}{\Gamma - 1}\left(\frac{p_2 + B}{\rho_2} - \frac{p_1 + B}{\rho_1}\right). \tag{A.26}$$

This approximation provides the enthalpy $h = h(p, \rho)$ which closes the original system Eqns. A.1 – A.3. The resulting system of equations is identical to the system for a perfect gas, the only difference being the pressures are replaced by the shifted pressures $p + B$. The shock relations for a perfect gas should carry over directly with the ratio of specific heats γ replaced by Γ.

There are problems with this approach. The system is now overspecified since five equations (Eqns. A.1–A.3, A.14, and A.26) are now available for the four unknown quantities p_2, ρ_2, u_2, and h_2. This point is not troublesome, since the choice of which four equations to solve yields results which only vary by several percent over the range of low Mach numbers. However, the error in the Mach number corresponding to a given pressure ratio is much larger than might be naively expected. In fact, denoting the neglected integral term by Δh_s, the correct expression for the Mach number as a function of the shifted pressure ratio is

$$M^2\left(1+\frac{1}{2}\left(\Gamma-1\right)\left(1+\frac{\rho_1}{\rho_2}\right)\frac{\Delta h_s}{h_2-h_1}\right)=\frac{\left(\Gamma+1\right)Z+\left(\Gamma-1\right)}{2\Gamma}. \tag{A.27}$$

The right-hand side is indeed the form of the perfect gas relation; however, the correct condition to neglect the Δh_s term is clearly

$$\frac{1}{2}\left(\Gamma-1\right)\left(1+\frac{\rho_1}{\rho_2}\right)\frac{\Delta h_s}{h_2-h_1}\ll 1. \tag{A.28}$$

Since $\Gamma = 7.15$ and ρ_1/ρ_2 is generally near unity, the error involved in neglecting the term is some $6\times$ larger than the mere ratio of the neglected term to the total enthalpy difference. Since at $p_2 = 10$ kbars, Δh_s is approximately three percent of the total enthalpy difference, this assumption can lead to a 15 – 20 percent error in the shock Mach number.

The above approximation does show that for weak shocks the system behaves essentially as a perfect gas with high γ value. However, the loss of accuracy is unnecessary since a similar conclusion can be drawn from the weak shock approximation. The correct approach is to use the full equation for the pressure ratio, Eqn. A.16, or density ratio, Eqn. A.18.

A.6 Area-Mach Relation

With the shock jump conditions from the modified Tait equation, the Area-Mach relation in shock dynamics for water can be derived. Recall for geometrical shock

dynamics, the shock relations are applied along the $C+$ characteristic:

$$\frac{\mathrm{d}p}{\mathrm{d}x} + \rho a \frac{\mathrm{d}u}{\mathrm{d}x} + \frac{\rho a^2 u}{u+a} \frac{1}{A} \frac{\mathrm{d}A}{\mathrm{d}x} = 0. \tag{A.29}$$

The derivatives of pressure can be expressed in terms of the density ratio using the definition of sound speed

$$\frac{\mathrm{d}p}{\mathrm{d}x} = a^2 \frac{\mathrm{d}\rho}{\mathrm{d}x}. \tag{A.30}$$

From the continuity equation, the velocity is written in terms of the Mach number and density ratio as

$$u_2 = a_1 M \left(1 - 1/R\right), \tag{A.31}$$

which gives the derivative

$$\frac{\mathrm{d}u}{\mathrm{d}x} = \frac{R-1}{R} \frac{\mathrm{d}M}{\mathrm{d}x} + \frac{M}{R^2} \frac{\mathrm{d}R}{\mathrm{d}x}. \tag{A.32}$$

The derivative of the density ratio is given by differentiating Eqn. A.18 and simplifying:

$$\frac{\mathrm{d}R}{\mathrm{d}x} = \left(\frac{2MR\left(R-1\right)}{R^{\Gamma+1} - M^2} \right) \frac{\mathrm{d}M}{\mathrm{d}x}. \tag{A.33}$$

Substituting into the characteristic equation, Eqn. A.29, and simplifying yields the Area-Mach relation:

$$A(M,\Gamma) = \exp\left[\int_{M_0}^{M} \frac{1}{M} \left(\frac{R^{(\Gamma+1)/2} + M}{R^{(\Gamma+1)/2} - M} \right) \left(1 + \frac{M(R-1)}{R^{(\Gamma+1)/2}} \right) \mathrm{dM} \right]. \tag{A.34}$$

A comparison of the Area-Mach relation for water using the modified Tait equation $\Gamma = 7.15$ and the perfect gas relation, $\gamma = 1.4$, is shown in Fig. A.3. The reference Mach number for the $A(M)$ relation is chosen as the midpoint of the Mach number range; therefore, the values are forced to coincide at the midpoint. Of the coefficients in the modified Tait equation, only the value of Γ appears in the Area-Mach relation. For problems such as shock focusing, the trajectory of the triple point and the location of maximum pressure predicted by geometrical shock dynamics will be independent

of the choice of B. However in converting Mach number results to pressure values, the value of B will be required.

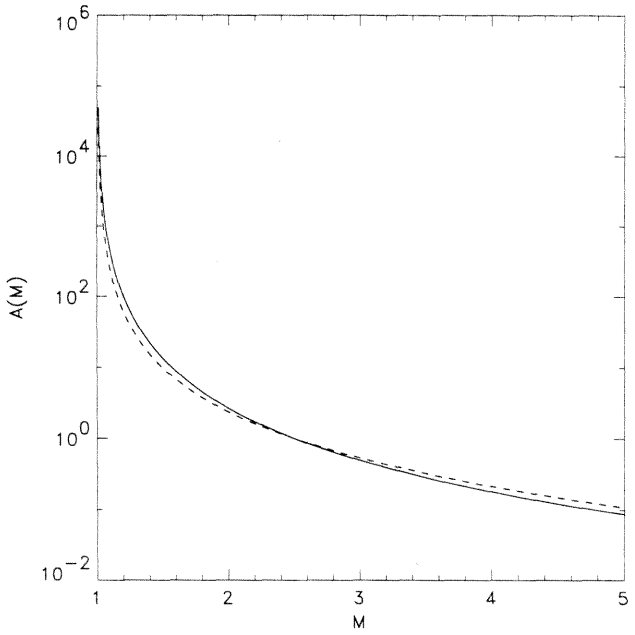

Figure A.3: Comparison of the Area-Mach relation $A(M)$ for water using the modified Tait equation $\Gamma = 7.15$ and perfect gas relation, $\gamma = 1.4$.

Bibliography

Best, J. (1991) "A generalisation of the theory of geometrical shock dynamics," *Shock Waves*, **1**, 251–273.

Cole, R. (1948) *Underwater Explosions*, Princeton Univ. Press, Princeton.

Haar, L., Gallagher, J., and Kell, G. (1984) *NBS/NRC steam tables: thermodynamic and transport properties and computer programs for vapor and liquid states of water in SI units*, Hemisphere Pub. Corp., Washington.

Holl, R. (1982) *Wellenfokussierung in Fluiden*, Dissertation, Aachen.

Kirkwood, J. and Bethe, H. (1942) "Progress report on the pressure wave produced by an underwater explosion," *OSRD Report 588.*

Appendix B Seismic Detection of Sonic Booms

The seismic network in Southern California routinely detects sonic booms from aircraft. The high density of sites and the extensive ground coverage of the network, over 50,000 square kilometers, provide a unique opportunity to study the long-range propagation of direct and indirect sonic booms.

In Section B.1, the fundamental features of sonic boom carpets under a realistic atmosphere are presented. The pressure signals from the N-wave signal in the atmosphere produce a small, but detectable, ground motion as outlined in Section B.2. Seismic data from three overflights are presented in Section B.3: a west to east SR-71 pass at $M = 3.15$, the landing of space shuttle Discovery, STS-42, at Edwards AFB, and the passage of shuttle Discovery over Washington and Oregon. Section B.4 presents the results of an analysis of a set of "mystery booms" which occurred in California in 1992 and 1993.

B.1 Atmospheric Propagation

For the propagation of sonic booms through the atmosphere, the linear theory of geometrical acoustics is applied. In geometrical acoustics, the shock front moves along rays with speed c relative to the surrounding medium, where c is the local sound speed. Following Pierce (1981), the raytracing equations can be written

$$\frac{\mathrm{d}\mathbf{x}}{\mathrm{d}t} = \frac{c^2\mathbf{s}}{\Omega} + \mathbf{v}, \tag{B.1}$$

$$\frac{\mathrm{d}\mathbf{s}}{\mathrm{d}t} = -\frac{\Omega}{c}\nabla c - \mathbf{s}\times(\nabla\times\mathbf{v}) - (\mathbf{s}\cdot\nabla)\mathbf{v}, \tag{B.2}$$

where $\mathbf{n}$ is the unit normal to the wave, the medium moves with velocity $\mathbf{v}$, the wave-slowness vector $\mathbf{s} = \mathbf{n}/(c + \mathbf{v} \cdot \mathbf{n})$, and $\Omega = 1 - \mathbf{v} \cdot \mathbf{s} = c/(c + \mathbf{v} \cdot \mathbf{n})$. A stratified model is typically assumed for the atmosphere where properties vary only with altitude [$\mathbf{v} = \mathbf{v}(z)$, $c = c(z)$], and the vertical wind velocity is zero ($v_z = 0$). For this case, the equation for the change of $\mathbf{s}$ simplifies to a generalization of Snell's law. The horizontal components s_x and s_y must remain constant, while the vertical component is given by

$$s_z = \pm \left[\left(\frac{\Omega}{c} \right)^2 - s_x^2 - s_y^2 \right]^{1/2}. \tag{B.3}$$

The ray equations become

$$\frac{\mathrm{d}x}{\mathrm{d}t} = \frac{c^2 s_x}{\Omega} + v_x, \qquad \frac{\mathrm{d}y}{\mathrm{d}t} = \frac{c^2 s_y}{\Omega} + v_y, \qquad \frac{\mathrm{d}z}{\mathrm{d}t} = \frac{c^2 s_z}{\Omega}. \tag{B.4}$$

From the assumption of a stratified atmosphere, the right-hand side of Eqns. B.4 are functions of altitude alone, and can be integrated numerically from atmosphere profiles.

Rays are confined to regions of sound speed and wind speed where $s_z^2 > 0$. A turning point exists where s_z passes through zero and the ray changes direction of vertical propagation. For an atmosphere without winds, a ray will only turn horizontal at the altitude with sound speed

$$c(z^*) = \frac{c_0}{\cos \theta_0}, \tag{B.5}$$

where c_0 and θ_0 are the sound speed and ray angle to the horizontal at the point where the ray is emitted. For the case of a sonic boom, the ray is emitted at the complement of the Mach angle. Therefore, the ray turning points for an aircraft in straight and level flight are located at the altitude where the sound speed is equal to the velocity of the aircraft. For an aircraft flying at below the ambient sound speed at the ground, all rays will be turned and none will reach the ground, this critical Mach number being referred to as the cutoff Mach number. Rays which are turned at high altitude will only reach the ground if the sound speed is greater than that at

the ground, otherwise the ray will be channeled between an upper and lower turning point.

For long-range propagation in the atmosphere, the effect of winds cannot be neglected. For a stratified atmosphere with winds, the turning points for each ray depends on the ray direction. It is convenient to define the effective sound speed seen by a ray moving in a particular direction $c_{eff} = c_0 + \mathbf{v} \cdot \mathbf{n}$. The turning point for a ray occurs at the altitude where

$$c_{eff}(z^*) = \frac{c_0}{\cos\theta_0}, \tag{B.6}$$

which depends on the ray direction through the effective sound speed.

For the present analysis, the Range Reference Atmosphere for Edwards Air Force Base is used for wind and thermodynamic properties to 70 km altitude (Meteorology Group, Range Commanders Council 1983). These profiles are comparable to the U.S. Standard Atmosphere, Supplemental Atmosphere (1966) and climatic data for the Pacific Missile Range, California (de Violini 1967, 1969). In Fig. B.1, profiles of temperature and zonal and meridional wind components are shown as a function of altitude from the monthly profiles for January and November. Zonal winds are positive when from west to east and meridional wind components are positive when from south to north. During the winter months the zonal wind component shows strong stratospheric winds blowing from west to east. Meridional wind components are much weaker and tend to fluctuate in direction, although stronger meridional wind components are also found at stratospheric altitudes.

Effective sound speeds for five ray directions are shown in Fig. B.1. Shallow rays traveling east will be turned downward toward the ground between 40 km and 60 km altitude. The effective sound speed for rays traveling directly north or south is not sufficiently high at altitude to diffract the rays to the surface, but a significant area of high effective sound speeds exists even for the northeast and southeast directions. Rays traveling west will not be turned back to the ground at any altitude. The temperature rise in the stratosphere alone is not sufficient to return rays to the ground.

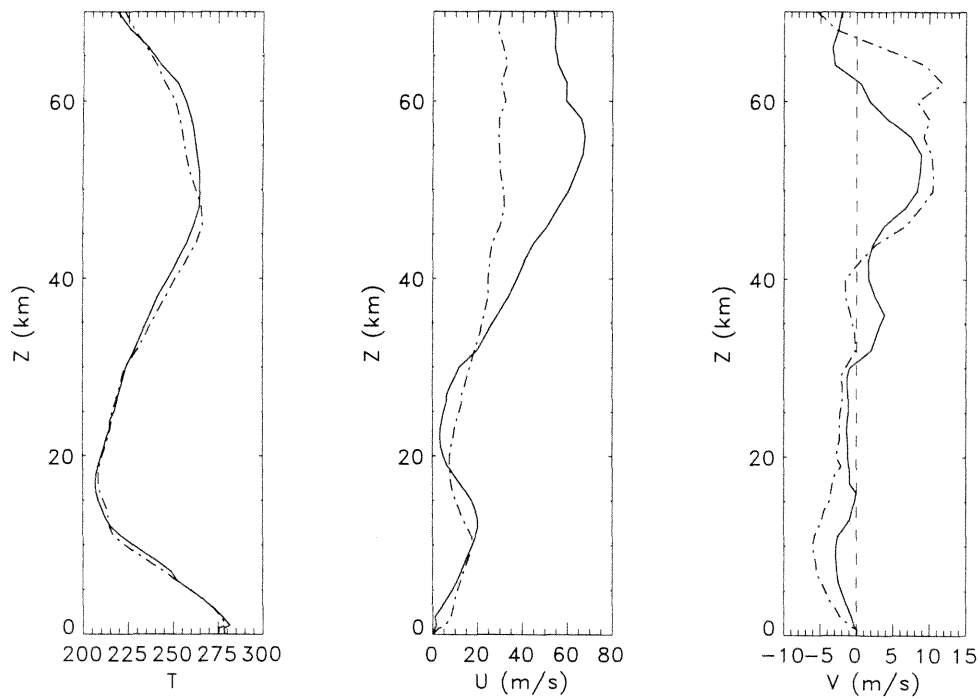

Figure B.1: Temperature and zonal (east/west, U) and meridional (north/south, V) wind component profiles for January (——) and November (-·-), Edwards AFB Range Reference Atmosphere.

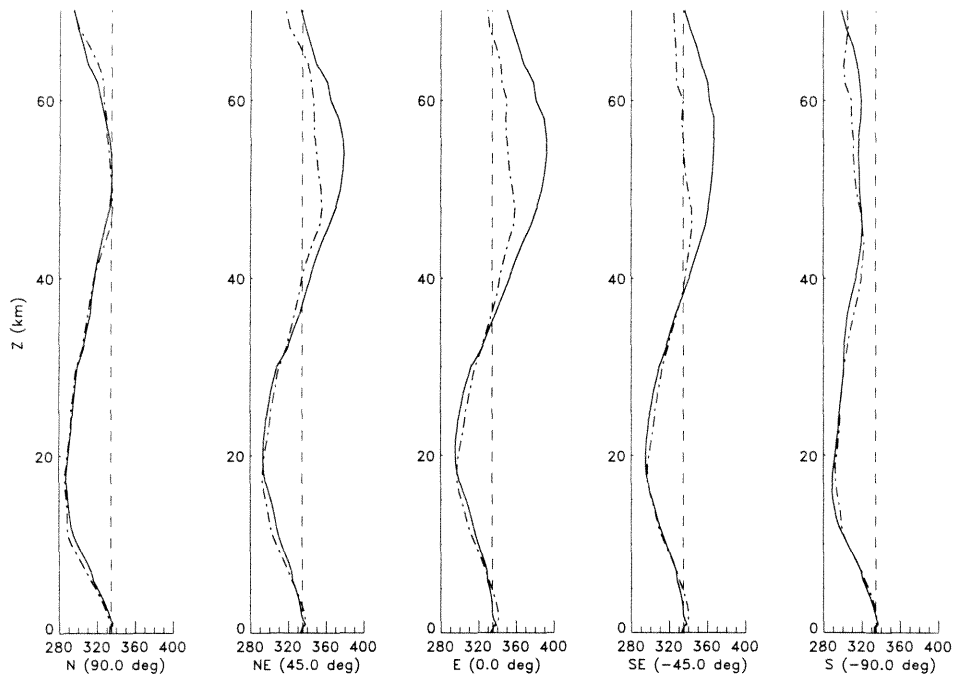

Figure B.2: Effective sound speed profiles for January (——) and November (-·-), Edwards AFB Range Reference Atmosphere.

For a uniform atmosphere with no winds, the sonic boom forms a Mach cone which intersects the ground to produce the hyperbolae typically associated with the sonic boom footprint. For realistic atmosphere profiles, the sonic boom footprint becomes much more complex as shown in Fig. B.3. The primary carpet lies directly beneath the aircraft and consists of direct rays from the aircraft to the ground. The increasing temperature as rays approach the ground leads to the refraction of the rays upward which limits the width of the primary carpet. Outside of the primary carpet, a secondary carpet is formed of indirect rays which have propagated upward and been refracted back to the ground. Additional carpets are formed further from the aircraft flight path by rays which have reflected from the ground, returned to high altitude, and then back toward the ground. Even higher order carpets exist further out from the flight path.

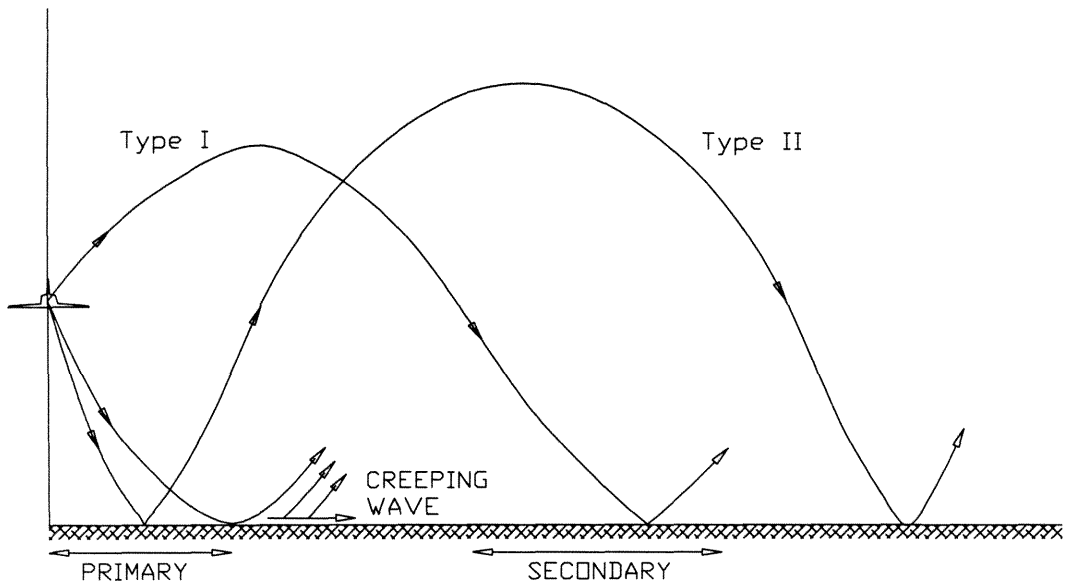

Figure B.3: Illustration of sonic boom carpets.

Between the primary carpet and secondary carpet, geometrical acoustics predicts a shadow region where no rays reach the ground. However, the full theory of acoustics allows for a creeping wave launched at the edge of the primary carpet which propagates along the ground in the ray direction. The creeping wave is typically illustrated as a wave moving along the ground continually launching rays upward. Since the creeping wave sheds energy, the amplitude dies off exponentially

with distance (Rickley & Pierce 1980).

Examples of these atmospheric effects have been observed experimentally for sonic booms. Rickley and Pierce (1980) measured secondary sonic booms from Concorde flights along the East coast of the United States. Microphones captured similar indirect sonic booms from the Concorde refracted from the level of the stratosphere (40 – 50 km) which had propagated a horizontal range of over 165 km. These were followed several minutes later by low-frequency signals which had refracted from the level of the thermosphere (100 – 130 km) and propagated over ranges up to 1000 km (Balachandran *et al.*, 1977). Sonic boom signatures are often recorded past the nominal edge of the primary carpet; however, the occurrence of creeping waves is difficult to detect due to the similar effects of turbulent scattering (Onyeowu 1975).

Although pointwise pressure measurements have been made for indirect sonic booms, fundamental questions about the size and shape of the indirect carpets and the shadow regions remain unanswered. Measurement of indirect sonic booms has traditionally been very difficult due to the locational dependence on the atmospheric conditions at high-altitude and the wide geographic coverage required to resolve the carpets. As shown in the next section, existing seismic networks, such as the network in Southern California which covers over 50,000 square kilometers, provide a very useful tool for analyzing the indirect sonic booms.

B.2 Seismic Detection

Early use of seismographs in sonic boom research was primarily restricted to examining the effects of sonic booms on ground motion and the possibility of damage to structures or triggering of earthquakes (Cook & Goforth 1970). These studies involved only a few seismograph instruments, often specifically emplaced for the overflights. Only recently have larger existing seismograph networks been used to detect sonic booms from aircraft and meteors (Kanamori *et al.*, 1992, Qamar 1993).

Due to the much higher sound speed in the surface, the majority of the energy of the N-wave is reflected; however, several effects of the wave are observed in the

ground. The primary effect of the pressure wave is the moving strain field in the surface immediately beneath the N-wave. A secondary, weaker effect is the production of coupled Rayleigh waves which follow the passage of the N-wave. In addition, irregularities in the ground properties and acoustic coupling with geographical features become local sources which radiate additional seismic waves. Since the wave speed is higher in the ground, precursor waves are often observed to arrive several seconds before the sonic boom (Cook *et al.*, 1972).

If the shock wave is approximated as a moving normal load over an elastic halfspace, the displacement and velocity of the surface can be computed from a superposition of solutions producing zero normal and shear stress at the boundary. Consider an incident wave moving along the surface at velocity U with pressure distribution

$$p(x,t) = p_0 e^{i\omega(t-x/U)}. \tag{B.7}$$

The vertical displacement u_z at the surface is given by:

$$u_z(x,t) = -\frac{U p_0}{2\mu\omega}\left(\frac{\lambda+2\mu}{\lambda+\mu}\right) e^{i\omega(t-x/U)}, \tag{B.8}$$

where λ and μ are the elastic constants of the halfspace (Ben Menachem & Singh 1981) The surface velocity follows immediately by derivation of the displacement. The theoretical surface displacement and velocity predicted by Eqns. B.7 and B.8 for a pressure N-wave with duration $\tau = 0.2$ is shown in Fig. B.4. The surface velocity diagram shows the inverted U-type of signature characteristic of an N-wave for velocity seismograms, the two strong downward peaks corresponding to the leading and trailing shock on the original N-wave.

Pressure transducers have been added to a number of the TERRAscope stations in Southern California operated by the Caltech Seismological Laboratory. This allows direct comparisons between sonic boom pressures and surface velocity. In Fig. B.5, data are shown for the two TERRAscope stations CAL (CalState LA) and RPV (Rancho Palos Verdes) for the reentry of space shuttle Endeavour on March 18, 1995.

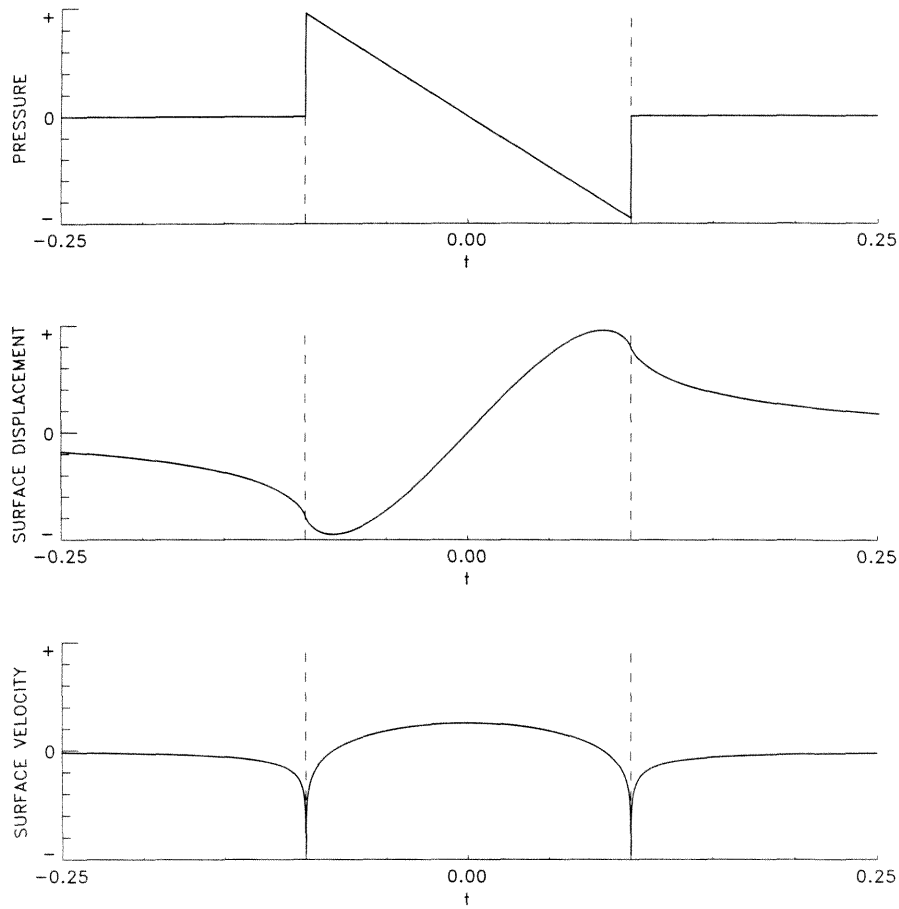

Figure B.4: Surface effects of pressure wave.

(Data provided by Dr. H. Kanamori, Caltech Seismological Laboratory.) The pressure and surface velocity are measured directly and corrected only for instrument response, and the surface displacement is integrated from the velocity. The characteristic double-peaked signature of an N-wave is clearly visible in the surface velocity traces which provides an accurate estimate of the N-wave duration. The features of the N-wave are also very well captured in the surface displacement.

The seismic network used in the current study consists of over 200 stations shown in Fig. B.6 from TERRAscope (Caltech's broadband seismic network), the Caltech-U.S.G.S. Southern California Seismic Network (SCSN), and the University of California Los Angeles Basin Seismic Network. The majority of sites are SCSN stations which measure ground motion velocity in the frequency range of 1 to 20 Hz. These

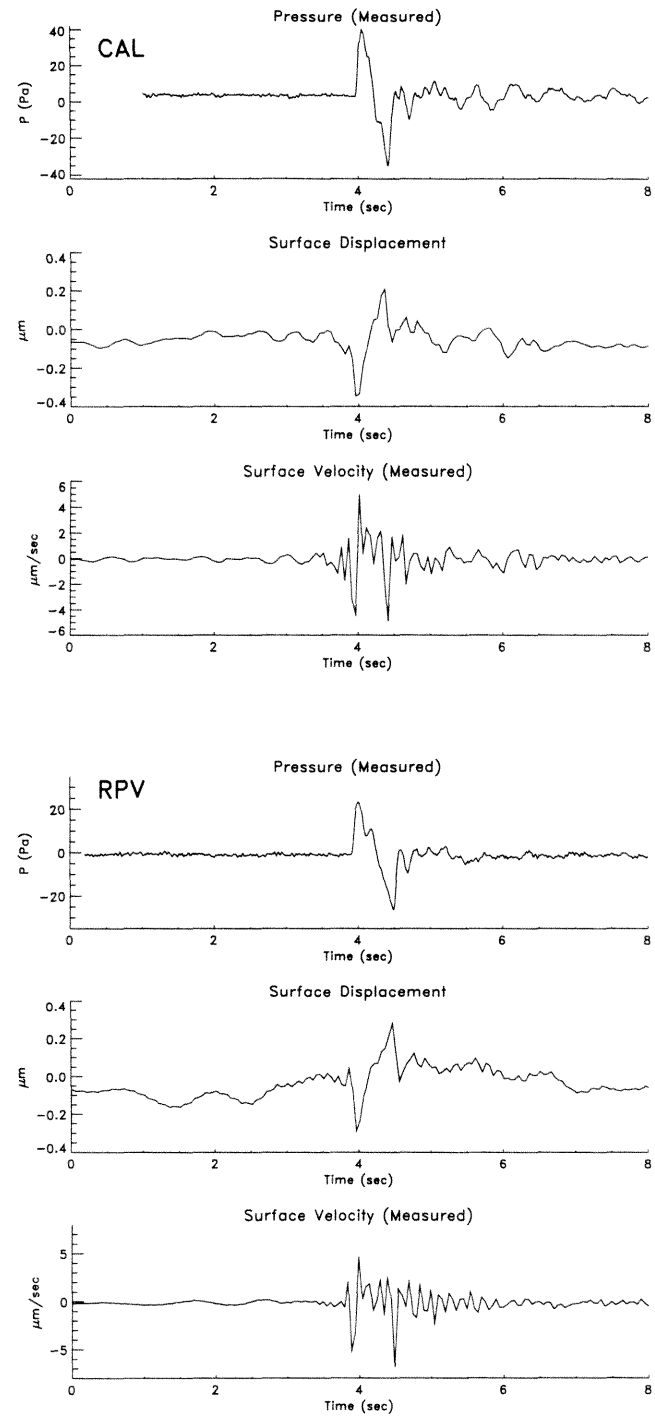

Figure B.5: Pressure, surface displacement, and surface velocity for TERRAscope sites CAL (Cal State LA) and RPV (Rancho Palos Verdes) for the reentry of space shuttle Endeavour, March 1995. (Data provided by Dr. H. Kanamori, Caltech Seismological Laboratory.)

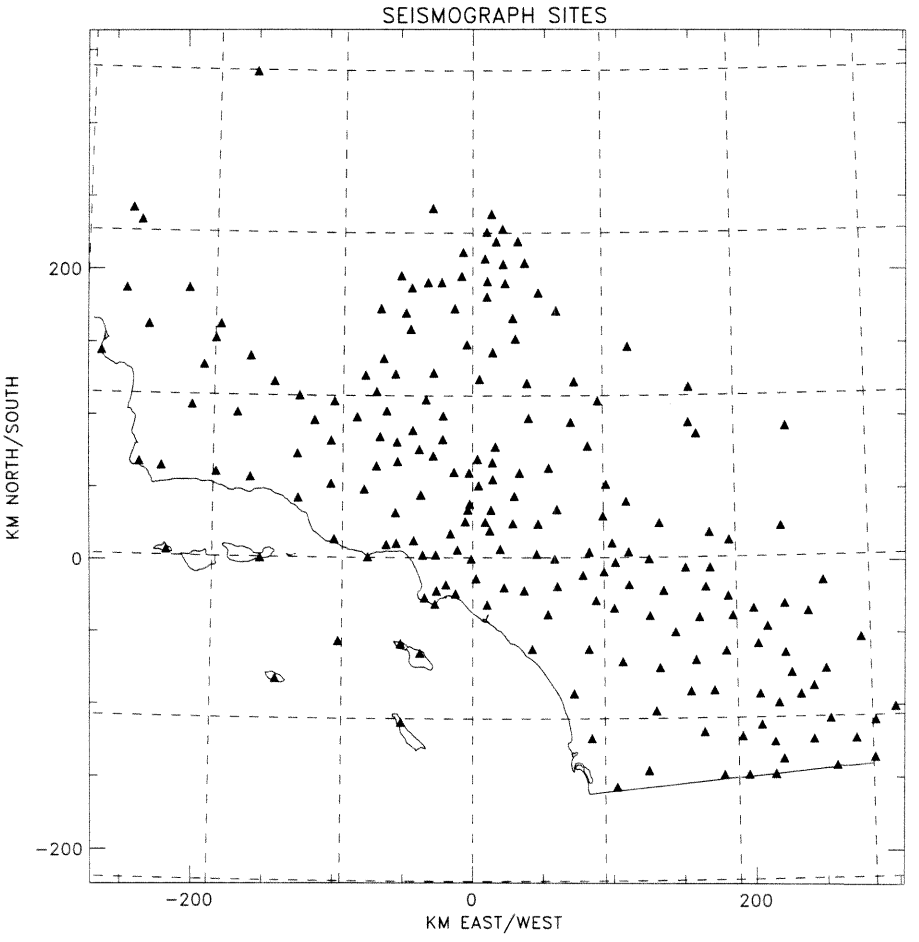

Figure B.6: Seismic stations in California used for the current study.

instruments record frequencies well within this range, but response falls off above 20 Hz due to an anti-aliasing filter near 30 Hz. Only a limited response is available below 1 Hz. Raw output voltage data were provided at 100 samples per second by Dr. H. Kanamori, Caltech Seismological Laboratory and Dr. J. Mori, U.S.G.S., Pasadena. For magnitude analysis, the data was corrected for instrument response; otherwise the raw signal data were used for selecting arrival times.

For the entire network, amplitude information is difficult to extract from the seismic data due to the lack of detailed knowledge of the local surface conditions of the seismic stations. When the site and instrument properties are known, seismic data have been shown to produce accurate estimates of N-wave pressures for the primary sonic booms from shuttle landings (Kanamori *et al.*, 1992). However, for the

extensive network used in this study, the sites are typically only classified as hard or soft rock sites. A useful approximation for at least a basic comparison of pressures is available from Goforth and McDonald (1968). In flight tests with a wide variety of aircraft using velocity seismographs with a frequency range of 1 to 100 Hz, the peak ground velocity was found to be proportional to the maximum overpressure: for high-density rock, maximum ground velocity was approximately 1.5 μm/sec per Pascal of overpressure, and approximately 2 μm/sec per Pascal for low-density rock.

The seismograph records provide accurate information for arrival time of the pressure disturbances. When the signal characteristic of N-waves is visible, the duration of the N-wave can also be determined. However, at soft-rock sites, the actual N-wave signal itself is often lost in reverberations of the local sediment. Due to the extremely low magnitude of the ground motion, disturbances often are indistinguishable from local sources such as noise or nearby traffic. Events which are not also observed on nearby sites have to be ignored as local noise when choosing arrival times from the time traces.

B.3 Flight Results

B.3.1 SR-71 Mach 3.15 Overflight

First due to the relative complexity of the space shuttle reentry trajectories, the results from a portion of an NASA SR-71 flight on December 9, 1993 are presented. As part of a pre-scheduled flight, the SR-71 flew a high-speed pass from east to west over Edwards AFB at $M = 3.15$ at an altitude of 21 km. Through the kind cooperation of Dr. Robert Meyer of NASA Dryden, the SR-71 trajectory was modified to facilitate collection of seismic data.

The seismic data from the overflight are shown in Fig. B.7. All seismic stations available are denoted by the triangle symbols, and solid symbols denote the sites which detected the sonic boom. The arrival time data were converted to a regular grid and contoured to produce the solid arrival time contours. Since the majority of

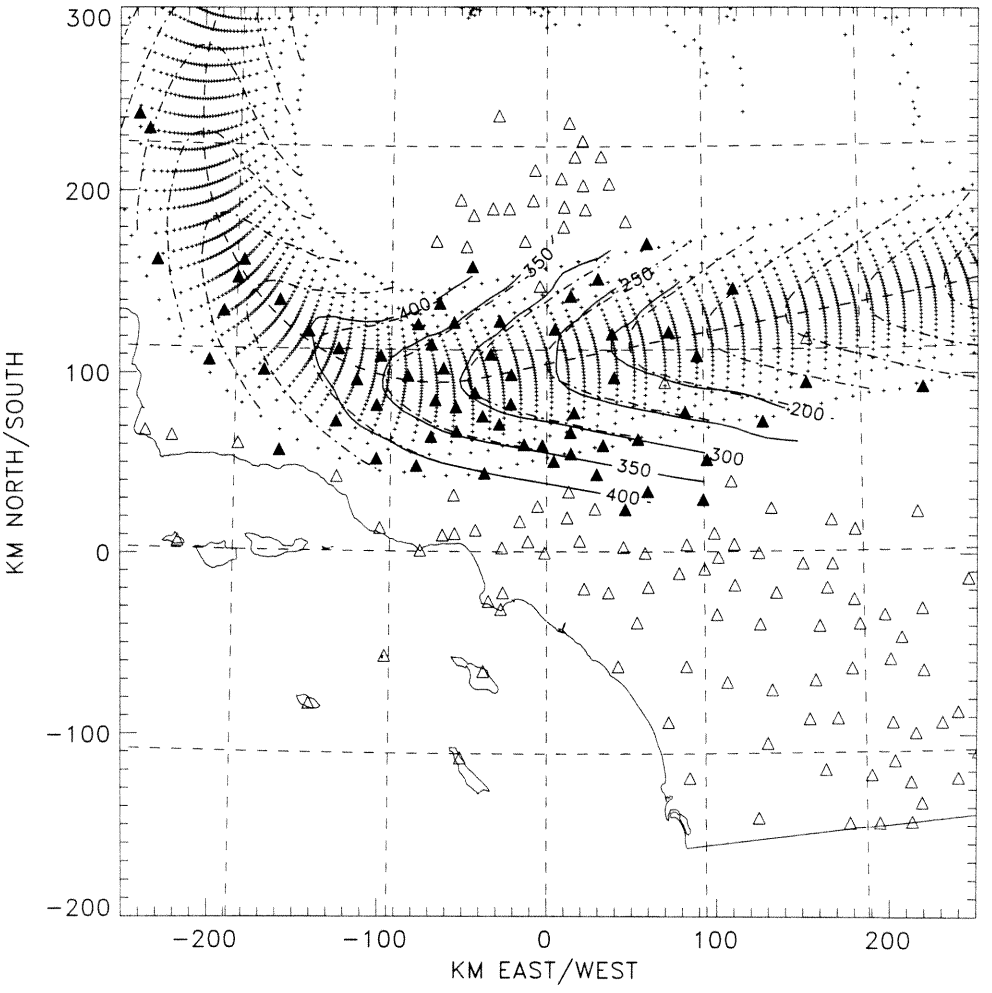

Figure B.7: Contours from seismic arrival times (——) compared with raytracing results (–·–) for SR-71 flight, December 8, 1993, at $M = 3.15$, altitude 21 km. The small plus symbols represent where rays from raytracing intersected the ground.

the rays are propagating east to west, no indirect carpets are observed. The seismic data clearly show both the north and south edges of the primary carpet.

For comparison, a raytracing computation was performed. A cone of rays was launched at the Mach angle at discrete times along the trajectory, and the rays were then propagated using the wind and temperature profiles from the Edwards AFB Range Reference Atmosphere (Meteorology Group, Range Commanders Council 1983). The small plus symbols in Fig. B.7 represent the locations where the computed rays intersected the ground. The majority of the ray ground intersections are direct rays

in the primary carpet underneath the aircraft trajectory, only a few indirect rays appear north of the primary carpet. The ground arrival time contours from raytracing are shown as dashed lines. The raytracing contours compare well with the arrival times from the seismic data, with the only significant disagreement being a loss of resolution due to the lack of sites as the aircraft begins to turn north.

Sections of the seismic traces for seven sites from the SR-71 flight are shown in Fig. B.8. The time traces show the ground velocity signal characteristic of an N-wave. The MAR site is shown as an example of a site where the signal is lost in reverberations in the ground layers. Precursor waves are seen before several of the N-wave signatures, most notably at the SBK site. This example provides an important verification that the seismic data do not show spurious signals, but only the signal from the N-wave.

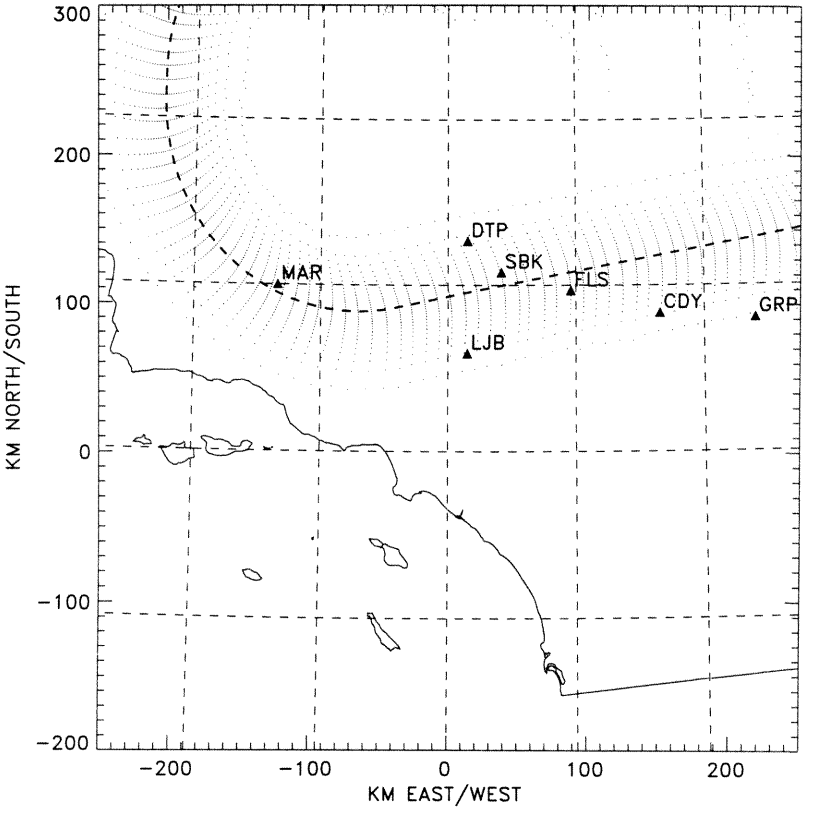

(a) See following figure for caption.

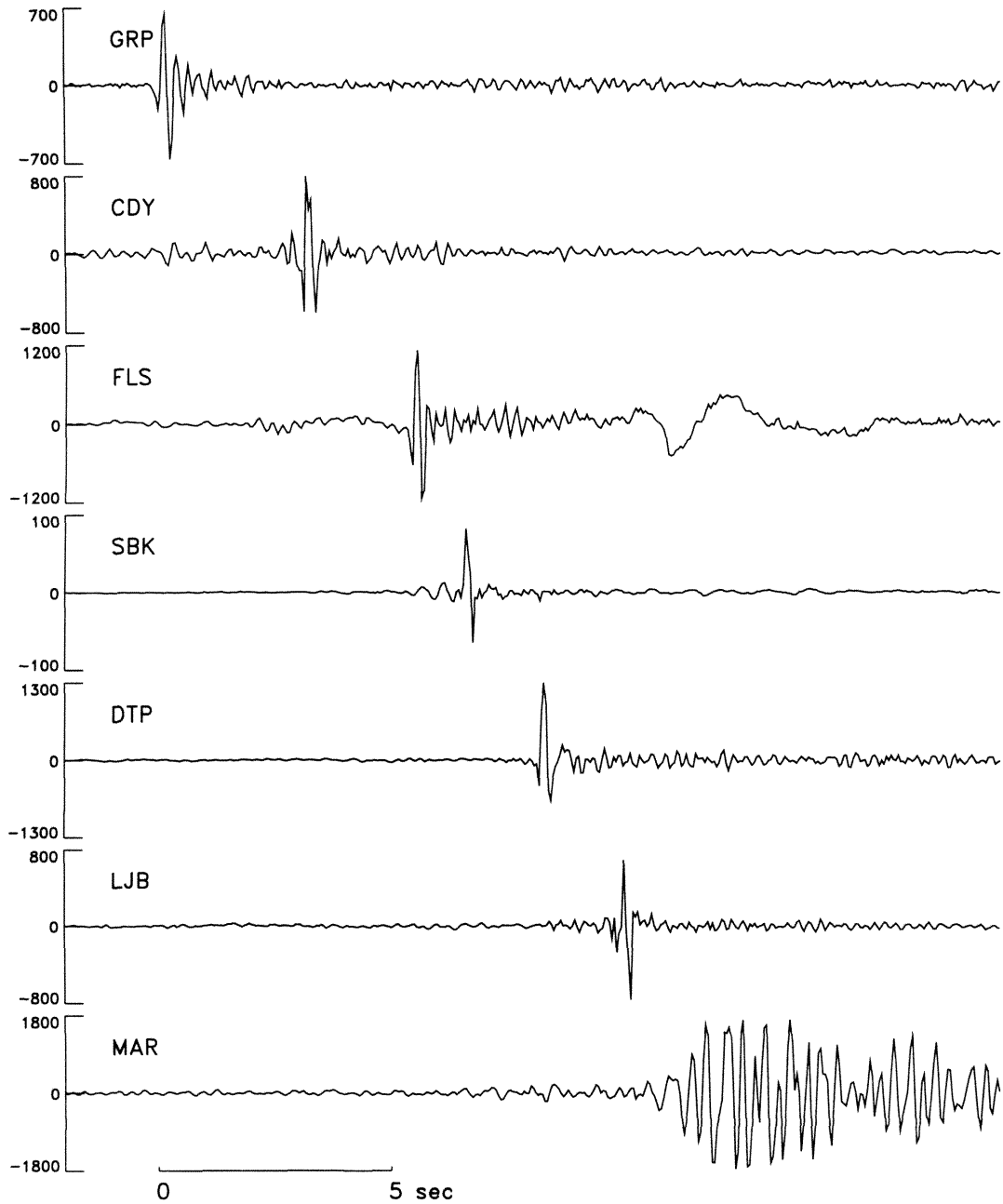

Figure B.8: (a) Seismic station locations relative to SR-71 trajectory and (b) time traces from selected seismic stations which detected the primary boom. Time traces record ground motion, vertical scale is voltage output in counts.

B.3.2 STS-42 Reentry

The seismic data were examined in detail for the landings at Edwards AFB of space shuttle Discovery, STS-42, on January 30, 1992. The flight approached Edwards AFB from the west over the Pacific Ocean, leading to rays which propagated predominantly from west to east producing a complex set of indirect sonic boom carpets.

Contours of arrival time from raytracing results for the reentry of STS-42 are shown in Fig. B.9. A cone of rays was launched at the Mach angle at discrete times along the trajectory, and the rays were then propagated through the wind and temperature profiles. The small plus symbols represent the locations where computed rays intersected the ground. The shuttle trajectory is shown as a dashed line. Within the primary carpet the arrival time contours shown as dashed lines have the characteristic hyperbolic shape, modified by the maneuvering of the shuttle. The shockfront predicted by raytracing is crossed and folded within the primary carpet, as denoted by the curve of ground intersection points for rays emitted at subsequent times cross. As the altitude and Mach number decrease, the width of the primary carpet decreases. In addition to the primary carpet, two indirect carpets to the east are apparent, separated by shadow regions where no rays reach the ground from raytracing.

The seismic network detected four booms from the STS-42 landing. Arrival time contours from the seismic data for the four booms are shown in Fig. B.10. Arrival times are chosen from the time traces, converted to a regular grid, and contoured at 50 second intervals. The most immediately striking feature of the seismic results is the complete ground coverage. Virtually the entire network detected at least one boom, and no shadow region is visible, in contrast to the raytracing results (Fig. B.9). Within the primary carpet, the contours agree very well with the raytracing results, verifying again the ability of the seismic network to accurately map the primary carpet.

Due to the rather unexpected amount of ground coverage of the sonic booms, three sets of representative time traces are shown in Figs. B.11 – B.13. The first figure, Fig. B.11, shows seven seismic sites situated in the shadow region predicted

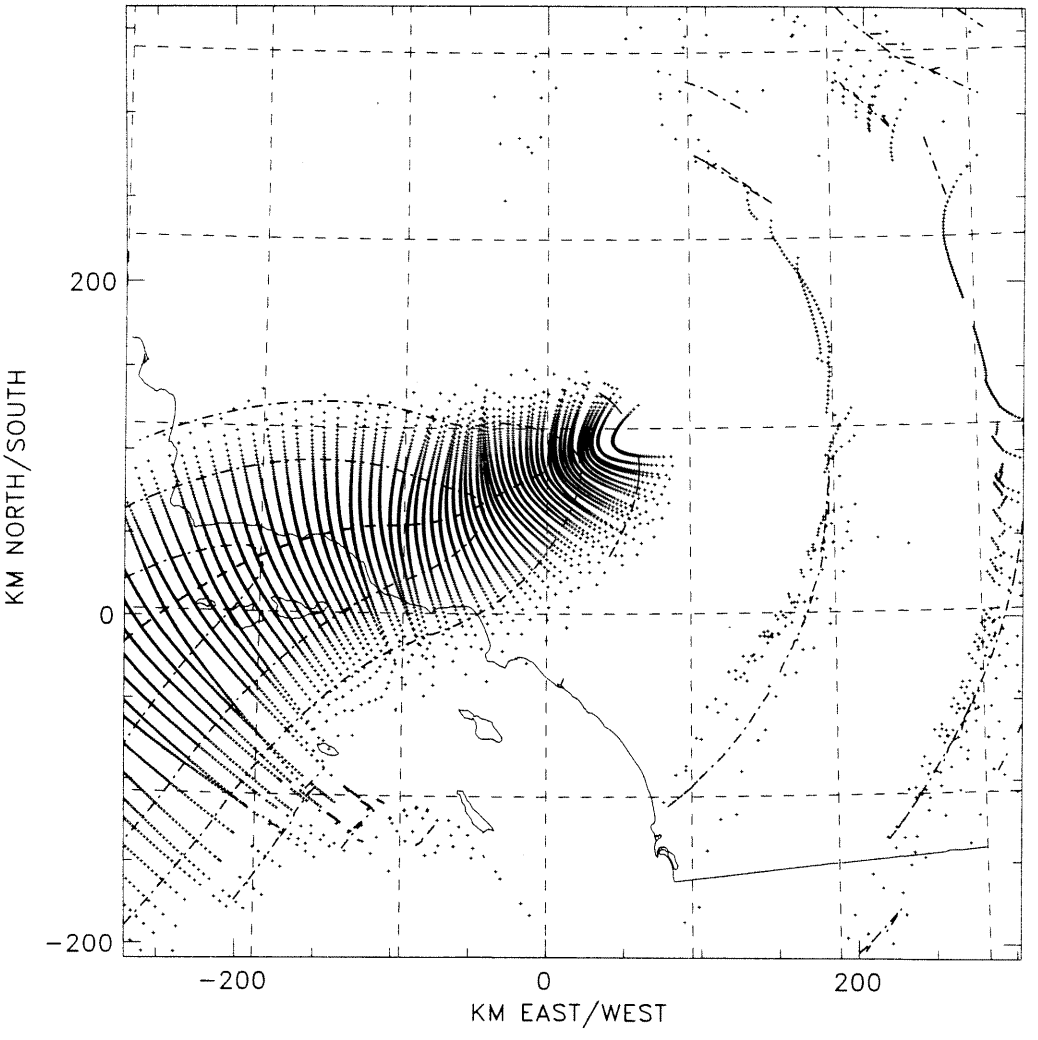

Figure B.9: Raytracing results for STS-42 reentry showing points where rays intersected the ground (+) and contours of arrival times (−·−).

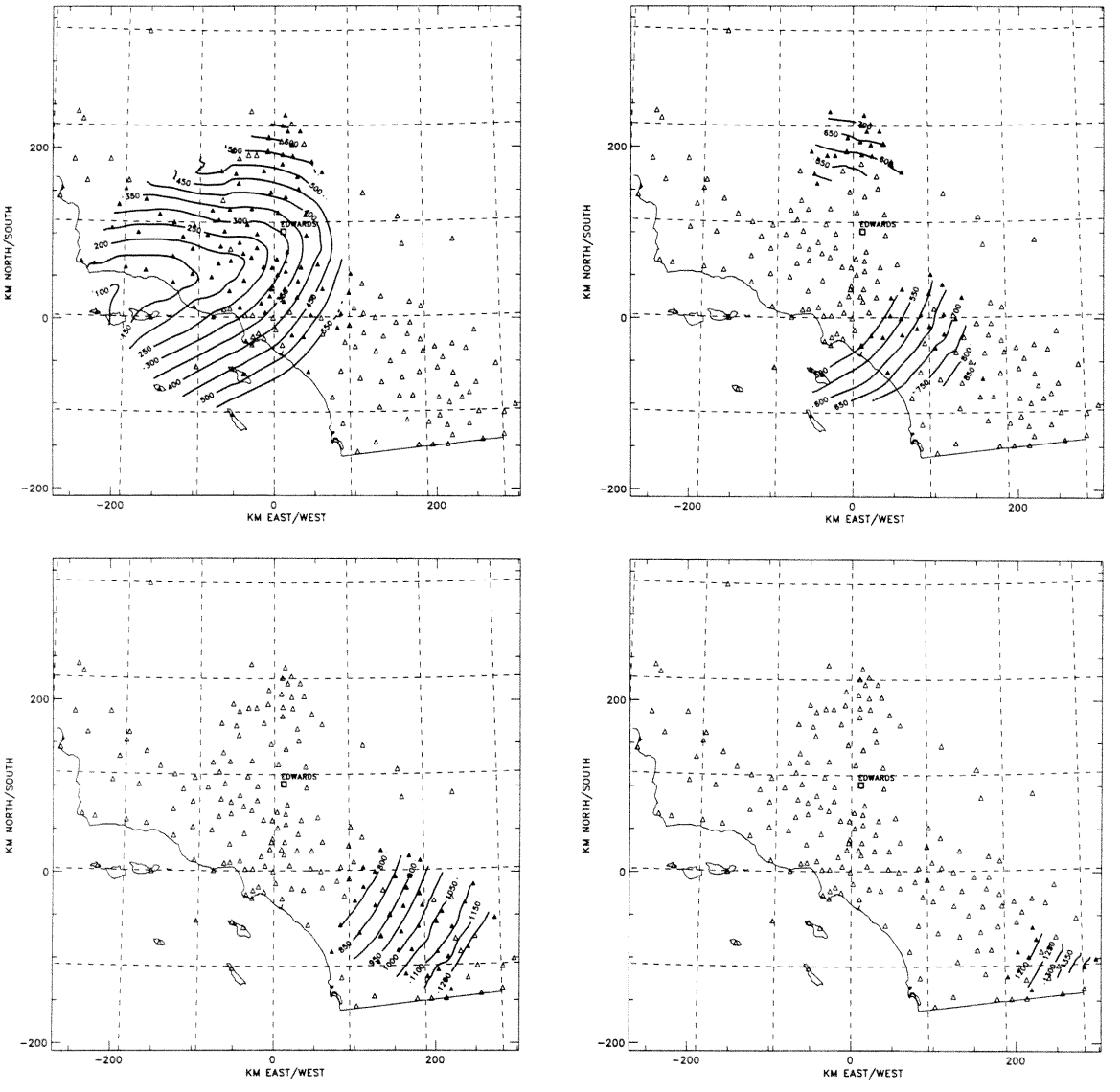

Figure B.10: Contours from seismic arrival times, STS-42 reentry.

by geometrical acoustics. The sites, both north and south of the trajectory, show two booms within the shadow region. The first boom is almost certainly the primary boom, labeled Boom 1. This is consistent with the underprediction of the carpet width by raytracing as was observed for the SR-71 overflight. The second boom, labeled Boom 2, may be a creeping wave, although the magnitude appears too large. Attempts to vary the atmosphere profile, such as introducing unusually strong jet stream winds, failed to duplicate the second boom in this region by raytracing.

The second figure, Fig. B.12, shows seven sites in an area roughly 100 km square, slightly inside the secondary carpet predicted by raytracing. Boom 2 appears on each of the sites, but splits into two peaks on the eastern sites, for example at the MDA and RAY sites. The low amplitude disturbance seen on these sites appears to be a third and fourth disturbance, labeled Boom 3 and Boom 4, which strengthens and becomes clearly visible further east. The final set of time traces for STS-42 reentry, Fig. B.13, shows a line of seven sites stretching 150 km, offering a rare opportunity to view the development of the indirect carpets. The second boom, Boom 2, is seen to disappear further from the flight track to be replaced by Boom 3 and Boom 4. The indirect booms are split into two segments, which one would assume is caused by discrete bands in the atmosphere profiles.

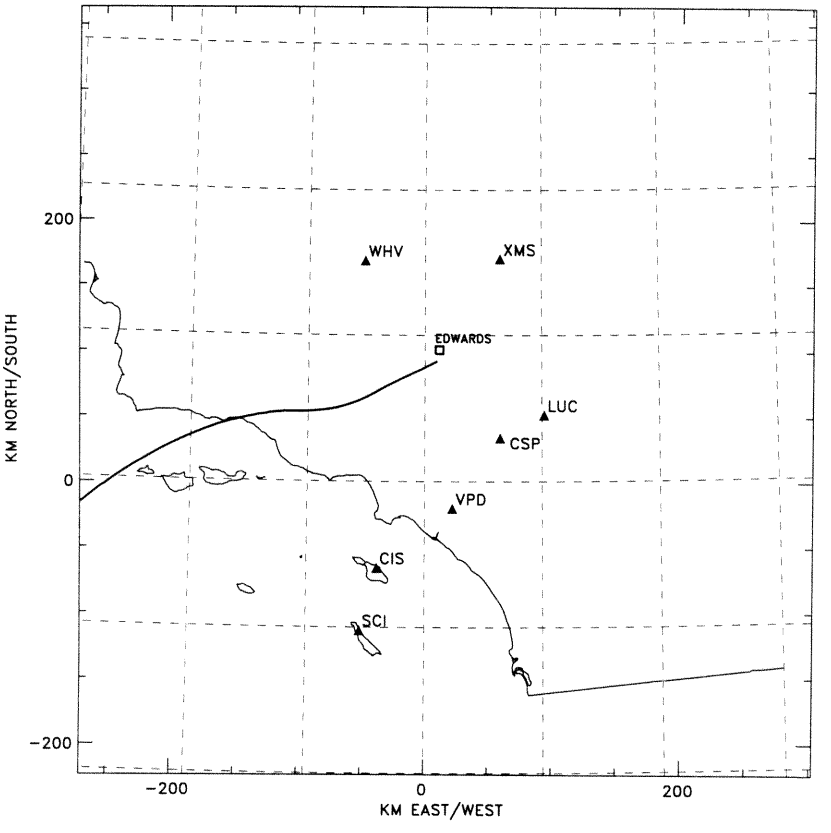

(a) See following figure for caption.

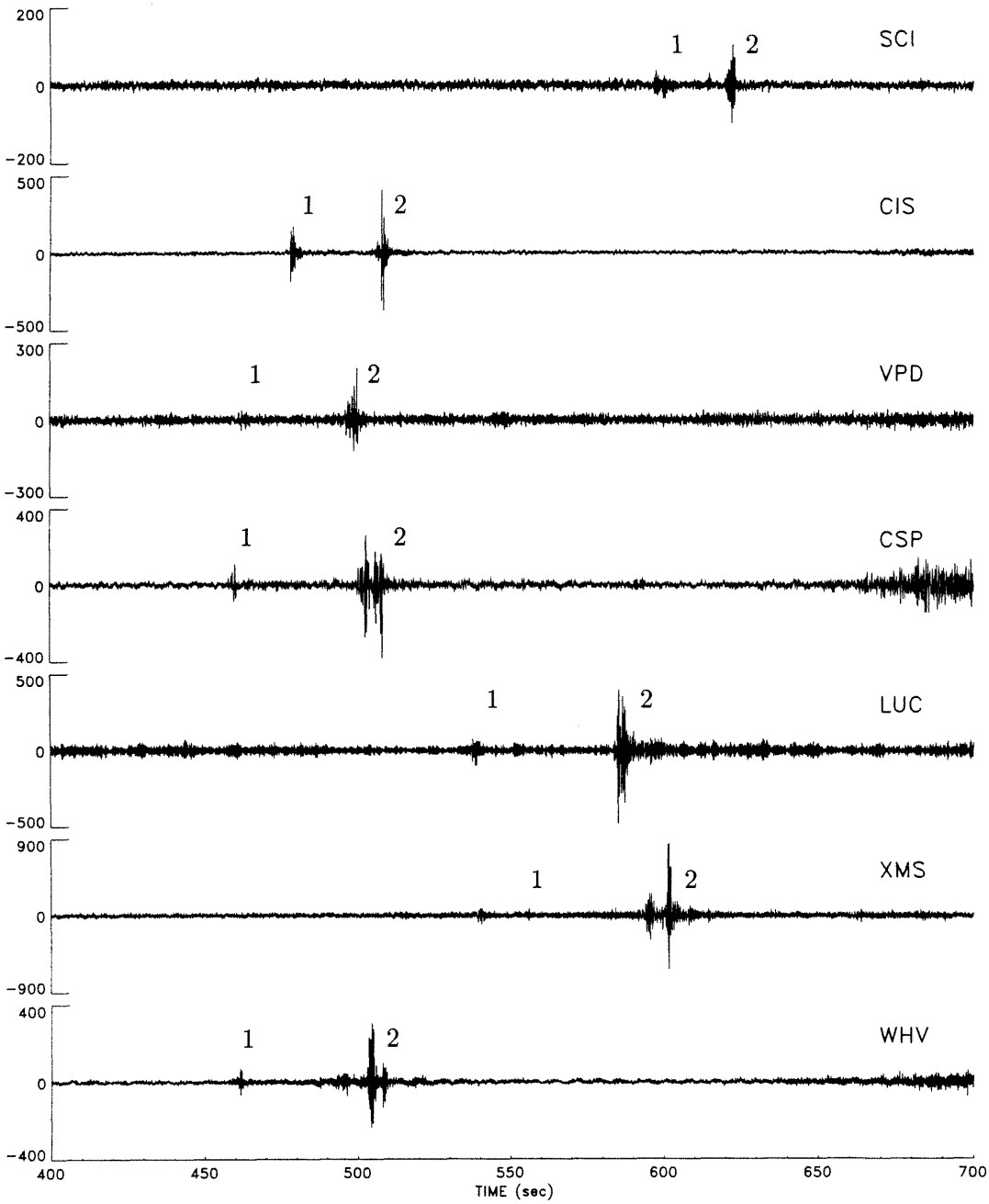

Figure B.11: (a) Seismic station locations relative to the STS-42 trajectory and (b) time traces from selected seismic stations within the shadow region predicted by raytracing for STS-42 reentry. Time traces record ground motion, vertical scale is voltage output in counts.

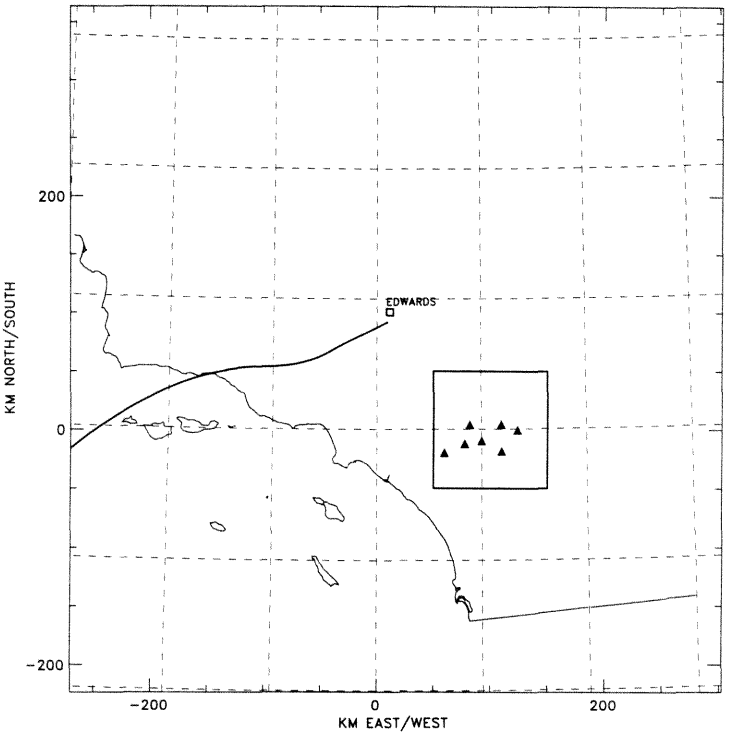

(a) See final figure for caption.

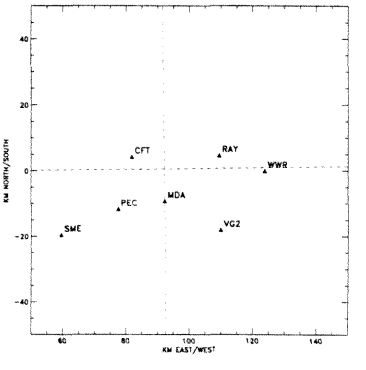

(b) See final figure for caption.

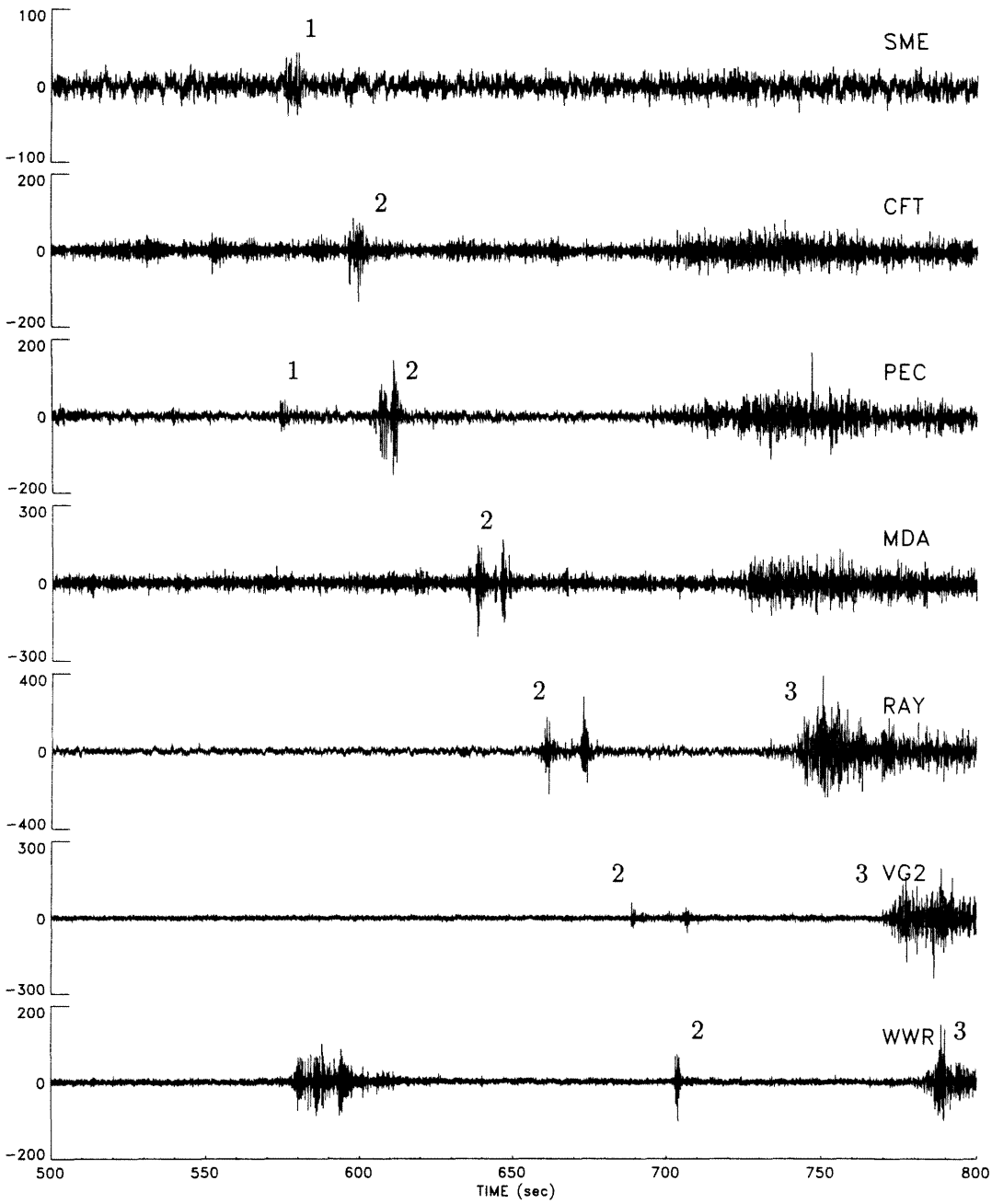

Figure B.12: (a) Seismic station locations relative to the STS-42 trajectory, (b) map inset, and (c) time traces from selected seismic stations within the secondary carpet predicted by raytracing for STS-42 reentry. Time traces record ground motion, vertical scale is voltage output in counts.

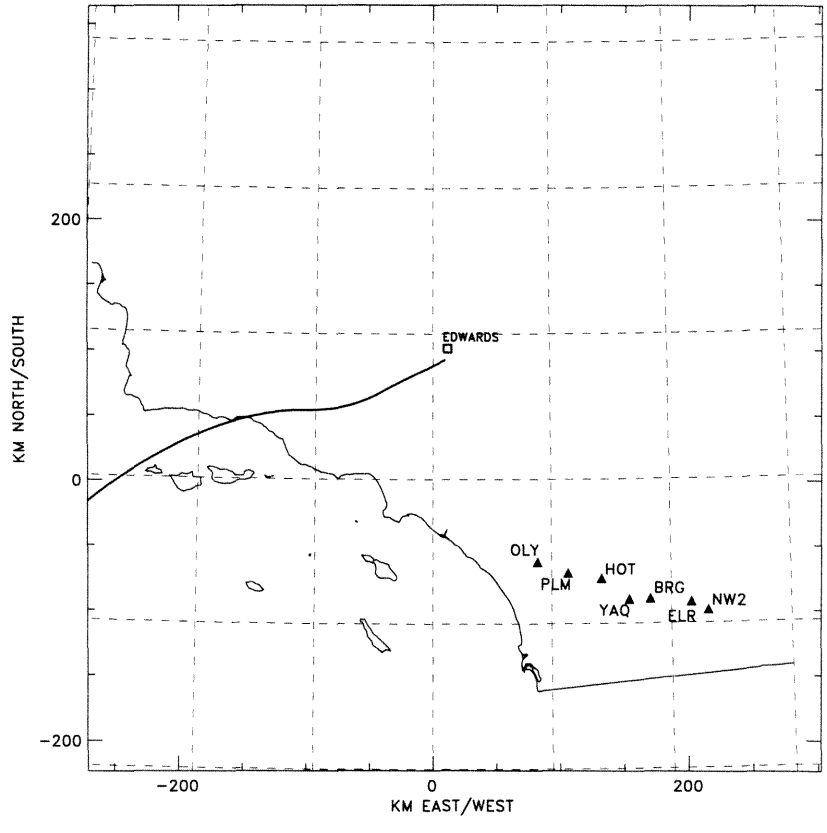

(a) See following figure for caption.

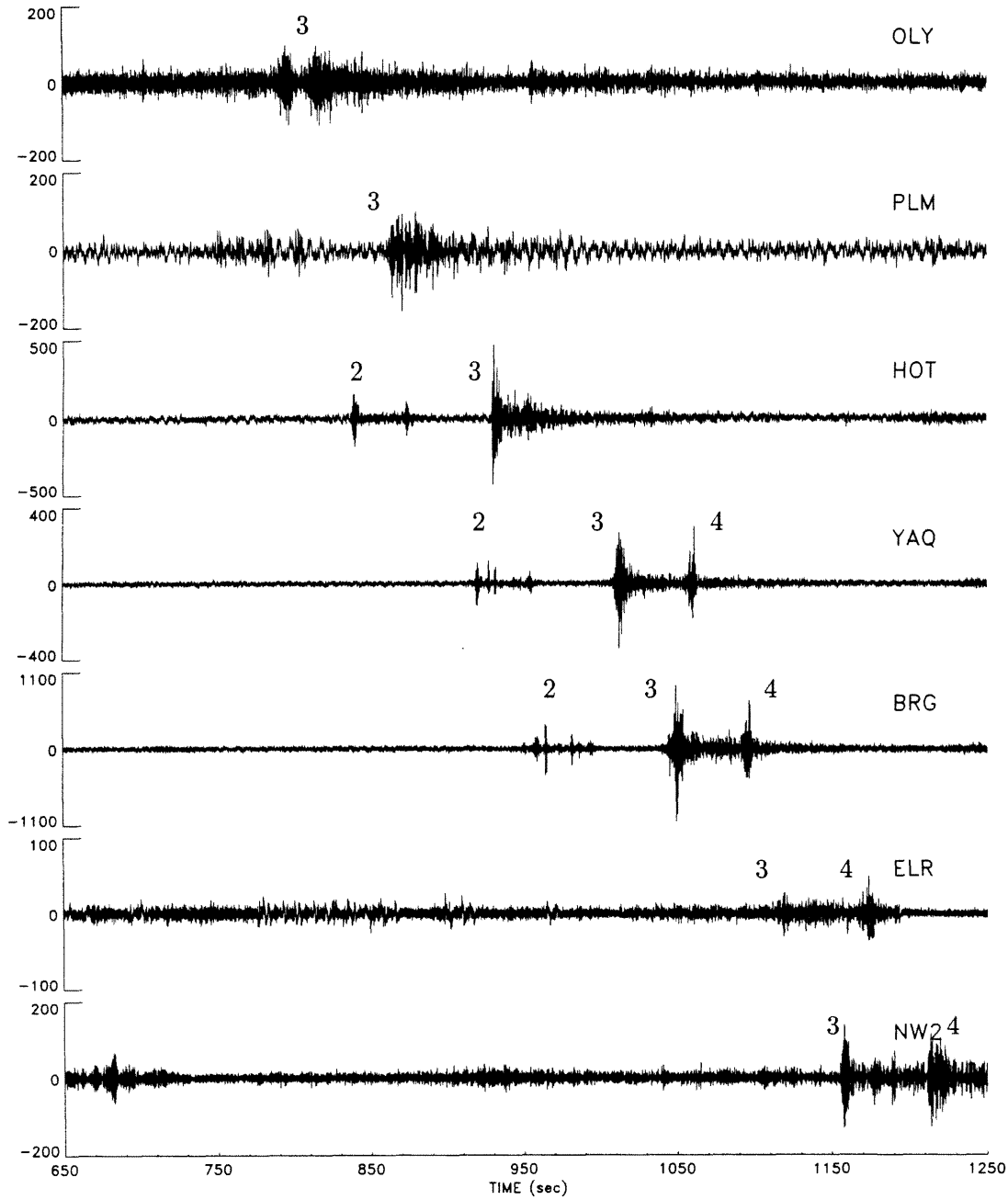

Figure B.13: (a) Seismic station locations relative to the STS-42 trajectory and (b) time traces from line of seismic stations outside the secondary carpet predicted by raytracing for STS-42 reentry. Time traces record ground motion, vertical scale is voltage output in counts.

B.3.3 Discovery Reentry

A network of seismic stations in Washington and Oregon detected the December 9, 1992 reentry of space shuttle Discovery (Qamar 1993). Figure B.14 shows contours of arrival times from 66 seismic sites covering both sides of the flight track for distances of over 500 kilometers. Arrival times supplied by Qamar have been converted to a regular grid and contoured without any assumptions about the original trajectory. The strong curvature of the contours and the relatively sparse data result in the oscillations seen along the contours; however, the outline of the hyperbolae in the primary carpet is clearly visible.

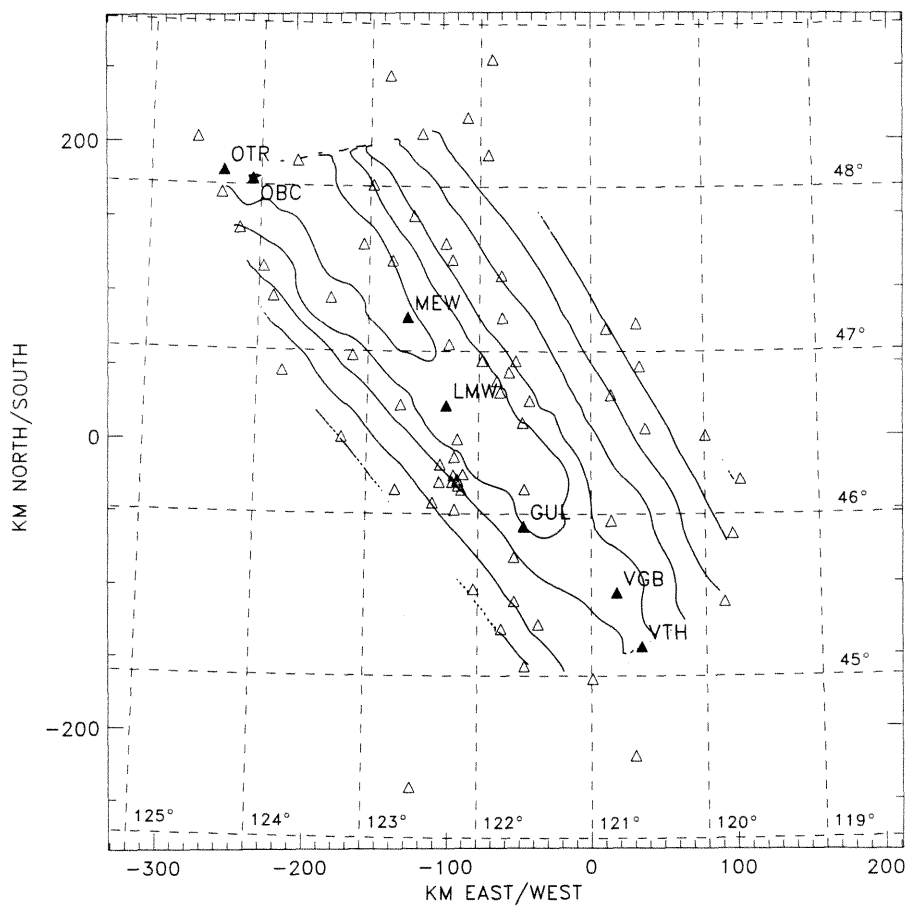

Figure B.14: Arrival time contours from seismic data for the December 1992 reentry of space shuttle Discovery over seismic network in Washington and Oregon. Time traces record ground motion, vertical scale is voltage output in counts. (Data supplied by Dr. A. Qamar, University of Washington.)

Sections of the time traces for the seven labeled stations are shown in Figure B.15. The stations are plotted in order of the arrival of the signal, *i.e.*, north to south; however, the time origin is shifted to align the arrival of the primary disturbance. The later stations show two disturbances which Qamar postulated were the two peaks of the N-wave, which would correspond to an N-wave duration of over 1 second.

To the present author's knowledge, such long duration N-waves have not been observed before. A simple calculation of the Mach angle from the hyperbola contours in Figure B.14 yields a Mach number of approximately $M = 14$. From a typical shuttle reentry profile, this Mach number corresponds to an altitude of approximately 55 km. Computing the N-wave duration from the standard approximate relations (Whitham 1974) gives an N-wave duration of no more than 0.8 sec. However the accuracy of the estimate for such high altitude and Mach number is difficult to assess. Long N-wave durations up to 0.7 sec have been observed from the space shuttle reentry using pressure transducers (Garcia *et al.*, 1985), for a sonic boom estimated to have originated from the shuttle at $M = 5.87$ at an altitude of 39.4 km, which is still much later in reentry than the sonic booms recorded in Washington. The appearance of the two peaks on such widely separated sites does rule out local geological effects.

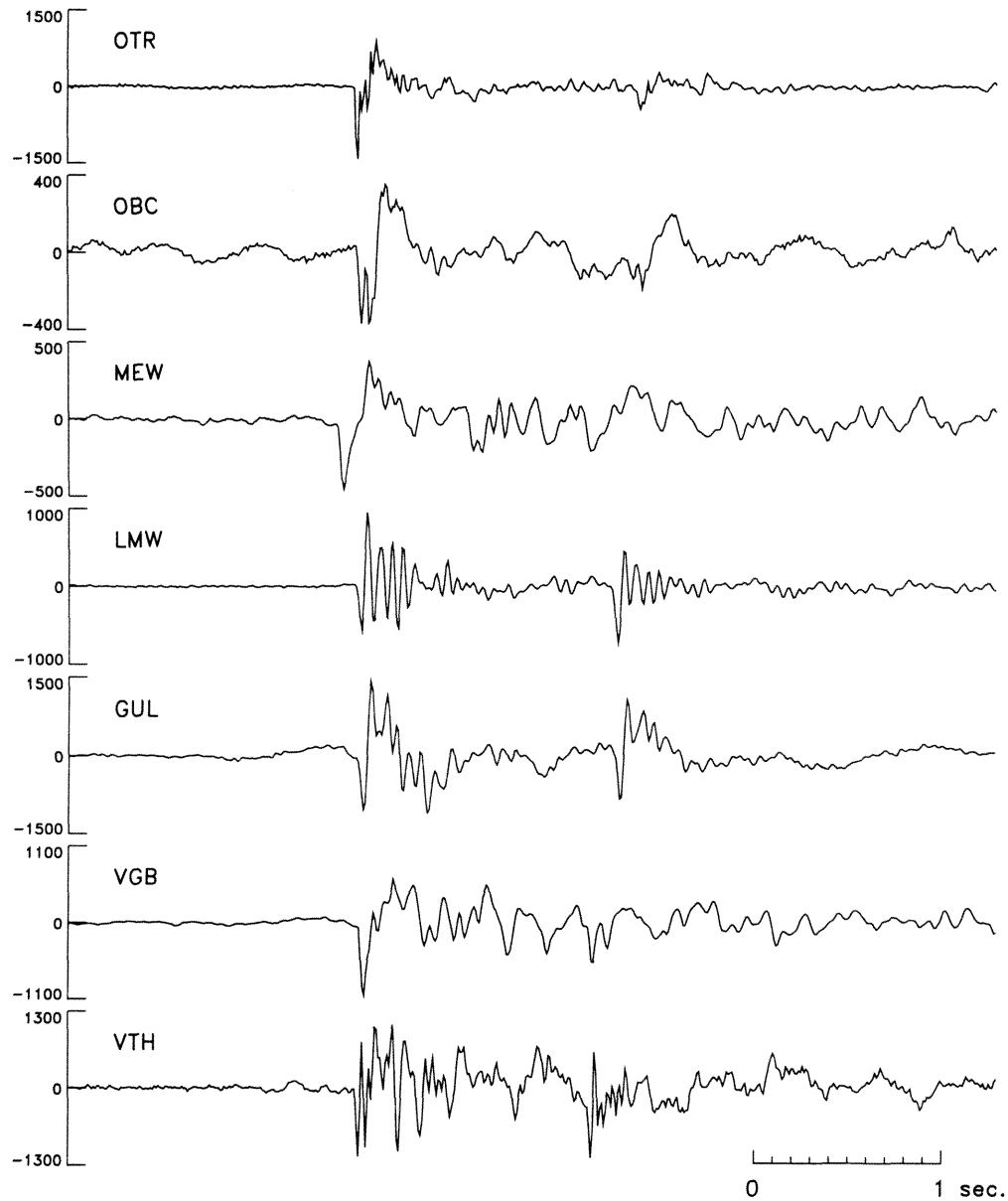

Figure B.15: Seismic traces for stations shown in Fig. B.14 for December 1992 reentry of space shuttle Discovery. (Seismic data supplied by Dr. A. Qamar, University of Washington.)

B.4 Mystery Booms

In the latter-half of 1991 and early 1992, the U.S.G.S. office in Pasadena received a number of calls from the general public concerning "mystery booms" heard in Southern California. Initially the events were assumed to be earthquakes, but further analysis of the seismograph records suggested sonic booms as the most-likely source. An initial analysis of the seismic signals by the U.S.G.S. by attempting to fit hyperbola to the arrival time data for 25 sites near the coast attributed the sonic booms to a source flying at high altitude and high Mach number. These reports were picked up in the popular press and attributed to a top-secret hypersonic Aurora spyplane. A unique feature of the events was that all occurred on Thursday morning at approximately 0700, as shown in Table B.1.

Time	**Date**
6:34 PDT	Thu June 27, 1991
6:46 PST	Thu Oct. 31, 1991
6:43 PST	Thu Nov. 21, 1991
7:17 PST	Thu Jan. 30, 1992
6:59 PST	Thu Apr. 16, 1992
Unknown	Thu June 18, 1992
6:38 PDT	Thu Oct. 15, 1992

Table B.1: Mystery boom occurrences. The October 1991 and January 1992 events are analyzed in the current work.

Following the early claims, the Air Force commissioned MIT Lincoln Labs to investigate the incidents. The available seismograph records for 41 sites for the October 1991 event were analyzed. Again the arrival times were fit as hyperbola, although an attempt was made to include the effects of vehicle deceleration and atmospheric refraction. The disturbances were attributed to the sonic booms from two F-4 Phantoms returning to Edwards AFB, flying supersonic near Mach 1 overland. None of the sites examined by Lincoln Labs included the third boom mentioned below.

In view of the above disagreement, the October 1991 and January 1992 events were analyzed in the present study. The raw seismograph time data were obtained and analyzed for all 209 available sites for both events. Arrival times were chosen

from the data and contoured without any assumptions concerning the shape of the time contours.

On the October 31, 1991 event, three booms are clearly distinguished on the time traces. The first boom appears on 90 sites throughout the seismic network. The boom dies out as one moves east and is not seen on the easternmost sites. The first boom is generally followed by a second boom which appears at the largest number of sites, 104, at an average of 83 seconds later. A third boom appears only at 30 of the easternmost sites, an average of 84 seconds after the second boom. The contours of arrival times are shown in Fig. B.16 for each of the three booms identified. The triangle symbols represent seismic sites for which data were available, and filled triangles show the sites which detected each boom.

The northern limit of detection of the sonic boom is clearly defined, since a large number of sites in the northeast did not detect the boom. This is consistent with the low amplitude of the boom observed near the northern boundary. However, the southern edge of the boom carpet is not well defined, due to the lack of seismograph sites further south in Mexico. The booms show a relatively high amplitude at the southern sites which suggests the boom carpet may extend further south. Twelve additional sites in Mexico logged no unusual activity for that morning. However, since the actual seismographic data are not available, the sites are not included in this report.

A second event, from January 30, 1992, was also examined in detail, and arrival time contours for the three booms observed are shown in Fig. B.17. The same pattern of three disturbances are observed: the first boom on the western sites, the second across the entire network, and the third only on the eastern sites. The booms were detected across the entire network from west to east, but the booms were confined to a narrower north to south band.

Only one of the events examined does not display the circular patterns stretching from west to east characteristic of the above two events. The boom from Wednesday, September 30, 1992 is a narrow circular pattern extending from south to north. The center of the circular pattern lies offshore, south of Catalina Island.

The analysis of the complete set of data eliminates both of the early theories for the source of the mystery booms. The lack of characteristic N-wave signatures and the fact that no booms were detected on the northwestern sites rules out the original theory of a high-speed aircraft flying north off the coast. At the speeds predicted (Mach 5 – 6), one would expect to see strong N-wave signatures with high amplitude near the coast, as with the shuttle reentry booms. The Lincoln Lab theory of two aircraft flying essentially down the center of the boom pattern fails to explain the three events detected. The aircraft would have to be flying at a speed of approximately Mach 1 relative to ground sound speed which would place the aircraft at or near the cutoff velocity for their altitude. In the case of a single aircraft, the first boom would be considered the primary boom carpet, and the second and third booms would be secondary booms. However, this single aircraft theory can be ruled out, since indirect booms would not be expected to appear under the aircraft track.

From the complete analysis, all the observed booms appear to be indirect booms from a source offshore propagated inland by high winds. Southern California typically has strong jet stream winds and stratospheric winds blowing from west to east. Such anomalous sound propagation is well-known, and mystery booms attributed to aircraft are not a new phenomenon. In the late 1970's, a series of East Coast mystery booms occurred. Although a wide range of phenomena were grouped into the "mystery booms," the majority were attributed to indirect sonic booms from the Concorde (Rickley & Pierce 1980) and sonic booms from military aircraft maneuvering offshore. Similar propagation of sonic booms over 100 kilometers by the high jet stream winds have been observed in Tucson (Wood 1975).

The magnitudes of the ground velocity for the October 31, 1991 events are shown in Fig. B.18. Magnitudes are corrected for instrument response, however no attempt is made to incorporate local site surface properties. For clarity, all amplitudes over 200 are plotted as 200. Higher ground velocities are found offshore, near the theorized source of the sonic booms. The large amplitudes on the easternmost sites seem to be due to local ground properties near the sites. Using the estimate of of 1.5 – 2 μm/sec per Pascal of overpressure, the ground velocity amplitudes correspond to the range of

average pressures 0.15 – 0.2 Pa observed for Concorde indirect sonic booms (Rickley & Pierce 1980).

An attempt to associate the mystery booms with specific flight operations from any of the local military bases has been unsuccessful. Local military bases reported no unusual activity on the dates of the mystery booms; in particular, the Pacific Missile Test Range which operates offshore from Point Magu reported no supersonic flight operations on the mornings of the October 1991 or January 1992 events.

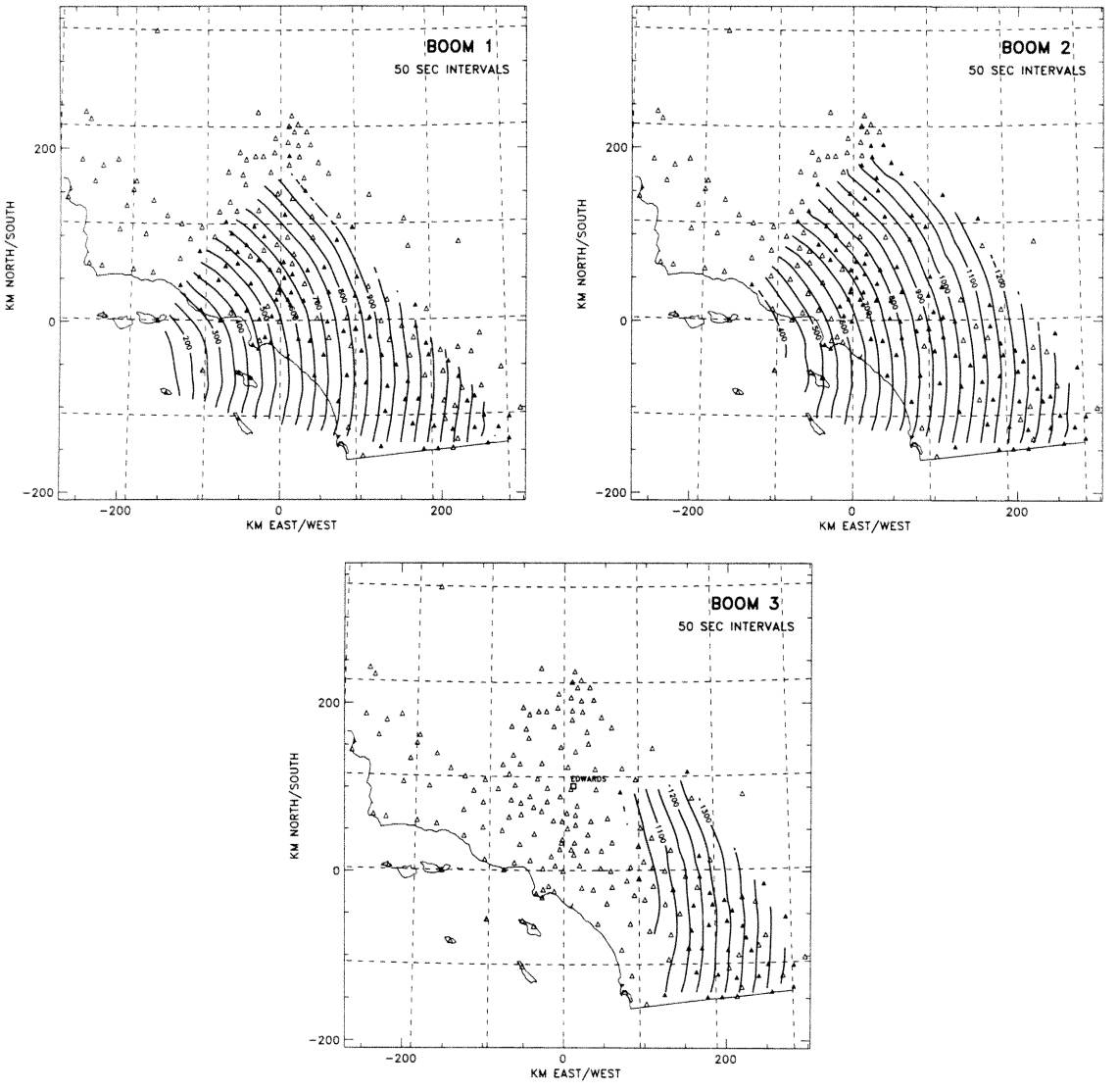

Figure B.16: Arrival time contours generated from seismic data for October 31, 1991 "mystery boom."

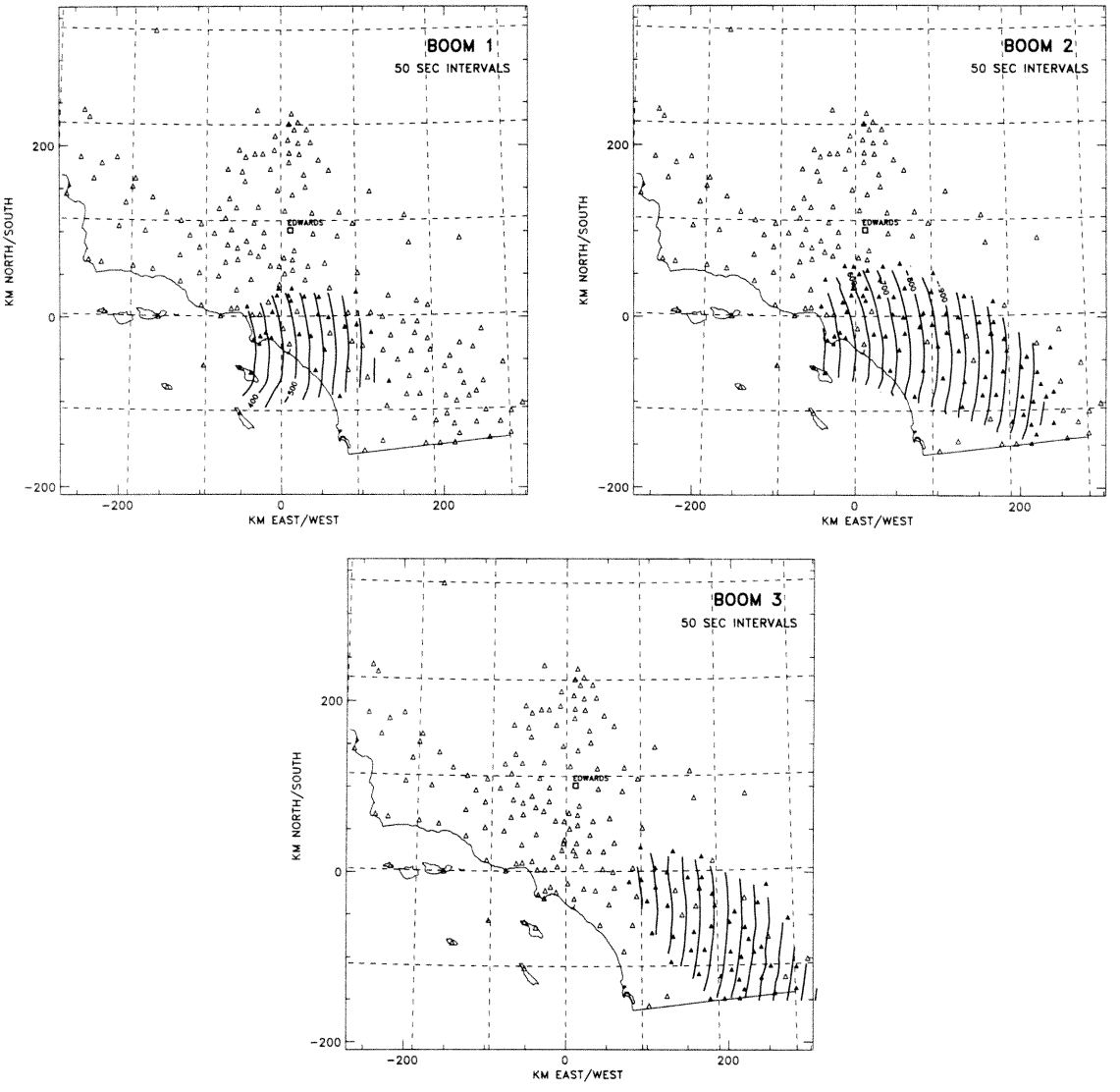

Figure B.17: Arrival time contours generated from seismic data for January 30, 1992 "mystery boom."

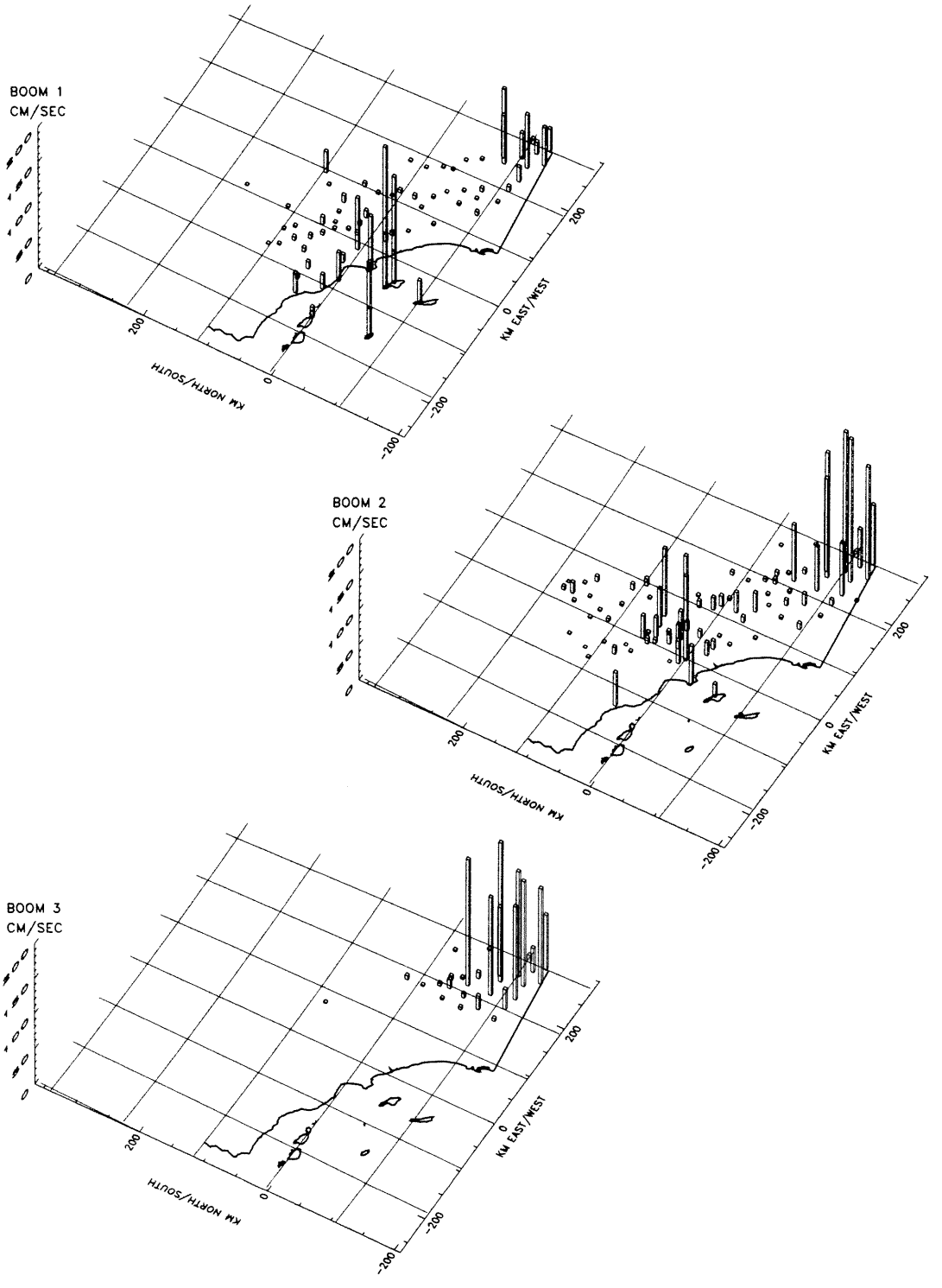

Figure B.18: Ground velocity magnitude (cm/sec) for October 31, 1991 events, corrected for instrument response. All amplitudes over 200 are plotted as magnitude 200 for clarity.

B.5 Conclusion

The seismic network in Southern California has provided the first opportunity to study the size and shape of indirect sonic boom carpets over a large area. The high density of the sites and large ground coverage allow analysis of the direct and indirect boom patterns on both sides of the flight trajectory, and the development of the booms can be followed over several hundred kilometers. The recent addition of pressure transducers at selected TERRAscope sites remedies the only significant weakness of the seismic data, the difficulty of predicting amplitudes.

From analysis of the space shuttle STS-42 reentry, the ground patterns are extremely complex. Ray theory fails to predict indirect sonic boom arrival times, observed multiple booms within the first shadow region, and extensive overlap of the multiply refracted sonic booms. The extensive ground coverage of the "mystery boom" and shuttle reentry booms suggest exposure under the real atmosphere is much larger than previously expected.

The inverse problem of predicting the aircraft trajectory from the ground arrival times is more difficult. Nonetheless, using the seismic network data, we were able to identify the source of the "mystery booms" as indirect booms propagated from offshore operations. However, careful study of the seismic data is required to identify direct and indirect sonic boom carpets before attempting to make predictions about the trajectory.

B.6 Acknowledgements

Seismic data and instrument information for the Southern California seismic network were kindly provided by Dr. H. Kanamori, Caltech Seismological Laboratory and Dr. J. Mori, U.S.G.S., Pasadena. Seismic data for the Discovery reentry were supplied by Dr. A. Qamar, University of Washington. Shuttle trajectory information was courtesy of Gene Stansbury and Joel Montalbano of NASA. Additional thanks are due to Dr. R. Meyer, Dr. J. Ehernberger, Dr. D. Lux., and Bob Cohn of NASA Dryden

and Dr. J. Greene of JPL for allowing us to participate in the SR-71 flight.

Bibliography

Balachandran, N., Donn, W., and Rind, D. (1977) "Concorde Sonic Booms as an Atmospheric Probe," *Science*, **197**, 47–49.

Ben Menachem A. and Singh, S. (1981) *Seismic Waves and Sources*, Springer-Verlag, New York.

Cook, J., Goforth, T., and Cook, R. (1970) "Ground Motion from Sonic Booms," *J. Aircraft*, **7**, 126–129.

de Violini, R. (1967) "Climactic Handbook for Point Magu and San Nicolas Island, Volume I, Surface Data," *PMR-MR-67-2.*

de Violini, R. (1969) "Climactic Handbook for Point Magu and San Nicolas Island, Volume I, Upper-Air Data," *PMR-MR-69-7.*

Garcia, F., Jones, J., and Henderson, H. (1985) "Correlation of Predicted and Measured Sonic Boom Characteristics From the Reentry of STS-1 Orbiter," *NASA TP-2475.*

Goforth, T. and McDonald, J. (1968) "Seismic Effects of Sonic Booms," *NASA CR-1137.*

Kanamori, H., Mori, J., Sturtevant, B., Anderson, D., and Heaton, T. (1992) "Seismic excitation by space shuttles," *J. Shock Waves*, **2**, 89–96.

Meteorology Group, Range Commanders Council. 1983 Range Reference Atmosphere 0 – 70 Km Altitude: Edwards AFB, California. *Doc. 366-83.*

Onyeowu, R. (1975) "Diffraction of sonic boom past the nominal edge of the corridor." *J. Acoust. Soc. Am.*, **58**, 326–330.

Pierce, A. (1981) *Acoustics: An Introduction to Its Physical Principles and Applications*, McGraw-Hill, New York.

Rickley, E. and Pierce, A. (1980) "Detection and Assessment of Secondary Sonic Booms in New England," *FAA-AEE-80-22.*

United States Committee on Extension to the Standard Atmosphere. 1966 *U. S. Standard Atmosphere Supplements*, Washington, U.S. Govt. Printing Office.

Whitham, G. (1974) *Linear and Nonlinear Waves*, Wiley, New York.

Wood, R. (1975) "Jet Stream – Sonic Boom Phenomena, Tucson, Arizona, April 1975," *Weatherwise*, **28**, 152–155.